THE DEVELOPMENT OF A PRESSURE TRANSDUCER AND ITS USE FOR STATISTICAL MEASUREMENTS IN A DEVELOPING TURBULENT PIPE FLOW.

by

D.P. KOSTIUK

Department of Mechanical Engineering

University of Manitoba

A Thesis presented to the faculty of Graduate Studies

in partial fulfillment of the requirements for the degree of

Master of Science

September, 1970

ABSTRACT

A miniature pressure transducer capable of measuring both static and transient pressures has been developed using a piezojunction sensing element. Spectral density measurements of the fluctuating wall pressure beneath a turbulent boundary layer obtained using this transducer, when compared to published results, verify that it may be used, with confidence, for turbulence measurements.

Using the pressure transducer to detect the fluctuating wall pressures and a hot-wire probe to measure the fluctuating velocity component in the axial direction, the flow structure in a developing pipe flow was studied. Energy spectral densities and cross correlations of the fluctuating wall pressures and fluctuating velocities were measured in a developing pipe flow, and from these measurements a qualitative picture of the pressure field and velocity field in such a flow has been presented.

ACKNOWLEDGMENTS

The author would like to take this opportunity to express his appreciation to Dr. R. S. Azad, for serving as his thesis adviser and for his continuing guidance and encouragement in this endeavor. Sincere thanks are also due to Dr. J. Tinkler for his careful and critical review of this thesis, and to Mr. R. H. Hummel for his invaluable assistance with regards to the instrumentation aspects of this work.

Finally, the financial support provided by the National Research Council of Canada for conducting this research is gratefully acknowledged.

TABLE OF CONTENTS

TABLE OF CONTENTS (continued)

TABLE OF CONTENTS (continued)

LIST OF ILLUSTRATIONS

LIST OF ILLUSTRATIONS (continued)

LIST OF ILLUSTRATIONS (continued)

LIST OF ILLUSTRATIONS (continued)

NOMENCLATURE

$C_f(\omega)$	correction factor for spectral density values at a given frequency.
f	frequency (Hz).
$f_A(t)$	a time function of a stationary process.
L	distance from entrance of pipe to test section.
p	instantaneous static pressure fluctuation.
$Q_{AA}(\xi_2,\xi_1;\tau)$	auto correlation function.
$Q_{AB}(\xi_2,\xi_1;\tau)$	cross correlation function.
r	radial coordinate measured outwards from the pipe axis.
R	inside pipe radius.
R_θ	Reynolds number based on U_∞ and θ.
$R_{pp}(\xi_2,\xi_1;\tau)$	auto correlation coefficient.
$R_{pq}(\xi_2,\xi_1;\tau)$	cross correlation coefficient.
T	averaging time.
u	instantaneous fluctuating velocity component in axial direction.
U	local mean velocity in axial direction at r.
U_c	longitudinal convection velocity.
U*	shear stress velocity defined as $(\tau o/\rho)^{\frac{1}{2}}$.
U_∞	free stream velocity.
v	instantaneous fluctuating velocity component in radial direction.
x_1	position vector of pressure transducer in relation to reference position.
γ	intermittency factor.
δ	boundary layer thickness.

NOMENCLATURE (continued)

δ^*	displacement thickness.
θ	momentum thickness.
ξ_1	position vector in radial direction measured from the surface of the pressure transducer.
ξ_2	position vector in axial direction measured from the radial plane in which the pressure transducer is located.
ρ	fluid density.
τ	time delay.
τo	wall shear stress.
$\Phi_{pp}(\omega)$	spectral density function of a fluctuating signal, p.
$\Phi(f)$	power spectral density; that is, the mean square pressure per unit bandwidth.
$\Phi(m)$	measured energy spectral value at a given frequency.
Φ	corrected energy spectral value at a given frequency.
ω	angular frequency.

INTRODUCTION

In industries dealing with fluid flow over a boundary surface, such as the aircraft or petroleum industries, a working knowledge of the flow phenomenon occurring at the boundary is essential if optimum performance of equipment and processes is to be attained. Consequently, a great deal of research into the structure of turbulence in the boundary layer has been undertaken in an attempt to formulate mathematical models which could be used to predict various aspects of the flow phenomenon.

In an incompressible turbulent flow, the main dependent variables are velocity and pressure, and until recently, the majority of the experimental investigations in turbulent flow have dealt only with the velocity components of the flow. This was mainly due to the early development of the hot-wire anemometers, however, with the recent development of miniature pressure transducers capable of detecting small, transient pressures, there have been more and more studies of the fluctuating wall pressures in turbulent flow.

Direct measurements of pressure fluctuations within a turbulent flow, as compared to measurements of the velocity fluctuations are not possible, because suitable pressure transducers which would have no significant influence on the flow field have not as yet been developed. Experimental work is therefore limited to the measurement of the wall pressure fluctuations produced by turbulent shear flow over a boundary surface in which the sensing element of the pressure transducer may be flush mounted, so as not to disturb the flow.

Several investigations have been carried out using correlation

techniques to determine the relationships between the fluctuating velocity fields and the pressure fields in a turbulent boundary layer. These have been measured in order to obtain an understanding of the structure of the scale of the eddies that produce the pressure fluctuations. Most of the experimental work to date has been conducted in two dimensional turbulent boundary layers over a flat plate and in fully developed turbulent pipe flow, whereas, very little work has been done in a three dimensional boundary layer as found in developing pipe flow.

One of the aims of this work was to develop a pressure transducer capable of detecting the fluctuating wall pressures present in turbulent boundary layers. The sensing element selected for the transducer is basically a silicon planar NPN transistor that has its emitter-base junction mechanically coupled to a diaphragm.

Using the pressure transducer to detect the fluctuating wall pressures, energy spectra and cross correlation measurements of the fluctuating wall-pressures and velocities will be obtained in a turbulent boundary layer of a developing pipe flow.

CHAPTER 1

THE DEVELOPMENT AND TESTING OF THE PIEZOJUNCTION PRESSURE TRANSDUCER

1.1 Introduction

In the last fifteen years a great deal of attention has been focused on the development of miniature pressure transducers capable of detecting transient pressures as found in the field of gas dynamics. One of the aims of this work was to develop a low cost, yet versatile pressure measuring system capable of measuring differential static pressures and fluctuating pressures as encountered in turbulence measurements.

For the static mode of operation the basic requirements for the transducer are as follows:

1. A high sensitivity to applied pressure.
2. An output which is linearly proportional to the applied pressure.
3. Good thermal D.C. stability properties.
4. A mechanism with a minimum of hysteresis.

When measuring transient pressures, the transducer should exhibit the above qualities, as well as the following:

1. A flat frequency response over the range of operation.
2. A high resonant frequency for the transducer assembly.
3. An output not affected by mechanical vibrations.
4. A minimum thermal sensitivity shift.

Recent investigators, Willmarth and Wooldridge (1965), Bull (1963), Kawamura (1960) and Schloemer (1967) have used pressure transducers containing a piezoelectric transduction element with a variety of crystal materials such as Barium-Titanate, Lead-Zirconate, and Lead-Titanate--Lead-Zirconate. The source impedance of a piezoelectric transducer is very high and hence

conventional amplifiers or oscilloscopes, which have an input impedance of the order of 1 megohm or less, cannot be used to monitor the output signal directly. Consequently there is a need for a low noise amplifier with an impedance of at least 100 megohms across its signal-input terminals. This problem has been more or less solved with the use of Field Effect Transistors, however, the necessity of a high-input impedance, low-noise amplifier adds greatly to the cost of the system.

Rather than use piezoelectric crystals, it was decided to use a new and inexpensive pressure sensing element which is commercially available under the trade name of PITRAN*. Basically, the PITRAN is a silicon planar NPN transistor that has its emitter-base junction mechanically coupled to a diaphragm. The electrical characteristics of this sensor are such that a relatively large output voltage occurs with small pressure changes, and hence the added cost and problems of an external signal amplification system may be eliminated. The result is a simple and inexpensive pressure measuring system capable of detecting both static and fluctuating pressures.

The construction details and the characteristic properties of the pressure measuring instrument developed are described in the following sections.

* PITRAN is a Stow Laboratories' registered trademark.

1.2 The Pressure Transducer.

1.2.1 Description of Sensing Element and Probe Unit.

As mentioned in section 1.1, the sensor is a silicon planar NPN transistor with a stress sensitive emitter-base junction. Figure 1.1(a) shows how the junction is mechanically coupled to the diaphragm. When a pressure is applied to the diaphragm the electrical characteristics of the transistor are changed due to the creation of localized stresses in the junction, a phenomenon which is referred to as the Anisotropic Stress Effect. Because of this, the current gain of the transistor is extremely sensitive to the applied stress and hence, to the motion of the diaphragm. The small, full scale deflection of the diaphragm, approximately 2 μ inches, has the advantage of offering a very small volumetric displacement of the sensing element, and hence very little disturbance to the flow. As a result of the small movements and the high sensitivity to applied stress, the manufacturers of the PITRAN have claimed a conversion efficiency (electrical energy out/mechanical energy in) much higher than that of any other pressure sensing element.

In order to use the sensor (see Figure 1.1(b) in both the static and dynamic mode, a fairly rugged and versatile mounting system had to be devised. Figure 1.2(a) shows the details of the holder with 1.2(b) showing how the holder was mounted in the wall of a pipe with the sensing element flush with the wall. As the container of the PITRAN is connected to the collector of the transistor, the sensing element had to be electrically insulated from the holder, and to achieve this, a semi-rigid epoxy (ECOBOND-45) was used with very satisfactory results.

To minimize the electromagnetic pickup, a seven wire, shielded cable was constructed with the base lead shielded by the emitter lead for each PITRAN. Care had to be taken in the electrical connection of the cable to

the holder in order to ensure that it would not exert a pull on the leads of the PITRAN during operation, as a distortion of the header could induce spurious signals in the output.

Once the PITRANS were installed in the holder the result was a fairly compact, rugged and versatile pressure transducer. As mentioned previously, one of the advantages of these sensors is the large output, and this eliminates the need for a great deal of external signal conditioning. However, as the PITRANS were differentially biased, for temperature stability reasons, a certain amount of signal conditioning was necessary. The nature and extent of the signal conditioning is discussed in the succeeding section.

1.2.2 Design and Construction of the Pressure Transducer Electrical Circuit.

Due to the relatively high (-100 mv/^{o}C) temperature coefficient of the PITRAN, it was necessary to install a temperature matched pair of sensing elements, differentially biased, in order to minimize the thermal zero shift. Figure 1.3 shows the circuit diagram for the system and because the PITRAN is basically a transistor, conventional transistor circuit design techniques were employed. The first stage operational amplifier (AMP 1) was used to convert the double ended output from the PITRANS into one signal. From the output of (AMP 1) the signal is further conditioned, first through an integrator (C1,R1) and then through a differentiating (C2,R2) circuit. The last operational amplifier (AMP 3) being used strictly for a gain control with the gain adjustable from 0 to 25.

The section, enclosed by dashed lines in Figure 1.3, is the part of the circuit used to balance the sensitivities and tracking of the two sensing elements. When the two PITRANS were received, it was found

that the sensitivities were different, with the β values being 18 and 8 for PITRAN 1 and PITRAN 2 respectively. To compensate for this difference, the base currents of the PITRANS were adjusted by varying the base resistances. In the balance network, all the biasing potentiometers interact with one another, however, B-1 can be considered a track adjustment with B-2 setting the operating point of the PITRANS while B-3 adjusts the D.C. zero of the output.

Because of the interaction of B-1, B-2 and B-3, an iterative procedure was necessary for their adjustment. To ensure that the last stages (AMP 2 and AMP 3) were D.C. zeroed, AMP 1 was AC coupled to AMP 2 and the output balance B-4 adjusted for a zero output. With the last stages D.C. zeroed, the first stage was again D.C. coupled to the rest of the circuit and the trim potentiometers B-1 and B-2 adjusted using an iterative procedure for a zero output voltage. For this adjustment the operating point was arbitrarily set at -8.0 volts so as to ensure that the collectors of the PITRANS were always reverse biased with respect to the bases.

A more precise optimizing technique consisted of plotting a curve of the output for different pressures applied to each sensing element, while keeping the differential pressure, ΔP, between them a constant. A ΔP of zero was found to be convenient and Figure 1.4 shows the results obtained with various W3 and emitter junction voltages. For applied pressures up to 400 mm of water to both sensors, the results showing a zero output is obtained with W3 and emitter junction voltages of -2.61 and -8.0 volts respectively.

1.3 The Calibration of the Transducer.

1.3.1 The Static Calibration.

The transducer is capable of measuring both static and fluctuating pressures, and consequently, a calibration could be obtained relatively easily by taking advantage of its static capabilities. On the other hand, this ease in calibration is not available for transducers which operate on a capacitive principle, as they can measure only the transient pressures. Thus, they must be calibrated with the use of pressure pulses such as obtained with shock tubes (Willmarth and Wooldridge (1963), Bull (1963)).

To perform the calibration, a differential static calibration unit (see Figure 1.5) was built with a variable hydrostatic pressure being supplied by a movable column of water. With this set up it was possible to apply a constant differential pressure to the pressure transducers while varying the pressure on each sensing element. Using this technique a family of curves of constant differential pressure was obtained as illustrated in Figure 1.6, and by cross-plotting the data from this figure a calibration curve for the differential mode of operation was obtained as shown in Figure 1.7. Both positive and negative pressures, from 0 to 400 mm of water, were applied to the transducer in order to give a wide operational range for the measurement of the static differential pressures as encountered in turbulent flow.

When the calibration technique was used with one of the PITRANS exposed to atmosphere, the applied differential pressure equalled the static pressure on the PITRAN. Hence, individual calibration curves for each sensing element were also obtained. A typical calibration curve is shown in Figure 1.8 with data points obtained during one calibration cycle. The results of this static calibration are best described with the linearity, hysteresis and repeatability characteristics as given in the following

paragraphs.

The linearity of a transducer's calibration is defined as the maximum deviation of any calibration point from the corresponding point on a specified straight line during one calibration cycle. Consequently, it is important to know the exact nature of the straight line to which the calibration curve is compared. Several straight lines were tried, however, little difference was obtained in the results, so the value reported is for an Independent Linearity referred to the "Best Straight Line". From Figure 1.8 the independent linearity was measured to be ±1.5% of the full scale output (F.S.O.).

The hysteresis of the transducer's calibration is defined as the maximum difference in any pair of output readings so obtained during any one calibration cycle. From the calibration curve (Figure 1.8) the hysteresis was measured to be 3% F.S.O.

The ability of the transducer to reproduce output readings when the same pressure is applied to it consecutively, under the same conditions, and in the same direction, is referred to as the repeatability. This has been measured to be within 0.5% F.S.O. as long as the emitter junction voltage and the W3 voltage were set at their optimum values.

Another important static characteristic is the D.C. stability of the instrument. Figure 1.9 shows a long range stability test performed with continuous monitoring for 82 hours. The relatively large change (+1% F.S.O.) in output voltage from hour 27 to hour 35 is directly correlated with a $6^{o}F$ increase in ambient temperature experienced during this time period. During the rest of the time the ambient room temperature remained relatively constant. The results of this test indicate that the instrument has about a three hour warm up period with the D.C. stability being affected by temperature changes. However, there does not appear to be any D.C.

drift with time.

Because of the warm up period the instrument was kept on continuously for the whole time period in which experimental data was obtained.

1.3.2 The Dynamic Calibration.

The transducer will be used for measurements where rapid pressure variations occur, and consequently, the transducers' dynamic characteristics must be established. A useful indication of the ability of the transducer to operate under various frequency ranges is the frequency response, which is formally defined as the change with frequency of the ratio of the output signal to the pressure signal amplitude.

The determination of the frequency response was accomplished by a comparison of the spectral density curves obtained using the transducer and a calibrated condenser microphone. A loudspeaker was excited with random noise, and the resulting pressure waves were measured, using both a Brüel and Kjaer half inch condenser microphone and the transducer. A schematic drawing of the test set up is given in Figure 1.10. The outputs from these transducers were analyzed in the frequency domain using a Hewlett-Packard Model 3590 A Wave Analyzer with the results given in Figure 1.11. The bandwidth used in these tests was 10 Hz.

The characteristics of the loudspeaker were not known and, as it turned out, the speaker had several definite resonant frequencies. However, this did not interfere with the test as only a comparison between the two spectra was being made. In fact, the distinct peaks were used to compare the tracking of the two sensors. As only relative shapes of the two curves were compared, the ordinate is, for ease in measurement, represented in decibels with respect to an arbitrary reference.

To ensure that an adequate signal-to-noise ratio existed for the

frequency spectral measurements, the power spectrum of the ambient noise of the pressure transducer was determined. This measurement is essentially a measure of the ambient noise in the room and the electronic noise in the transducer and accompanying electronics. The power spectral density curve for the ambient noise is also presented in Figure 1.11 and is some 20 db below the signal, a value which can be considered to be acceptable.

From the power spectral density curves it can be seen that the pressure transducer performed as well as the condenser microphone up to about 15 KHz. Above this frequency the transducer still continued to give an output where as the response of the condenser microphone rapidly degenerated around 20 KHz and beyond. Due to the comparative nature of the test it cannot be said that the transducer employing the PITRAN sensing elements has a better frequency response than the microphone. However, one may conclude that the response was equal to that of the condenser microphone. The half inch microphone used was recently calibrated and the individual calibration curve (See Figure A.2) supplied with the microphone, showed a flat (± 1 db re 0.0002 μb) response from 20 Hz to 20 KHz. Thus the frequency response of the pressure transducer may be represented as being flat (± 1 db re 0.0002 μb) from 0 to 20 KHz, with the strong possibility of having an even larger dynamic range than indicated, as signals beyond 60 KHz have been detected.

1.4 Effects of Experimental Environment on Transducer Performance.

The accuracy of the results depends greatly on how the output of the transducer is affected by vibrations, temperature variations and environmental sound field. These conditions will be discussed separately in the following sections.

1.4.1 Vibrations

A major effect of environmental vibrations is the application of low frequency acceleration forces to the sensing element which "look-like" pressure fluctuations to the transducer. The magnitude of these acceleration-induced output errors are proportional to the mass and stiffness of the sensing element. As the PITRAN sensor has a very small mass, and a relatively stiff diaphragm, it was felt that acceleration forces would not contribute significantly to the output signal.

This assumption was verified by mounting the transducer in the test section, with the sensing element blocked off from the flow, and recording the power spectrum for the transducer in a vertical and a horizontal position. If acceleration effects had been significant, there would have been a marked increase in energy levels when the acceleration sensitive axis of the sensing element coincided with the axis of gravity (transducer in vertical position). However, this was not the case as shown in Figure 1.14 where the mechanical coupling spectrum was taken with the transducer in the horizontal and vertical position.

A further effect of vibrations on a transducer is the excitation of internal components into higher frequency "sympathetic" vibrations at their resonant frequencies. At these resonant frequencies the applied vibration amplitude could be greatly amplified by the vibrating components, and large output errors would results Thus, it is necessary forthe natural frequency of the transducer to be appreciably higher than the highest significant

frequency of vibration of the structure on which the transducer is to be installed.

Vibration tests carried out on the transducer showed that the natural mechanical resonant frequency of the unit is 58 KHz. In order to determine the structure vibration, an independent test was made with a Brüel and Kjaer accelerometer, Model 4339, mounted by means of a magnet on the test section. The wind tunnel was then operated at its maximum speed. The output from the accelerometer was analyzed with the wave analyzer and the resulting power spectral density curve is shown in Figure 1.12. From this figure, prominant peaks can be seen up to 10 KHz, especially around the1KHz region; however, beyond the 10 KHz frequency range there are no significant peaks. Thus, it can be concluded that with a resonant frequency of 58 KHz for the transducer, the structure vibrations should not contribute a significant amount to the overall signal.

A further test to verify this was accomplished by installing the transducer in the tunnel wall such that the sensing element was blocked off from the flow. The method used to cover the sensing element did not completely eliminate the pickup of pressure fluctuations, however, it did reduce the signal output. With the tunnel operating at a center line velocity of 200 ft/sec, a power spectrum of the transducer output signal was obtained with the test section coupled mechanically to the rest of the tunnel and with an air coupling arrangement. The latter method essentially isolated the test section from vibrations and hence is a measure of the signal whereas the former method measured the signal plus vibrations. Figure 1.14 shows the output of this test and, recalling that signals add in quadrature when dealing with power spectra, it can be seen that the vibration effects are sufficiently small to be neglected. It can also be noted that the predominant

peaks at 70 and 140 Hz are present in both curves, consequently one may conclude that they are not due to vibrations. It was initially believed that these were due to the sound field in the test section, and consequently, tests were carried out to determine the sound field intensities. These tests are described in section 1.4.3.

1.4.2 Temperature Effects.

Exposure of a transducer to temperatures above or below that at which the calibration was usually performed causes some changes in the calibration. The PITRANS, because of their high thermal zero shift, are especially susceptible to temperature changes. It is for this reason that two temperature matched PITRANS were used, biased in a differential mode.

The characteristics important for the description of the thermal properties of the transducer are both the thermal zero shift and the thermal sensitivity shift. The former is a parallel displacement of the calibration curve while the latter is indicated by a change in the slope of the calibration curve.

The temperature dependency test was performed by submerging the pressure transducer, enclosed in a waterproof container, into a constant temperature bath ($\pm$ .05^{o}F). Using the static calibration unit, new calibration curves at different temperatures were determined, with the results shown in Figure 1.13. From this figure, the thermal sensitivity shift was determined to be 0.15% F.S.O. per degree Fahrenheit with the thermal zero shift being 1% F.S.O. per degree Fahrenheit.

1.4.3. Sound Field.

As the presence of a sound field in the working section is likely to give rise to interference with the wall pressure measurements it was

necessary to determine the intensity of the sound field.

An attempt to measure the sound field in the free stream condition was made using a faired half inch Brüel and Kjaer condenser microphone. The nose fairing on the microphone was designed to reduce the aerodynamically induced noise present when the microphone is exposed to high wind speed.

However, the results of the tests were inconclusive as the microphone could not be introduced into the test section in a satisfactory manner. Further sound tests were carried out with the measurements of the ambient noise outside the test section with and without the wind tunnel operating. The spectra revealed little information with regard to any significant sound frequencies being present. However, the tests without the wind tunnel running did reveal the 120 Hz "hum" of the lights in the Turbulence Lab. As well as the 120 Hz peak, the spectrum also showed the harmonics of the "hum".

From the sound measurements, no definite conclusions could be reached with regards to the presence of a strong sound field in the test section.

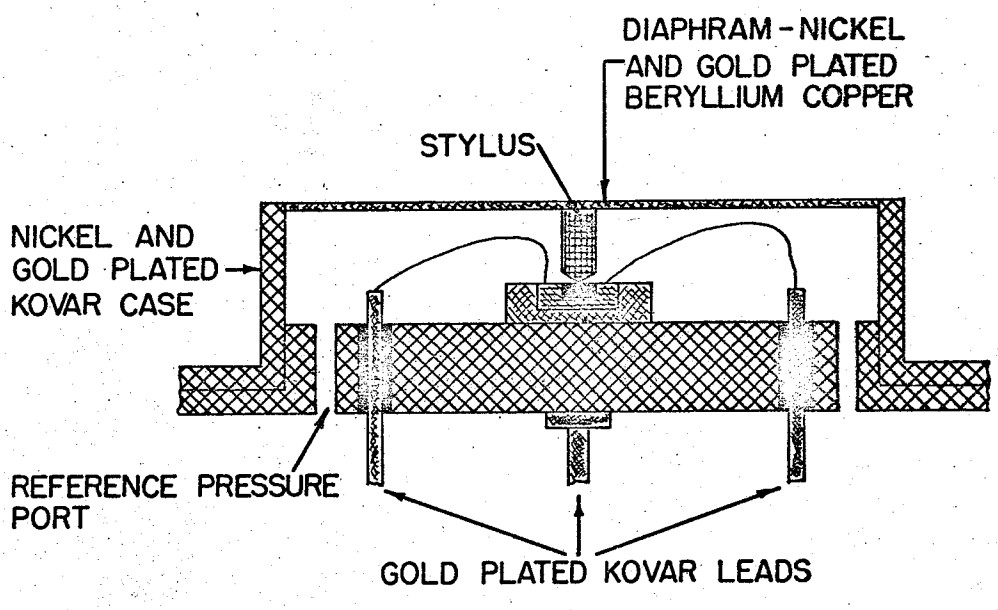

1(a)

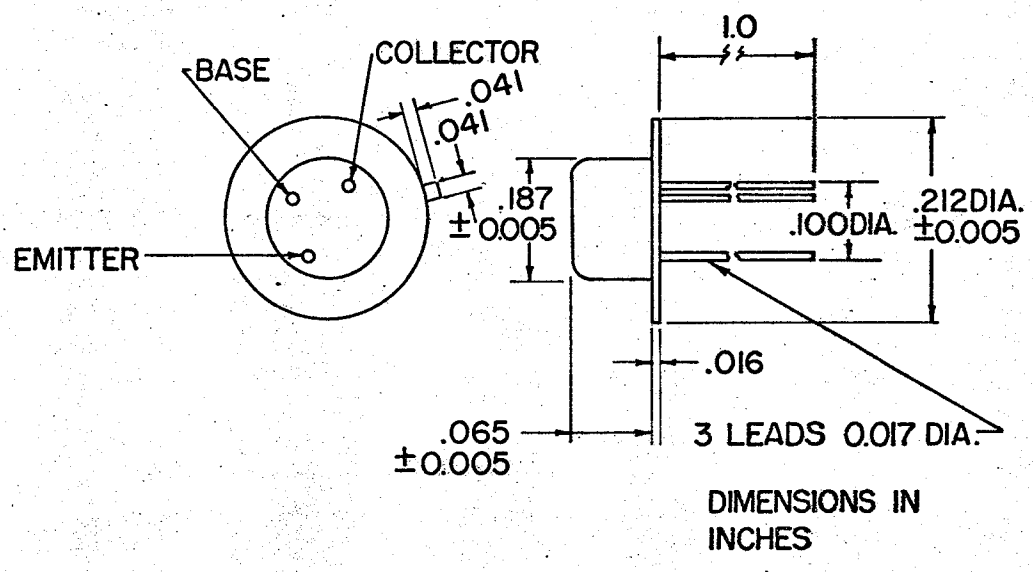

1(b)

FIGURE 1.1(a) Cross-section schematic of PITRAN sensing element.

(b) Dimensions of PITRAN

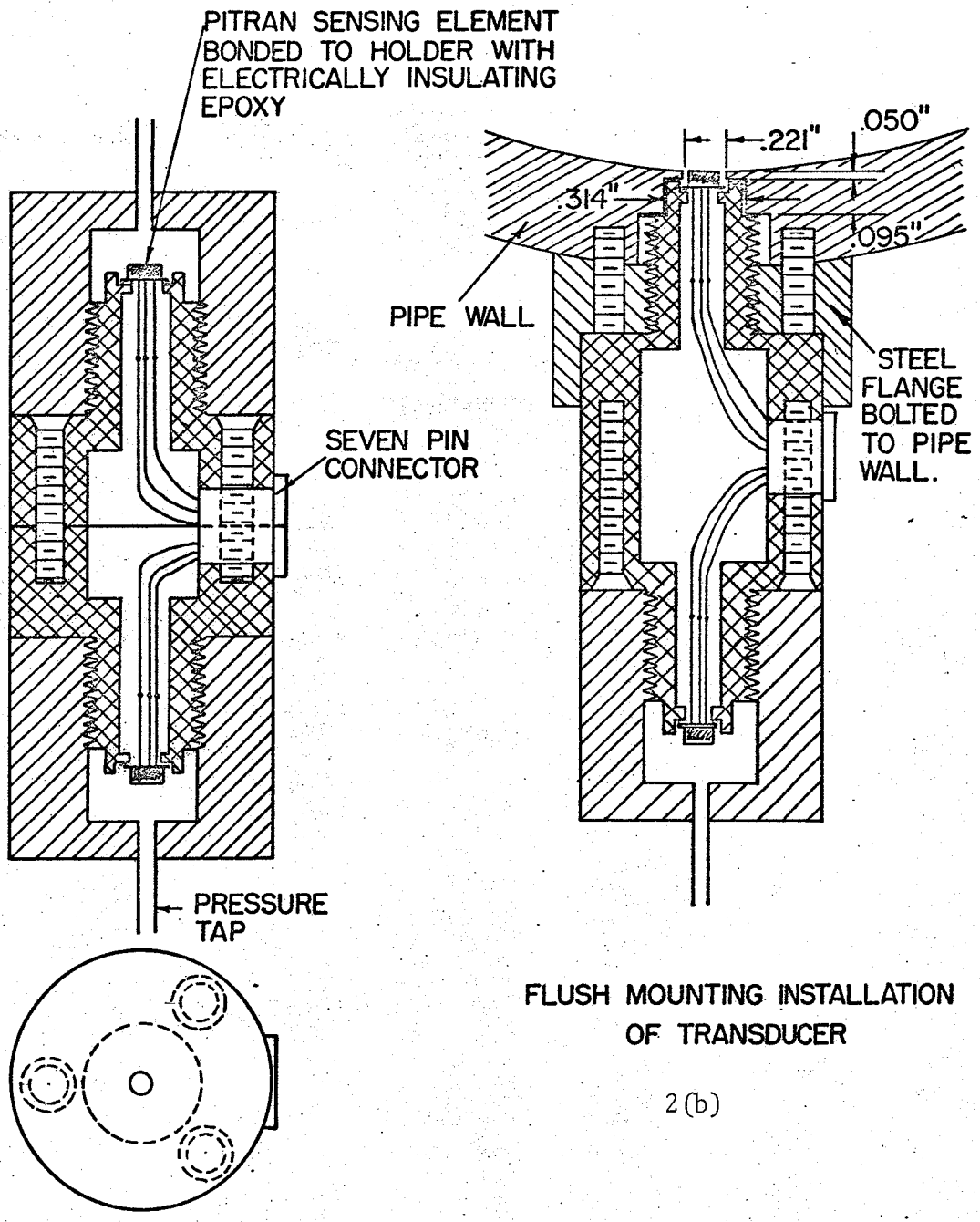

FIGURE 1.2(a) Construction details of pressure transducer.

(b) Flush mounting installation of transducer in the test section.

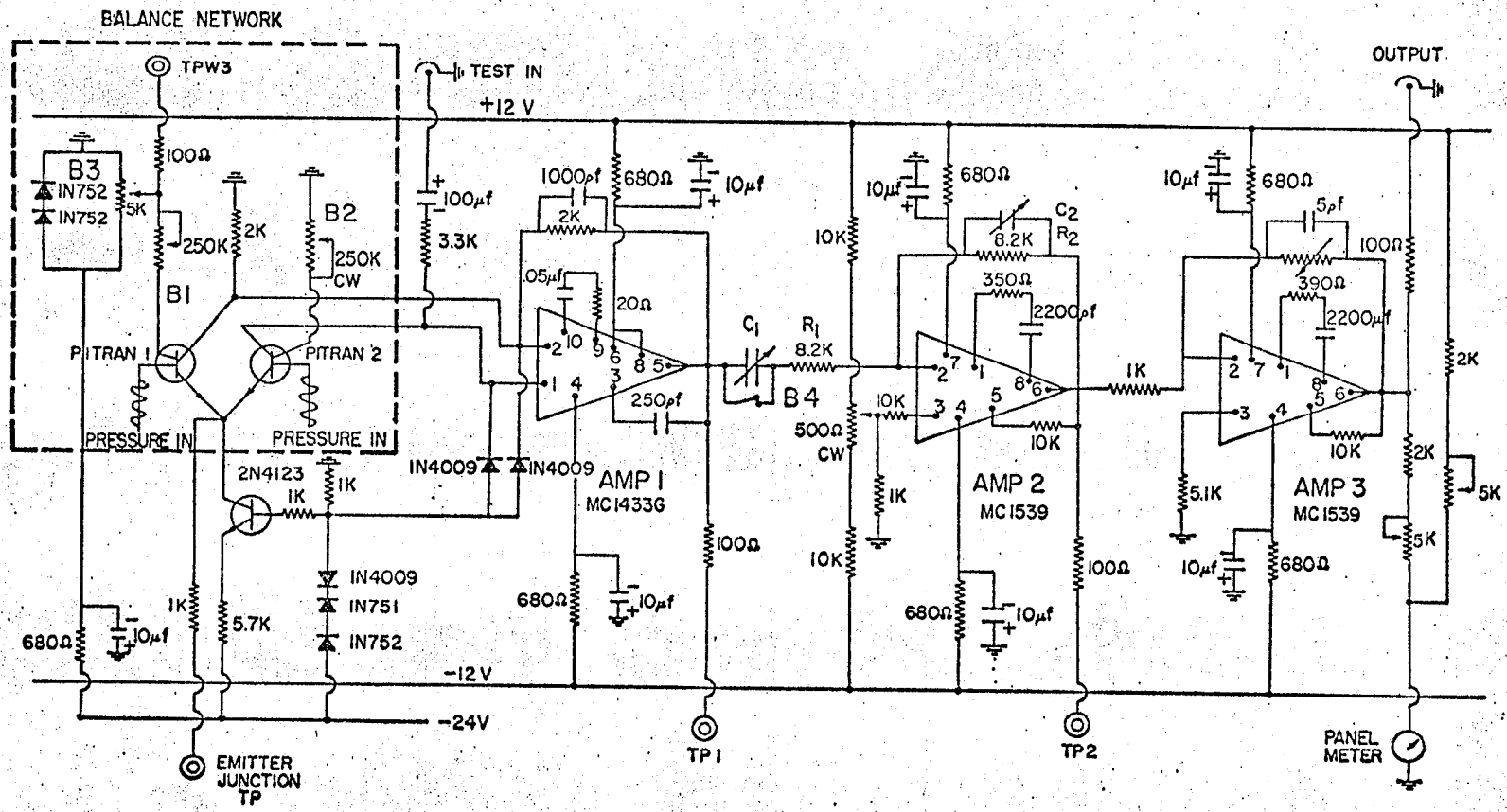

FIGURE 1.3 CIRCUIT DIAGRAM OF PRESSURE MEASURING INSTRUMENT.

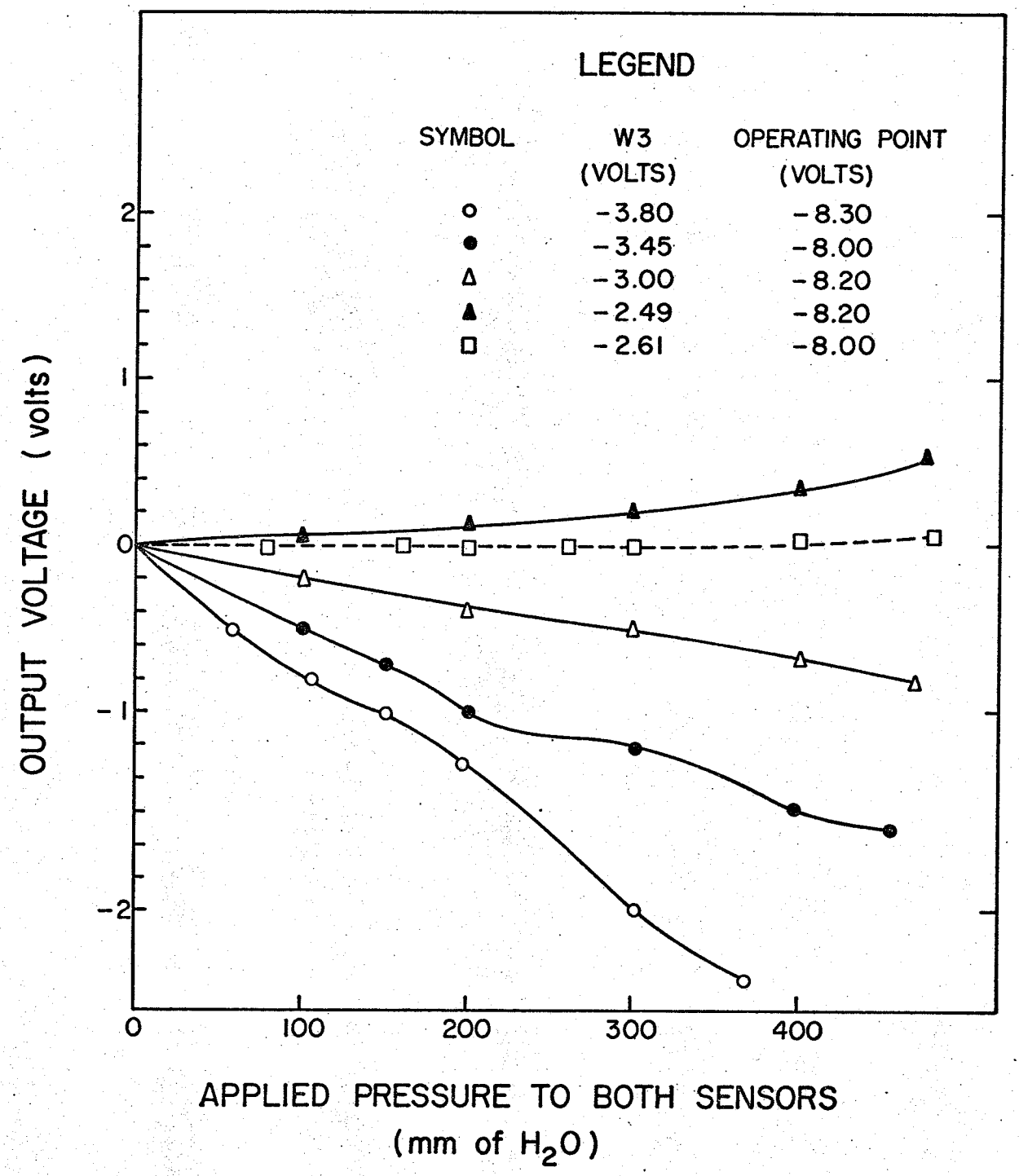

FIGURE 1.4 OPTIMIZATION TECHNIQUE USED TO DETERMINE THE SETTINGS FOR THE TRIM POTENTIOMETERS B-1 AND B-2.

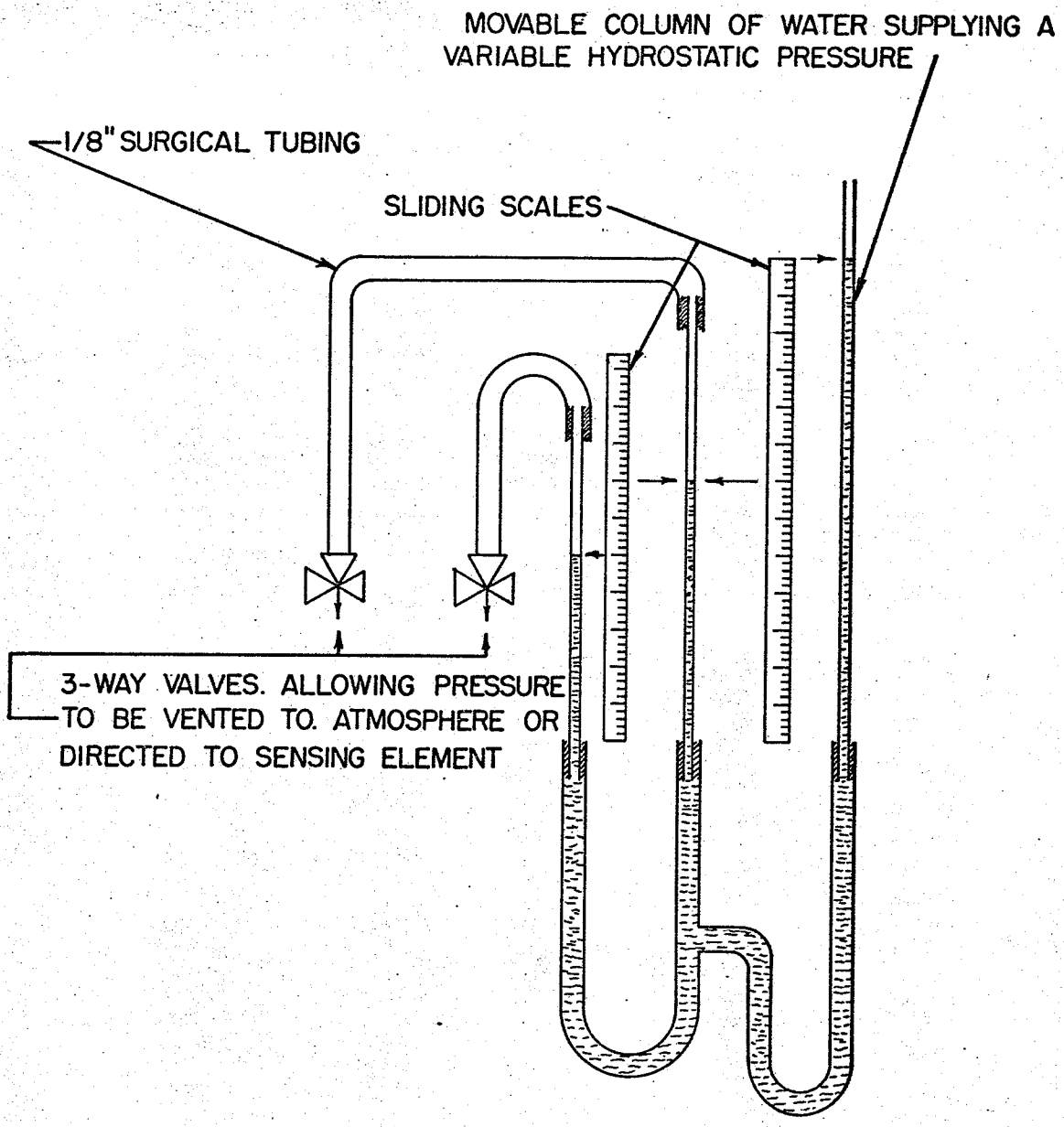

FIGURE 1.5 SCHEMATIC OF DIFFERENTIAL STATIC CALIBRATION UNIT.

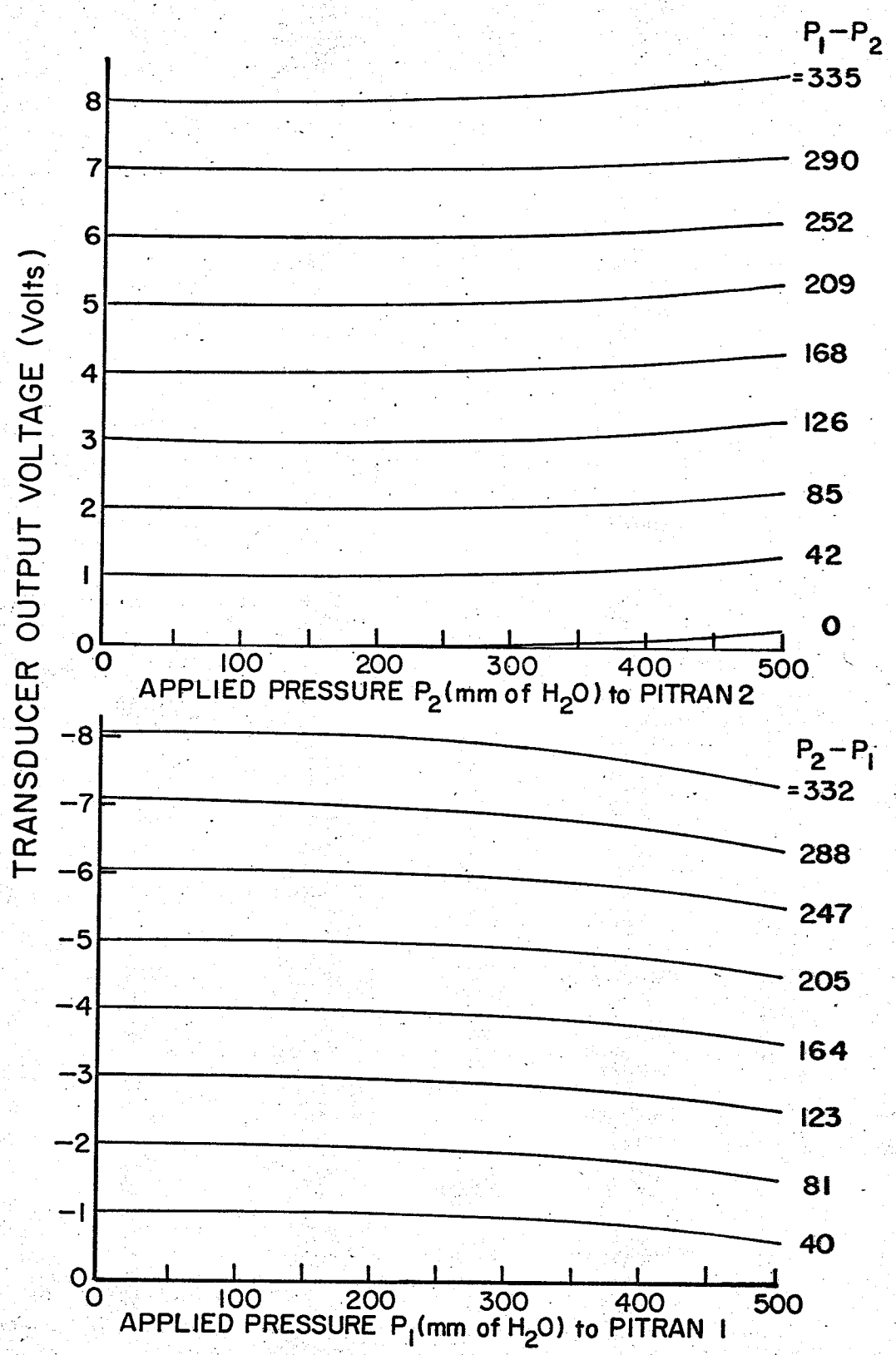

FIGURE 1.6 FAMILY OF CURVES OF CONSTANT ΔP OBTAINED FROM A DIFFERENTIAL STATIC CALIBRATION.

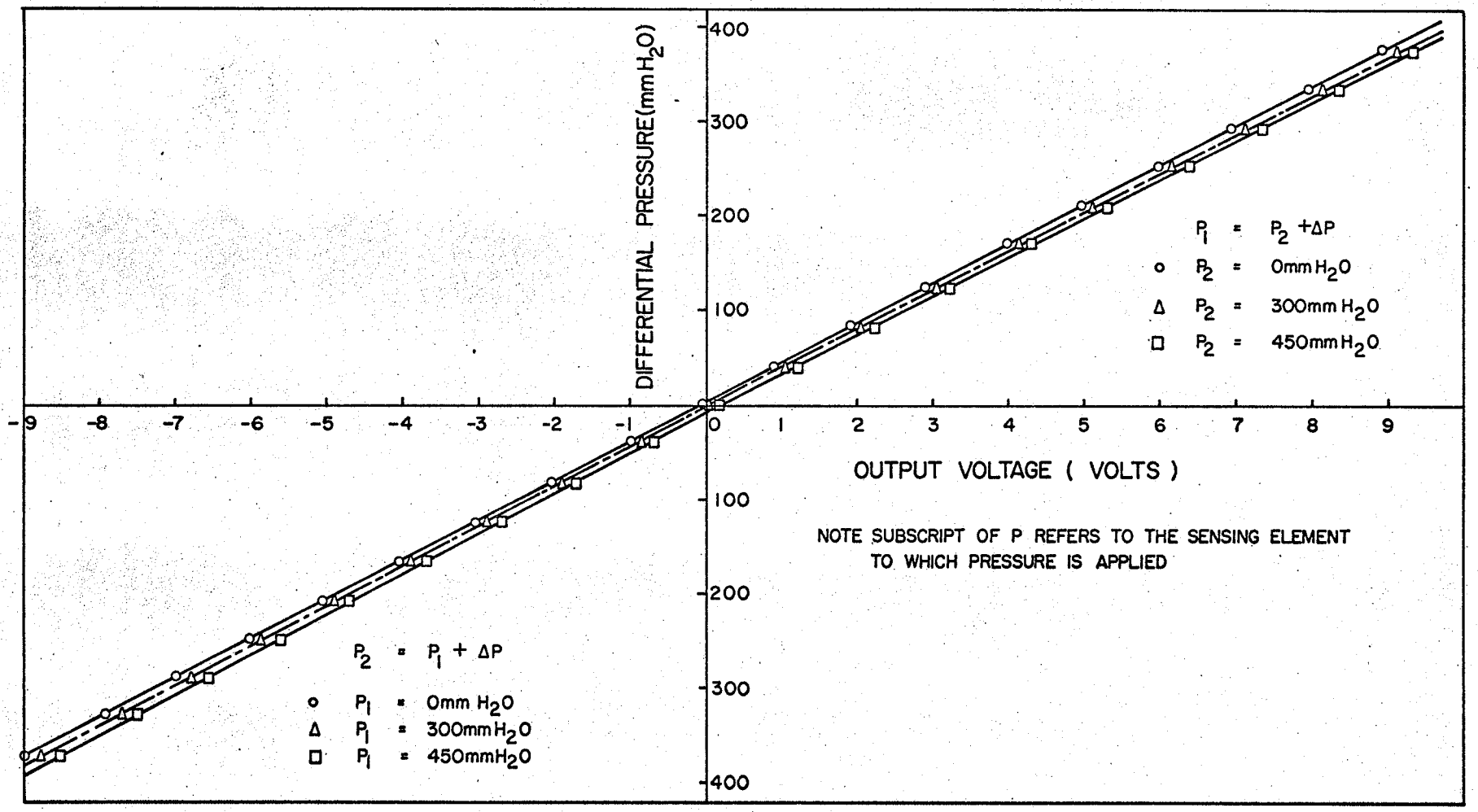

FIGURE 1.7 A CALIBRATION CURVE FOR THE DIFFERENTIAL MODE OF OPERATION OF THE PRESSURE TRANSDUCER.

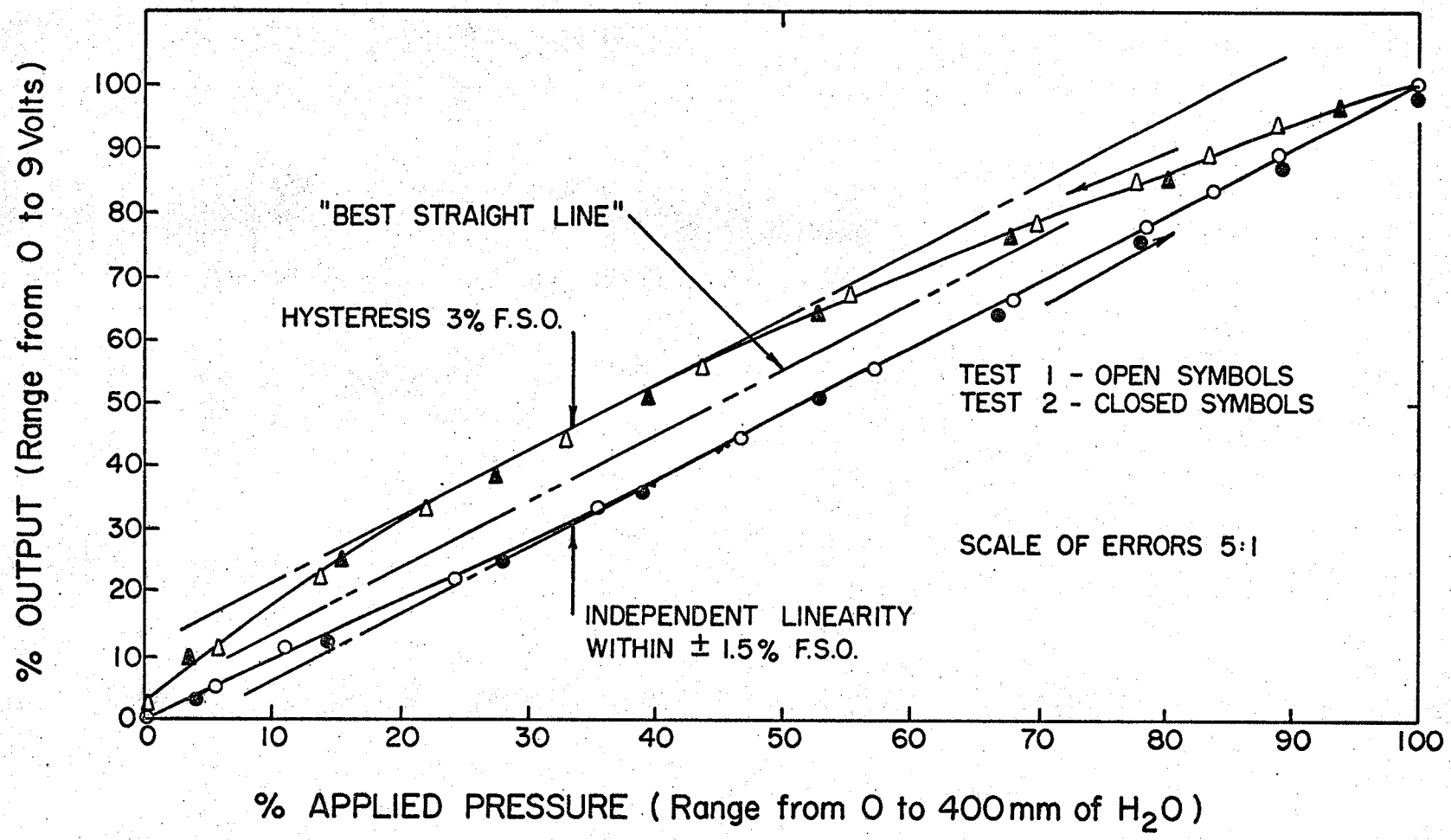

FIGURE 1.8 TYPICAL CALIBRATION CURVE FOR A SINGLE SENSING ELEMENT SHOWING THE LINEARITY, HYSTERESIS AND REPEATABILITY OF THE DATA.

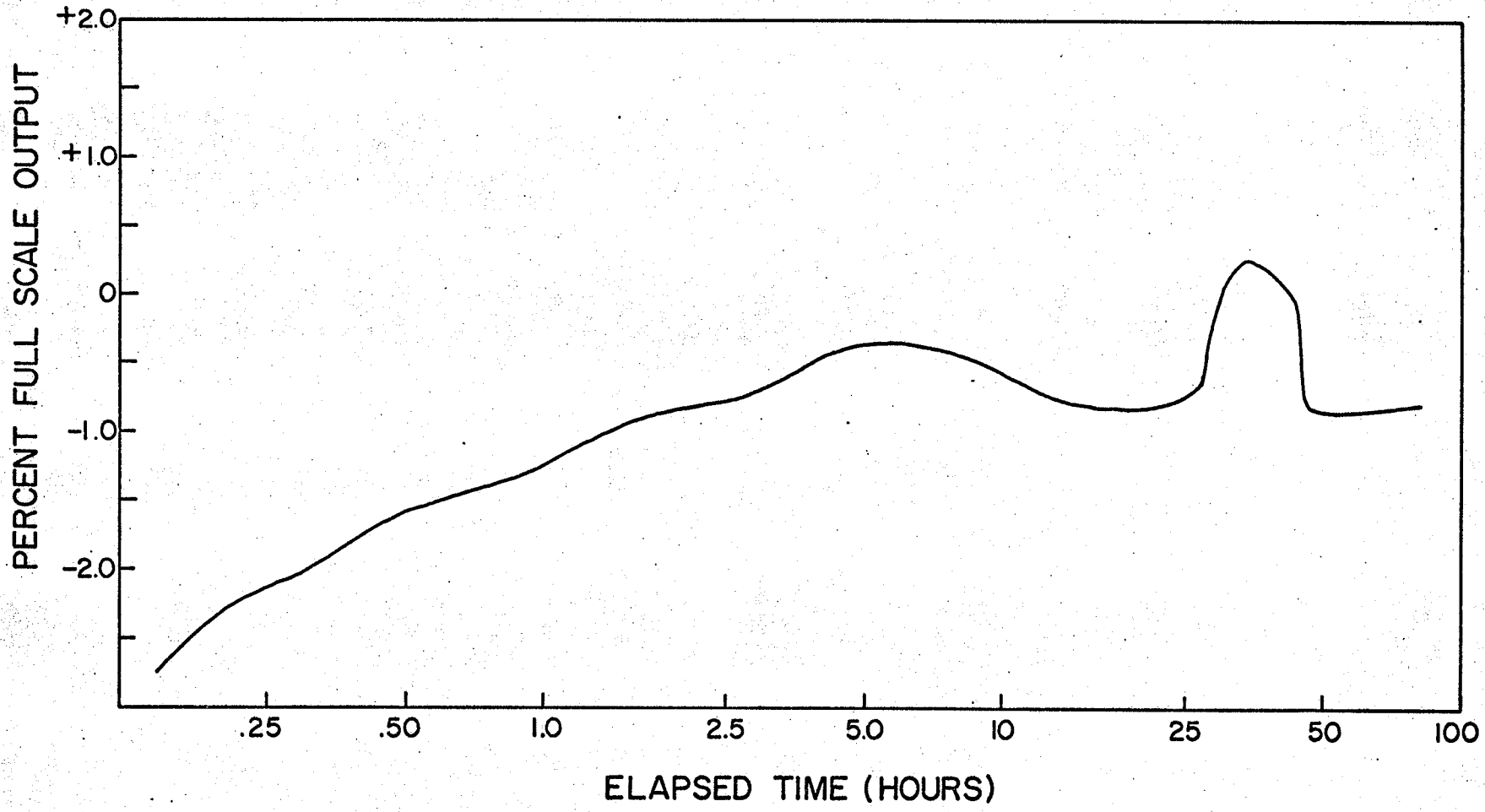

FIGURE 199 RESULTS FROM A D.C. STABILITY TEST PERFORMED ON THE INSTRUMENT WITH CONTINUOUS MONITORING FOR 82 HOURS, FROM THE SWITCHED ON CONDITION.

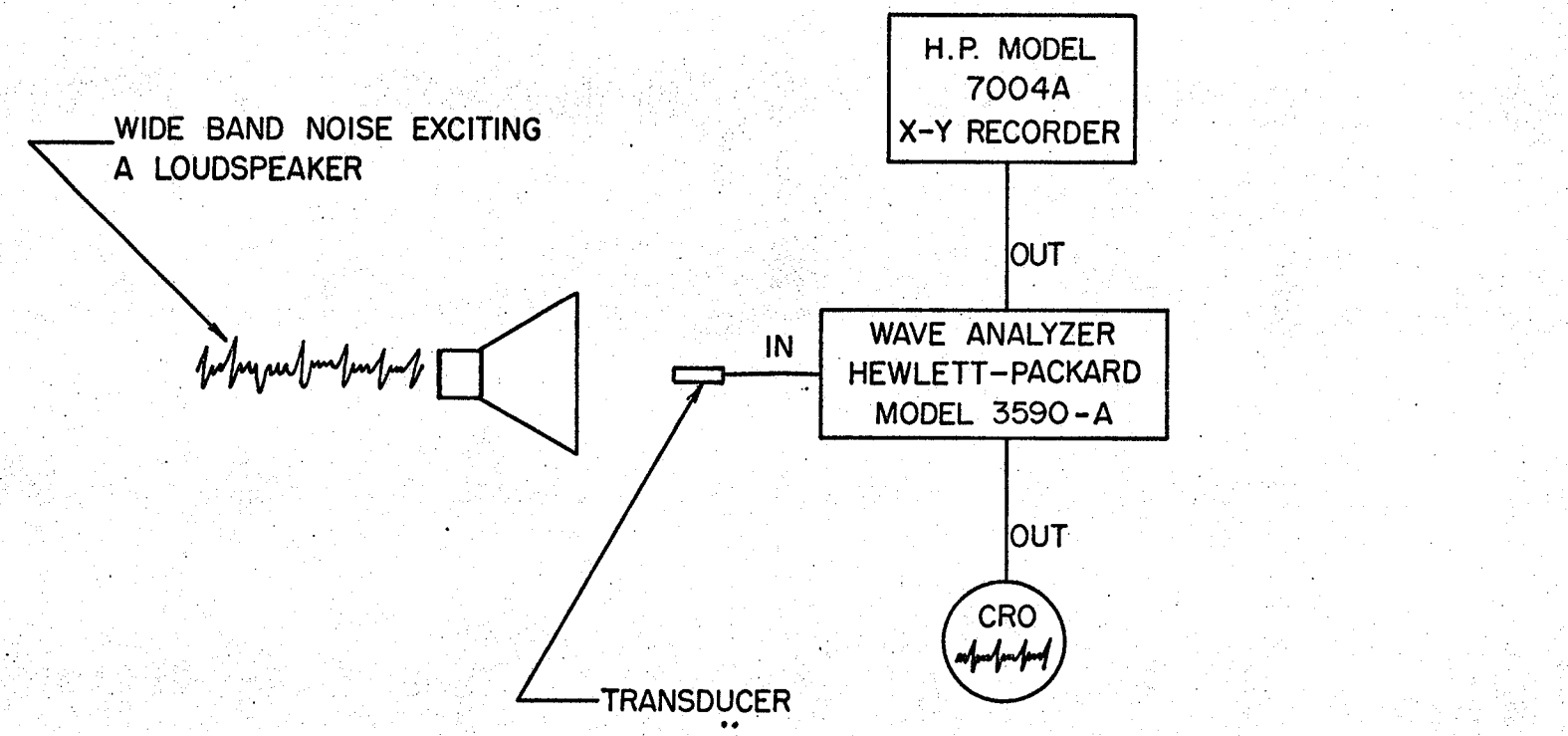

FIGURE 1.10 SCHEMATIC DIAGRAM SHOWING THE EXPERIMENTAL ARRANGEMENT USED TO DETERMINE THE FREQUENCY RESPONSE OF THE PRESSURE TRANSDUCER.

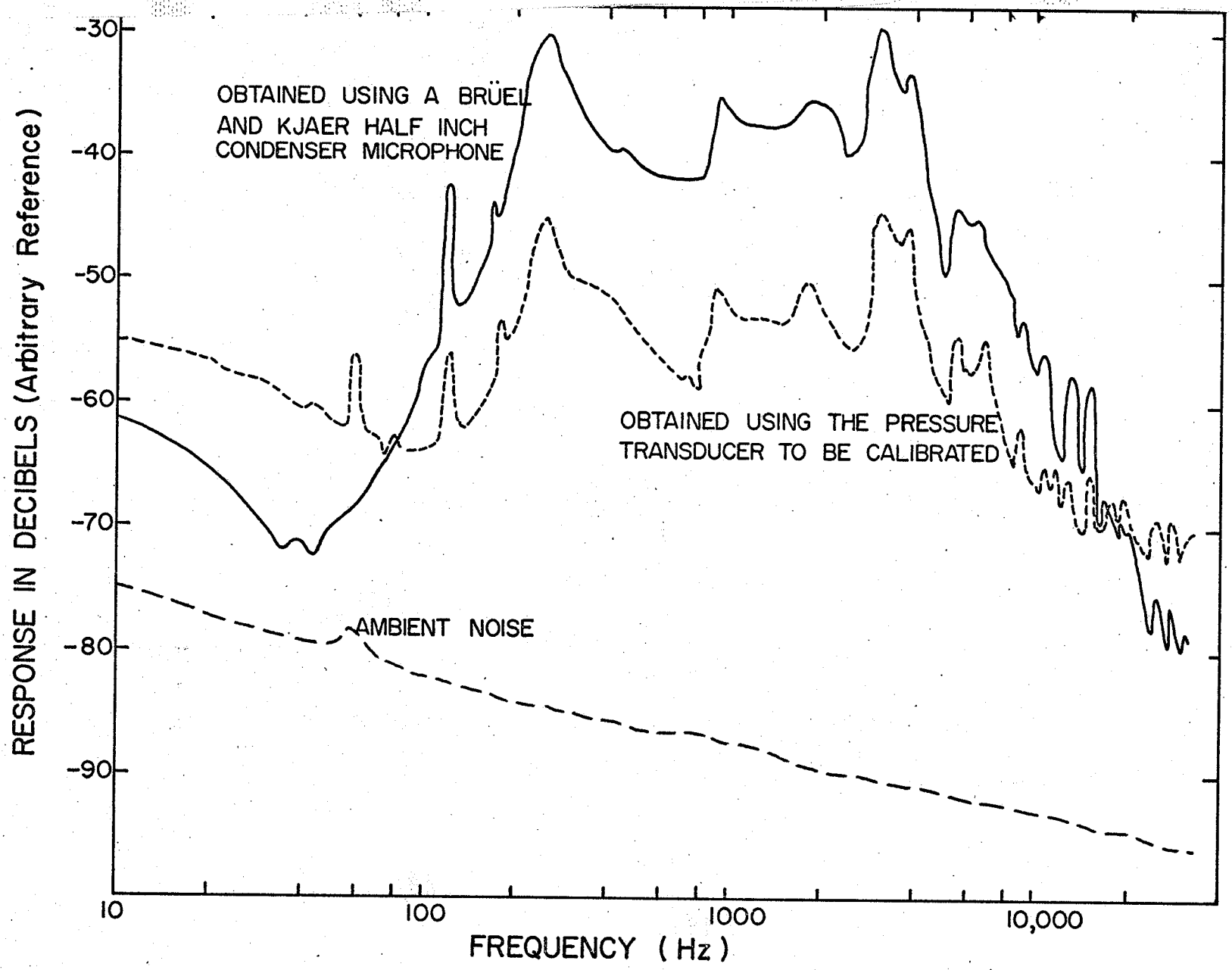

FIGURE 1.11 POWER SPECTRAL DENSITY CURVES OBTAINED FROM THE DYNAMIC CALIBRATION.

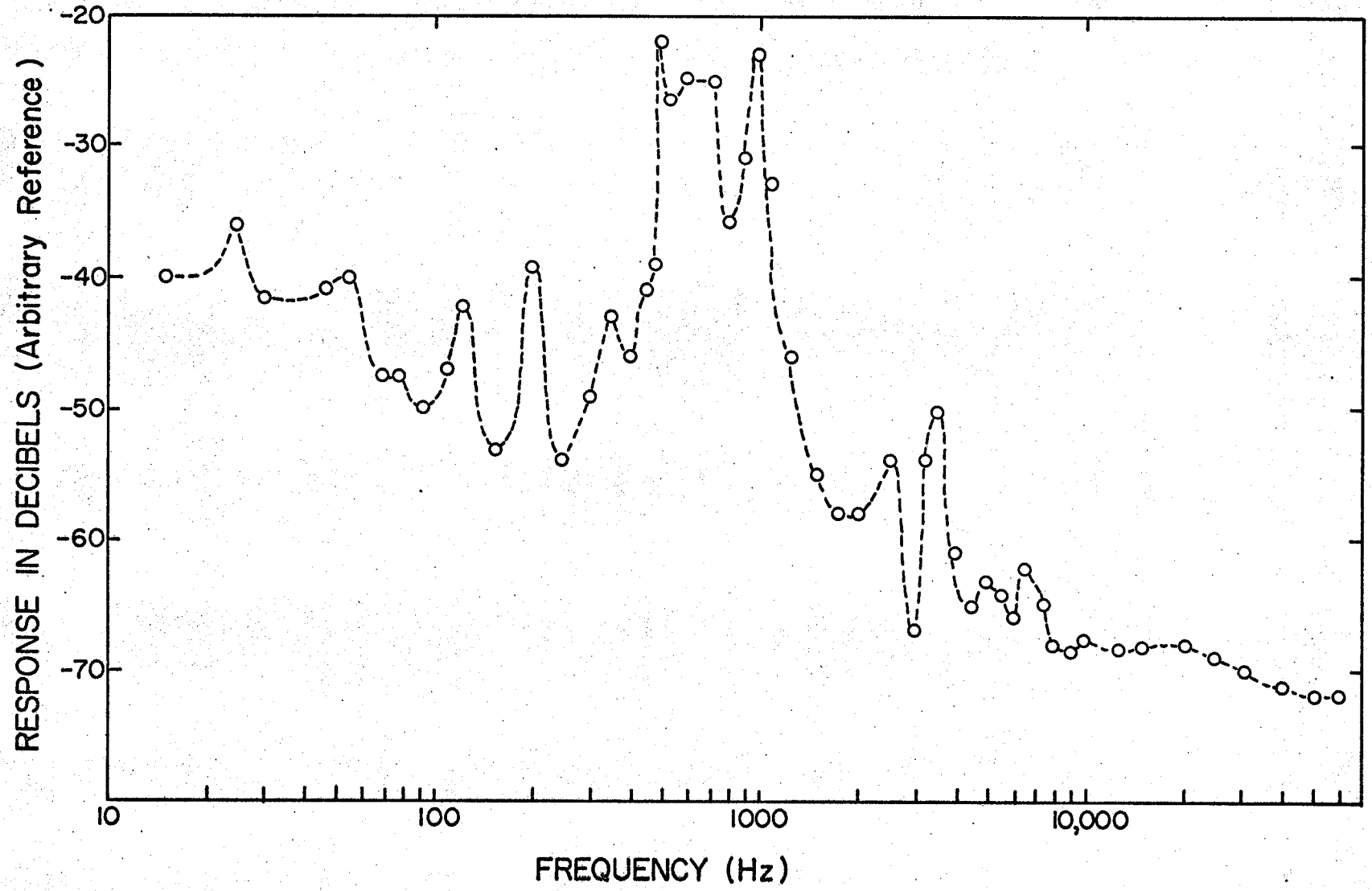

FIGURE 1.12 POWER SPECTRAL DENSITY CURVE OF THE WIND TUNNEL STRUCTURE VIBRATIONS AS MEASURED USING A BRÜEL AND KJAER ACCELEROMETER.

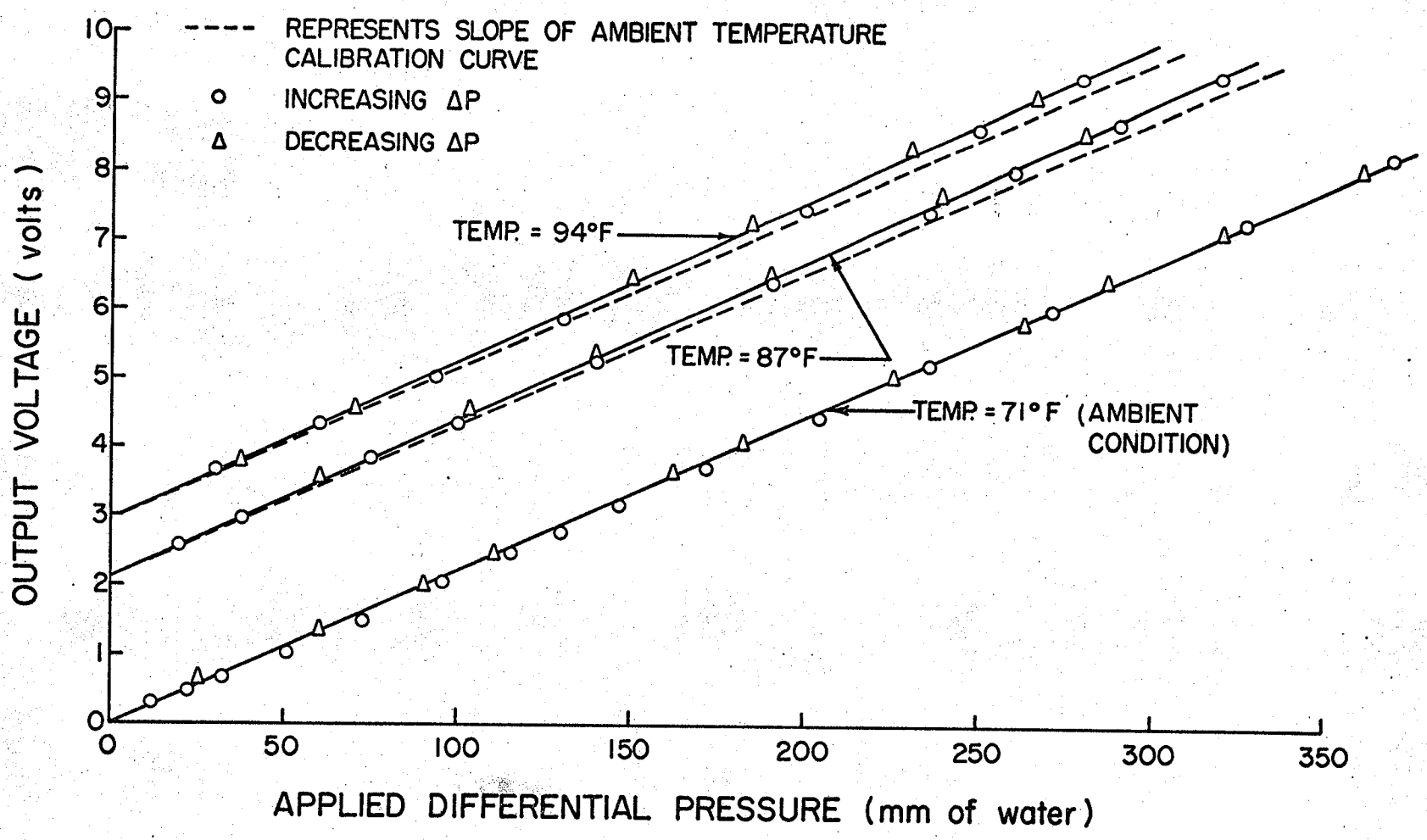

FIGURE 1.13 THERMAL EFFECTS ON STATIC CALIBRATION OF PRESSURE TRANSDUCER.

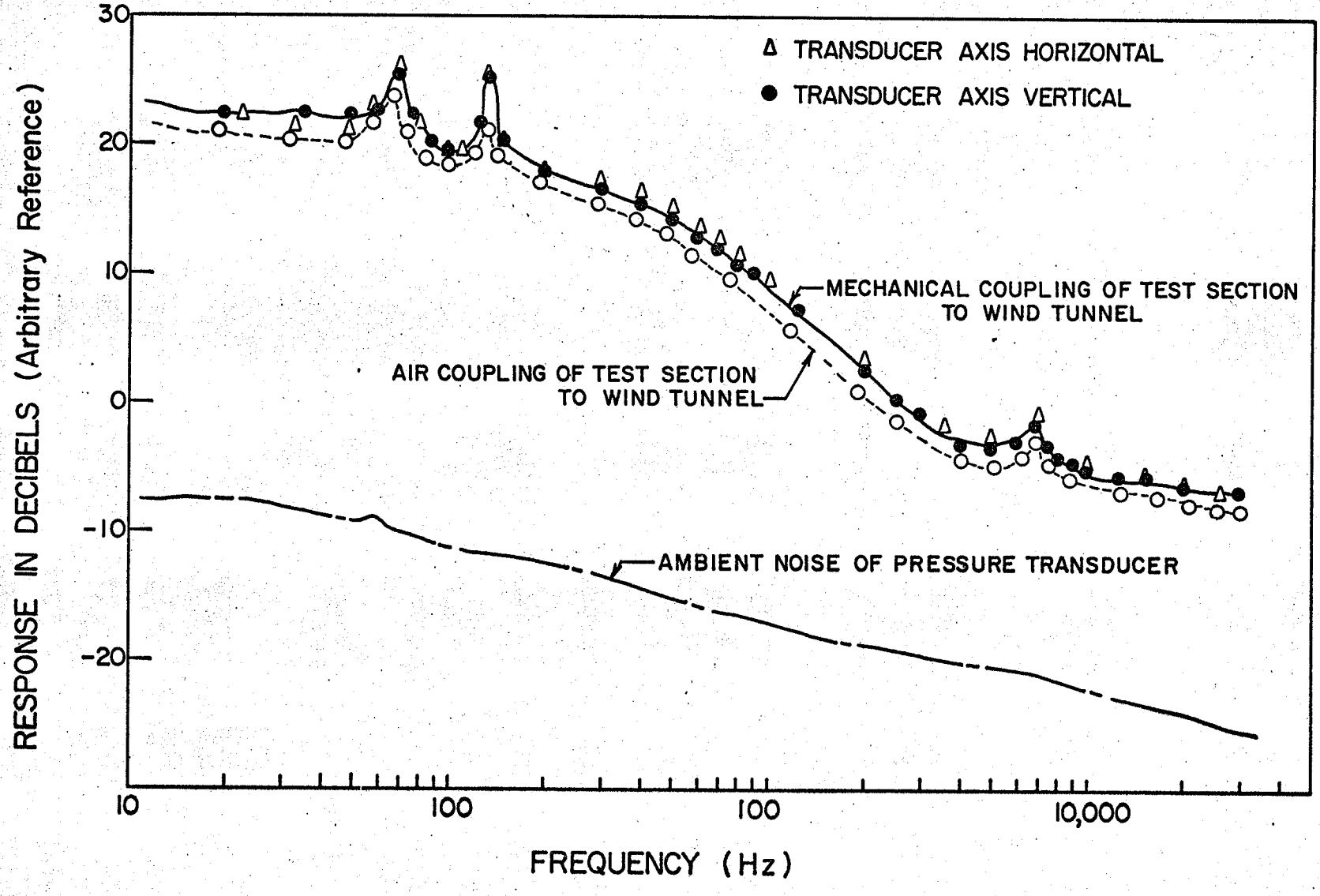

FIGURE 1.14 ENERGY SPECTRA FROM VIBRATION TESTS.

CHAPTER 2

EQUIPMENT AND EXPERIMENTAL PROCEDURES

2.1 Wind Tunnel Facilities.

The experiments were carried out in the low speed wind tunnel facilities of the Turbulence Laboratory, at the University of Manitoba. A schematic drawing showing the general layout of the tunnel and location of the test section is given in Figure 2.1. The air moving device consisted of a variable speed centrifugal fan, capable of producing center line velocities in the test section from 60 feet per second to 250 feet per second. Detailed information with regards to the flow straighteners, contraction cone and diffuser was given by Krueger (1970) and Freison (1970). The section after the contraction cone consisted of sections of smooth (25 μ rms) pipe with a 10 cm internal diameter. This smooth pipe allowed the turbulent boundary layer to develop naturally without any tripping devices. With this arrangement for allowing the flow to develop, it was possible to study a developing turbulent boundary layer as found in pipe flow.

The flow was studied in detail in the test section located at the inlet to the diffuser. Figures 2.1 and 3.1 show the positions of the test section with respect to the rest of the wind tunnel.

2.2 Instrumentation.

2.2.1 Pressure Measurements.

The fluctuating wall pressures were measured using the pressure transducer described in Chapter 1. Figure 1.2(b) shows how the transducer was mounted in the test section. The calibration of the transducer was described in section 1.3 with its dynamic characteristics showing a flat frequency response from 0 to 20 KHz and a thermal sensitivity shift of 0.015% per degree Fahrenheit, based on a calibration performed at ambient room conditions.

The static wall pressures were measured using a Betz micromanometer capable of measuring differential pressures of up to 400 mm of water, while the differential pressure across the contraction cone was measured using a Disa type 134b Micromanometer.

2.2.2 Velocity Measurements.

The fluctuating velocities were measured with constant current hot-wire equipment manufactured by Disa. The anemometers used were the Disa type 55D25 and type 55D01, with the outputs linearized using the Disa type 55D10 Linearizer. The performance characteristics and operating details for the above units are given in their respective instruction manuals.

When using the X-probe to measure the u and v components of the velocity field it was necessary to use two anemometers. As the sum and difference of the signals from each anemometer were used in the determination of the separate velocity components, it was necessary for the time lag in both anemometer circuits to be the same. To determine the time lag, the two anemometers were set up as shown in Figure 2.2 using two single wire miniature probes acting as the sensors.

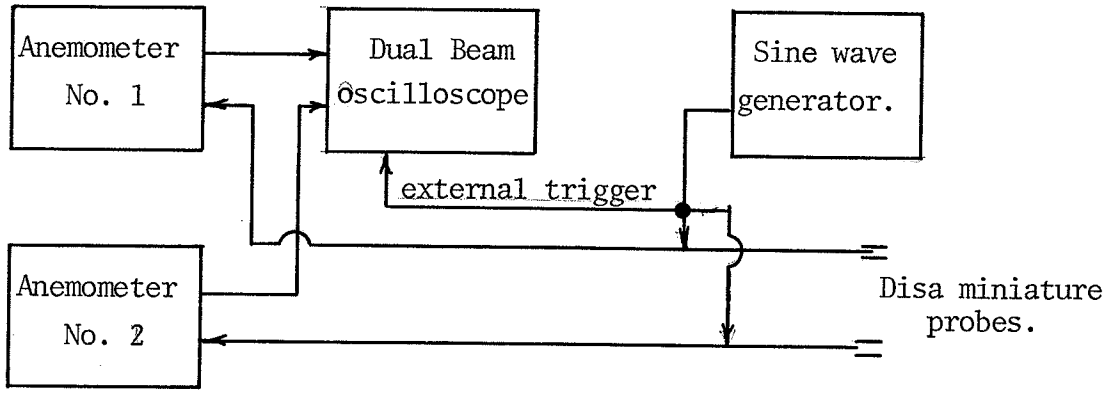

FIGURE 2.3 BLOCK DIAGRAM OF THE TIME-LAG TEST PERFORMED ON THE ANEMOMETERS.

With the anemometers in the operating condition, a sinusoidal signal from the signal generator was superimposed on both inputs from the miniature hot-wire probes. Using a dual beam oscilloscope, triggered externally from the signal generator, the phase lag between the outputs from the two anemometers could be determined by comparing the two wave forms on the scope. The results of the test showed that the solid state anemometer, Disa type 55D01, had a much smaller time lag than the tube type anemometers, Disa type 55D25. Consequently, for the X-probe measurements the older tube type anemometers were used, while for the single wire measurements the newer solid state anemometer was used.

The hot-wire probes used were the Disa 55A38 miniature X-array probes and the Disa 55F04 Boundary Layer Probe. Both probes have a 5 μ diameter platinum-plated tungsten wire with an active length of 1.25 mm, with the boundary layer probe being gold plated at the ends. This construction

ensured a very low level of aerodynamic interference between the sensitive portion of the wire and the prongs and stem body. The X-array probe was used to measure the turbulence intensities of the u and v velocity components and the boundary layer probe was used in the determination of the pressure-velocity correlation coefficient R_{pu} as well as the turbulence intensity of the u velocity component.

The X-probe was mounted in the aerofoil traversing mechanism as shown in Figure 2.3. Many problems were encountered in the use of the belt turning device (part 9 in Figure 2.3) incorporated in the aerofoil of the traversing mechanism. Thus, it was decided to use the X-probe in the aerofoil, without this turning mechanism, and consequently only the u and v components were obtained. For the measurements of the correlation coefficient, the fluctuating velocity in the axial direction, was measured with the boundary layer probe mounted in the traversing mechanism in the same manner as the X-probe.

2.2.3 Analogue Record of Signals.

The signals from the pressure and velocity transducers were recorded on a seven channel Lyric TR61-2 F.M. tape recorder. The recorder could operate at a tape speed of .6, 6 and 60 inches persecond with the corresponding upper frequency limits of 200, 2000 and 20,000 Hz respectively. A feature of this tape recorder was the playback unit which was designed with one movable head to allow the introduction of a time delay between a pair of signals. This was the time delay used for the determination of the auto-correlation function as described in section 4.1.

More detailed specifications for the tape recorder are found in its operating and maintenance manual.

2.2.4 Power Spectrum Measurements.

The power spectrum of both the pressure and velocity fluctuations were measured using a Hewlett-Packard Model 3590 A wave analyzer and a Radiometer Model FRA-2c wave analyzer. Both are constant bandwidth heterodyne type analyzers with the latter having the advantage of a narrower frequency bandwidth (2Hz vs 10Hz) while having the disadvantage of a lower, upper frequency limit (16KHz vs 620KHz). It was observed that the spectrum obtained with the narrower bandwidth analyzer did not present any more information than that taken using the wider bandwidth analyzer. Due to this, and the fact that the Hewlett-Packard wave analyzer could be used directly with the XY-recorder, all spectra presented were made using the Hewlett-Packard model.

The internal rms meter of the analyzer was found to be inadequately damped, and it was necessary to increase the time constant of the meter from 1 second to 10 seconds in order to read the meter.

To provide greater frequency stability to ensure precise tuning, a Hewlett-Packard sweeping local oscillator Model 3594A was used in conjunction with the wave analyzer. With this unit it was possible to sweep the desired frequency range both automatically and manually. Another useful feature of this local oscillator was the digital frequency display.

2.2.5 Vibration Measurements

The vibration tests carried out on the wind tunnel were performed using a Brüel and Kjaer piezoelectric accelerometer, type 4339. The individual calibration curve (reproduced in Figure A-2) supplied with the accelerometer showed a dynamic range from 10Hz to 20 KHz with an undamped natural frequency of 46KHz. A block diagram of the instrumentation used for the vibration measurements is shown in Figure 2.4 using the Brüel and Kjaer Precision Sound Level meter, type 2203, as an amplifier.

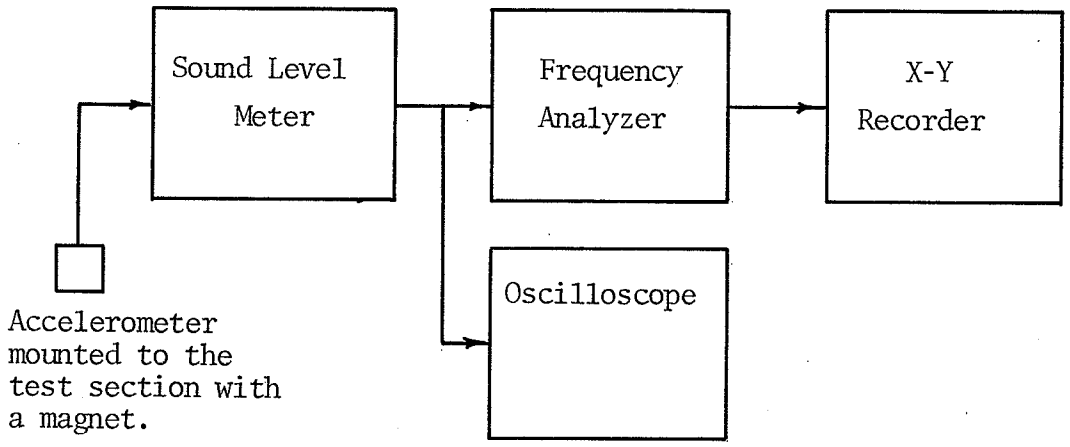

FIGURE 2.4 BLOCK DIAGRAM OF THE INSTRUMENTATION FOR THE VIBRATION MEASUREMENTS.

2.2.6 Sound Measurements.

The condenser microphone which was used in the qualitative dynamic calibration of the pressure transducer was a Brüel and Kjaer half inch condenser microphone. As there was no preamplifier for the microphone the Sound Level meter had to be used as an amplifier as was the case with the accelerometer.

The microphone was recently calibrated and the individual calibration curve (reproduced in Figure A-1) showed a flat frequency response from 20Hz to 20KHz with a resonant frequency of approximately 25KHz. These values are for the microphone cartridge with the protection grid over the diaphragm, being mounted on the Brüel and Kjaer cathode Follower type 2614.

When the microphone was used to measure the sound field in the wind tunnel, the faired nose cone was used. This cone was designed to reduce the

aerodynamically induced noise present when the microphone is exposed to high wind speeds.

2.2.7 Correlation Measurements

The Correlation Coefficients R_{pu} were measured using a Disa type 55A06 Random Signal Indicator and Correlator. The principle on which the Correlator worked, required that the rms value of the two input signals be equal. This was accomplished by adjusting the gain of the output amplifiers of both the pressure transducer and the hot-wire anemometers.

More detailed information on the operating principle of the Correlator can be obtained from the appropriate instruction manual.

2.2.8 Monitoring Equipment.

All electrical signals were visually monitored using a Telequipment Type D35-A Dual Beam Oscilloscope. The root-mean-square measurements were made with a Disa Type 55D35 true rms meter with variable damping facilities incorporated in it. This feature is useful for measurements in fluid mechanics where large fluctuations are likely to occur, as optimum averaging times could be selected. The D.C. voltages were measured using a Disa Type 55D30 voltmeter which features an adjustable attenuation with a digital readout.

More detailed information with regards to the performance characteristics of the above units are available in their respective operating manuals.

2.3 Calibration Methods.

2.3.1 Calibration of Hot-Wire Probes

Temperature tests showed that the operating temperature of the wind tunnel was some $10^{o}F$ higher than that in the miniature tunnel of the Disa type 55D41 Calibration Equipment. This equipment had been used for calibration of the hot-wire probes by previous investigators (Slusar (1969), Freison (1970) and Krueger (1970). However, the difference in operating temperatures could cause considerable errors in the hot-wire calibration. Thus, it was decided to calibrate the hot-wire probes in the test section of the wind tunnel. To accomplish this, the wind tunnel was first calibrated by measuring the mean velocity profiles (results shown in Figure 2.5) in the test section, for various flow speeds, using the pitot tube arrangement as shown in Figure 2.6. The pressure drop across the contraction cone of the tunnel was measured, as well as the tunnel air temperature at each speed. From this data, a calibration curve for the center line velocity, and the average velocity in the test section of the wind tunnel was determined as shown in Figure 2.7. Using this calibration curve it was possible to determine the centerline velocity in the test section and hence the hot-wire probes could be calibrated in the environment in which they were to be operated. A typical, linearized, calibration curve for the single wire, boundary layer probe is given in Figure 2.8.

The velocity calibration of the hot-wire probes was checked before and after each tunnel run when the spectral density and the turbulence intensity measurements were being made.

2.3.2 Calibration of Pressure Transducer.

The calibration of the pressure transducer was performed using the differential static calibration unit shown in Figure 1.5. The details of

the static and the dynamic calibration of the transducer are described, in detail, in section 1.3.

When the root mean square pressure and spectral density measurements were being made, the calibration was checked before and after each tunnel run.

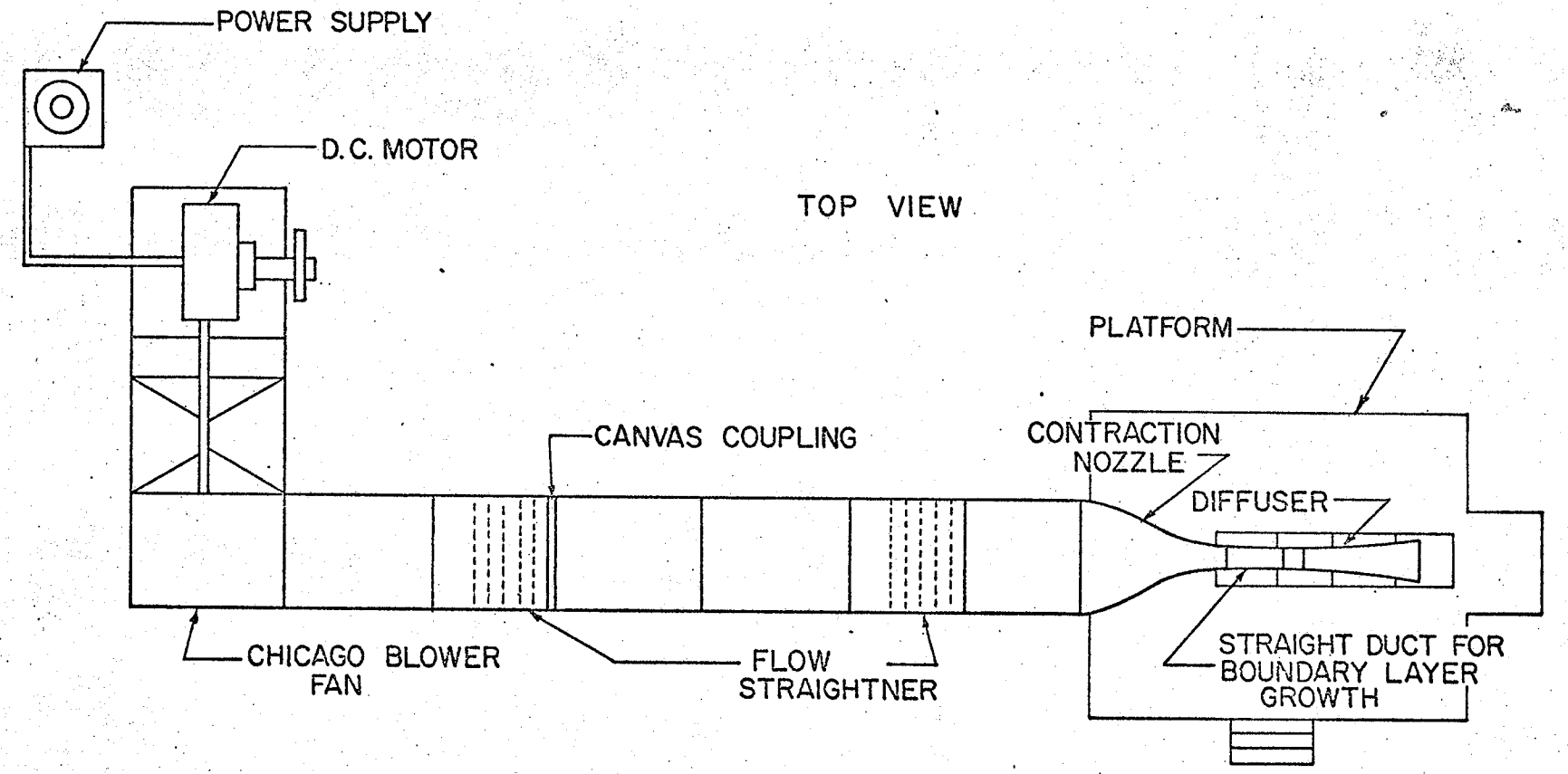

FIGURE 2.1 SCHEMATIC DIAGRAM OF THE WIND TUNNEL FACILITIES.

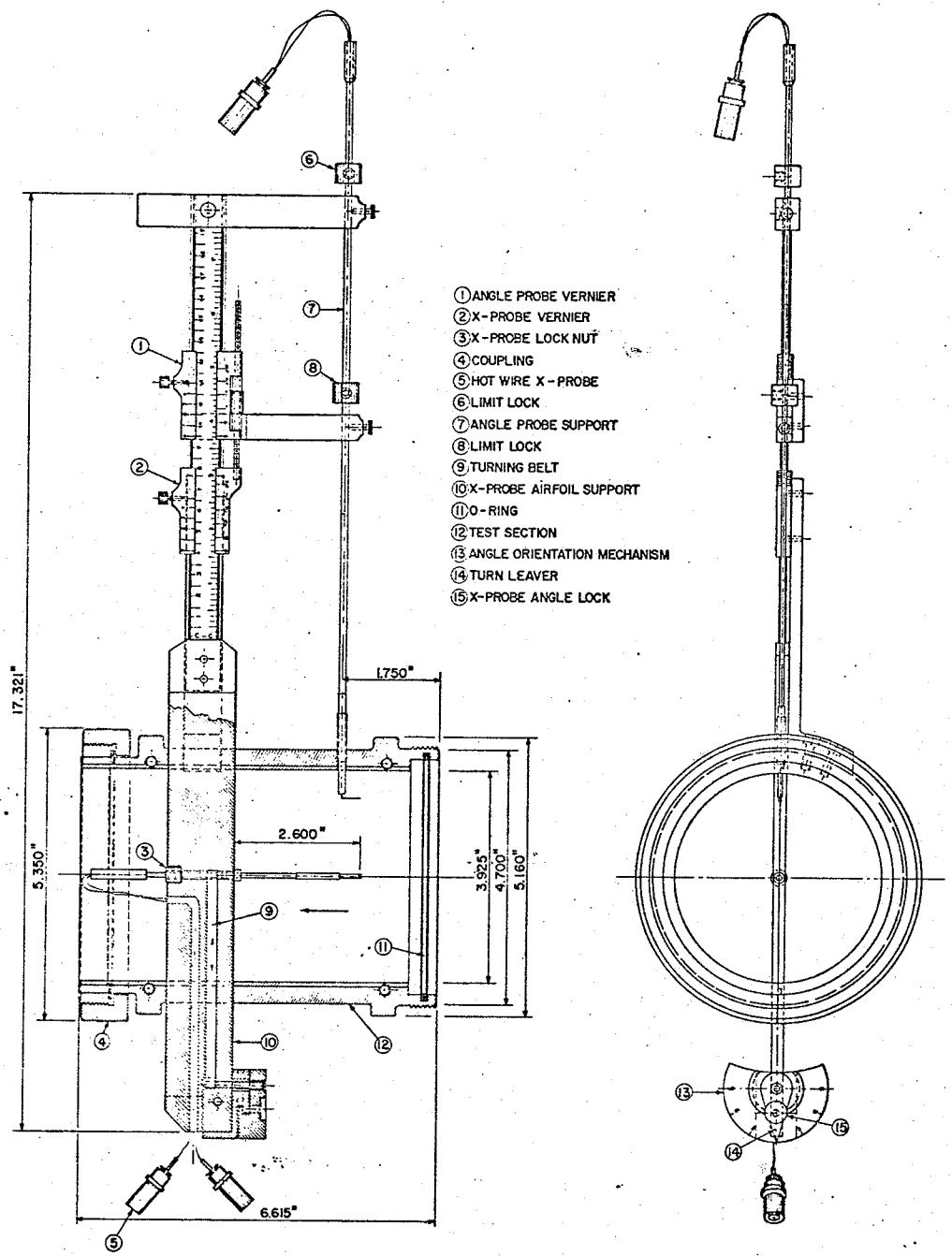

FIGURE 2.2 PIPE TRAVERSING MECHANISM.

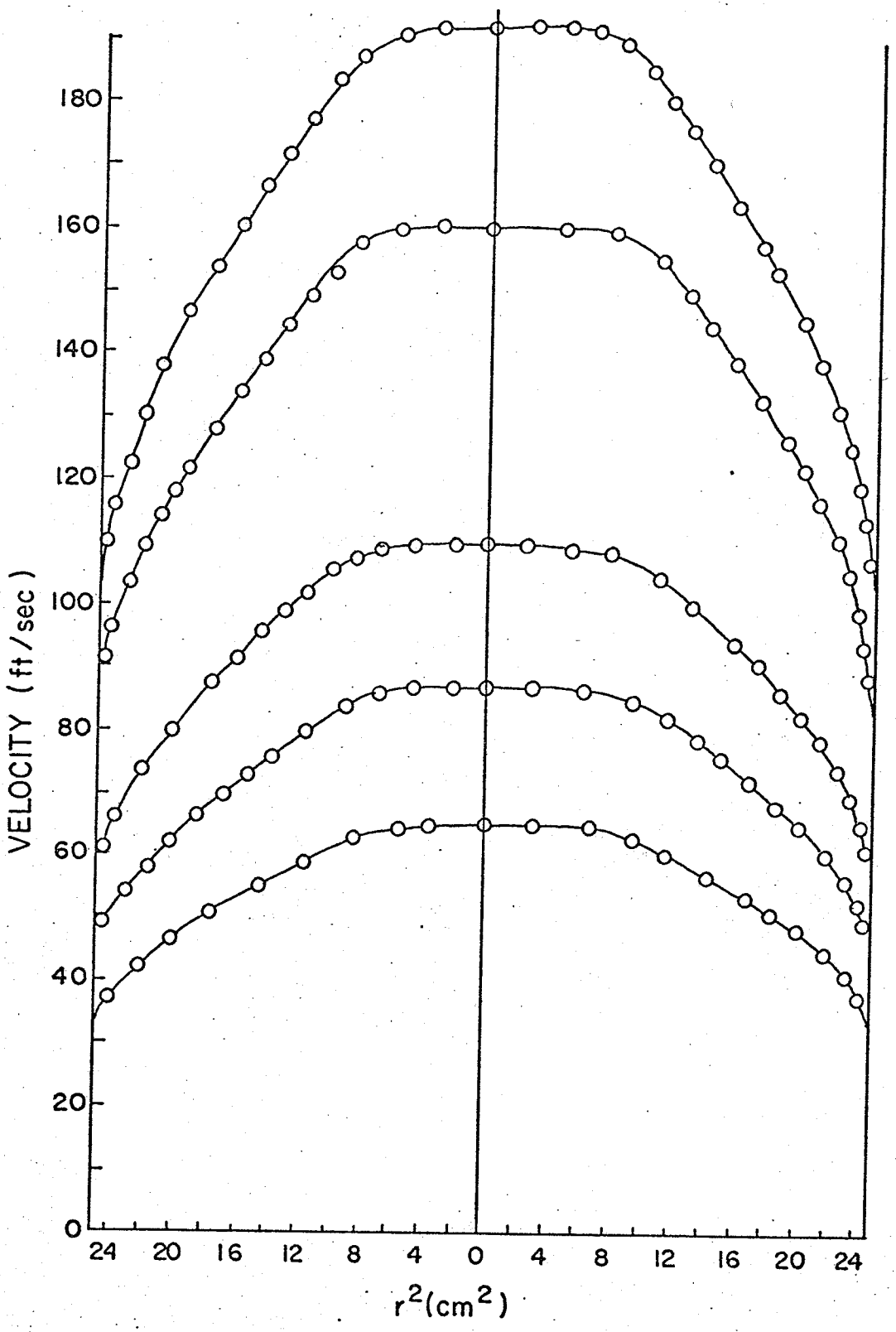

FIGURE 2.5 MEAN VELOCITY PROFILES OBTAINED USING THE PITOT TUBE TRAVERSING MECHANISM.

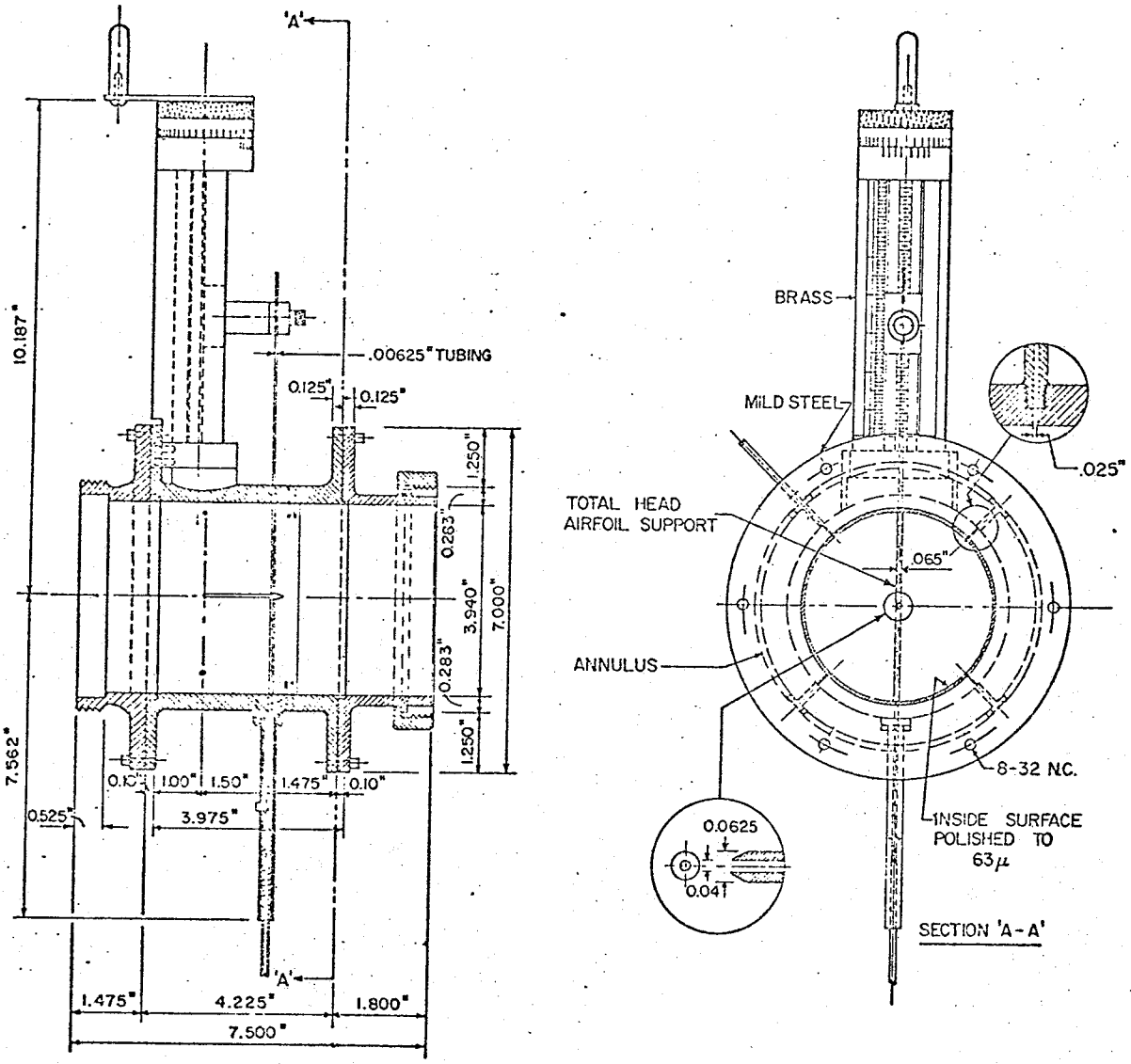

FIGURE 2.6 PITOT TUBE TRAVERSING MECHANISM

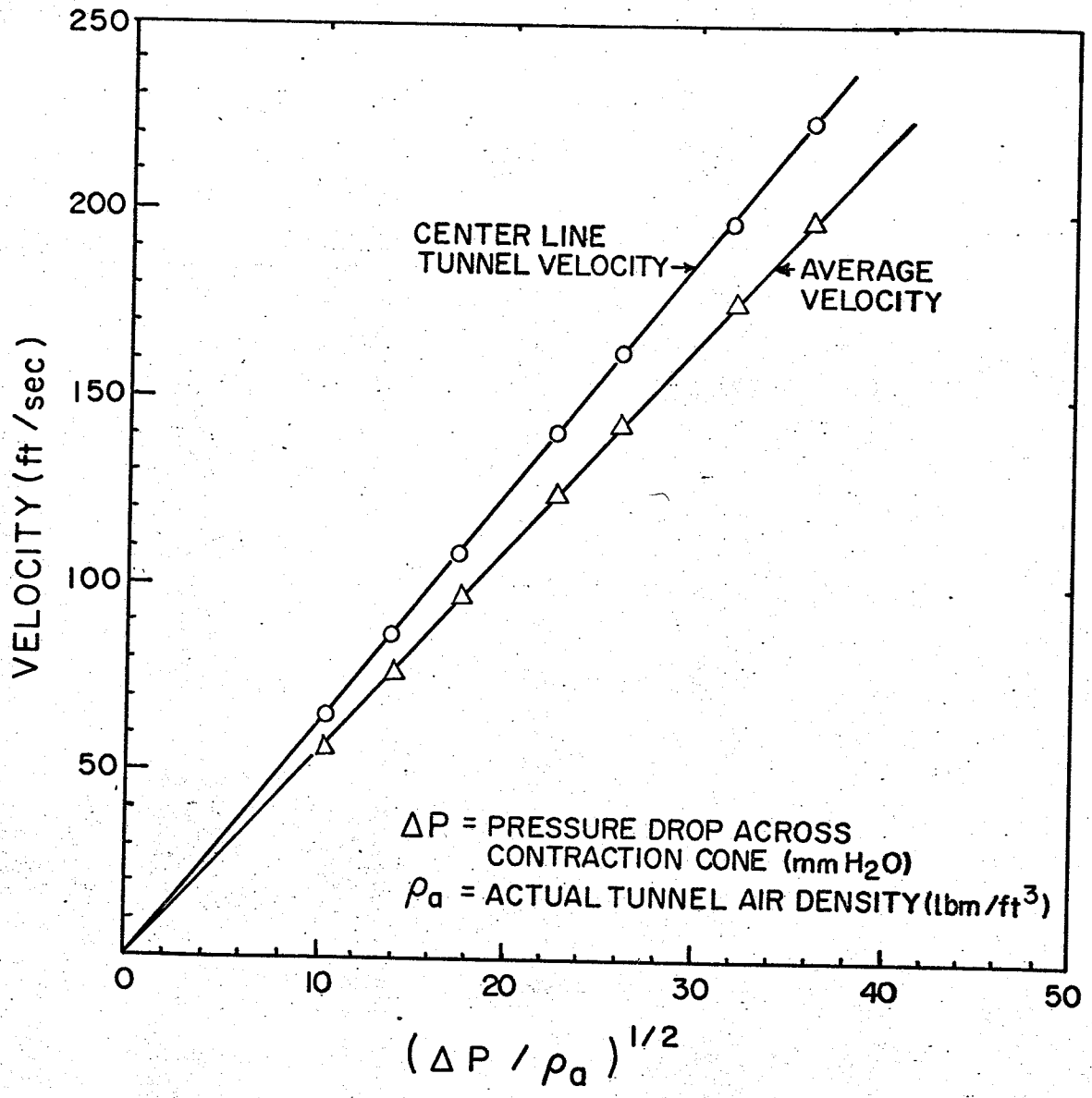

FIGURE 2.7 CALIBRATION CURVE OF WIND TUNNEL BASED ON PRESSURE DROP ACROSS CONTRACTION CONE AND TUNNEL AIR DENSITY.

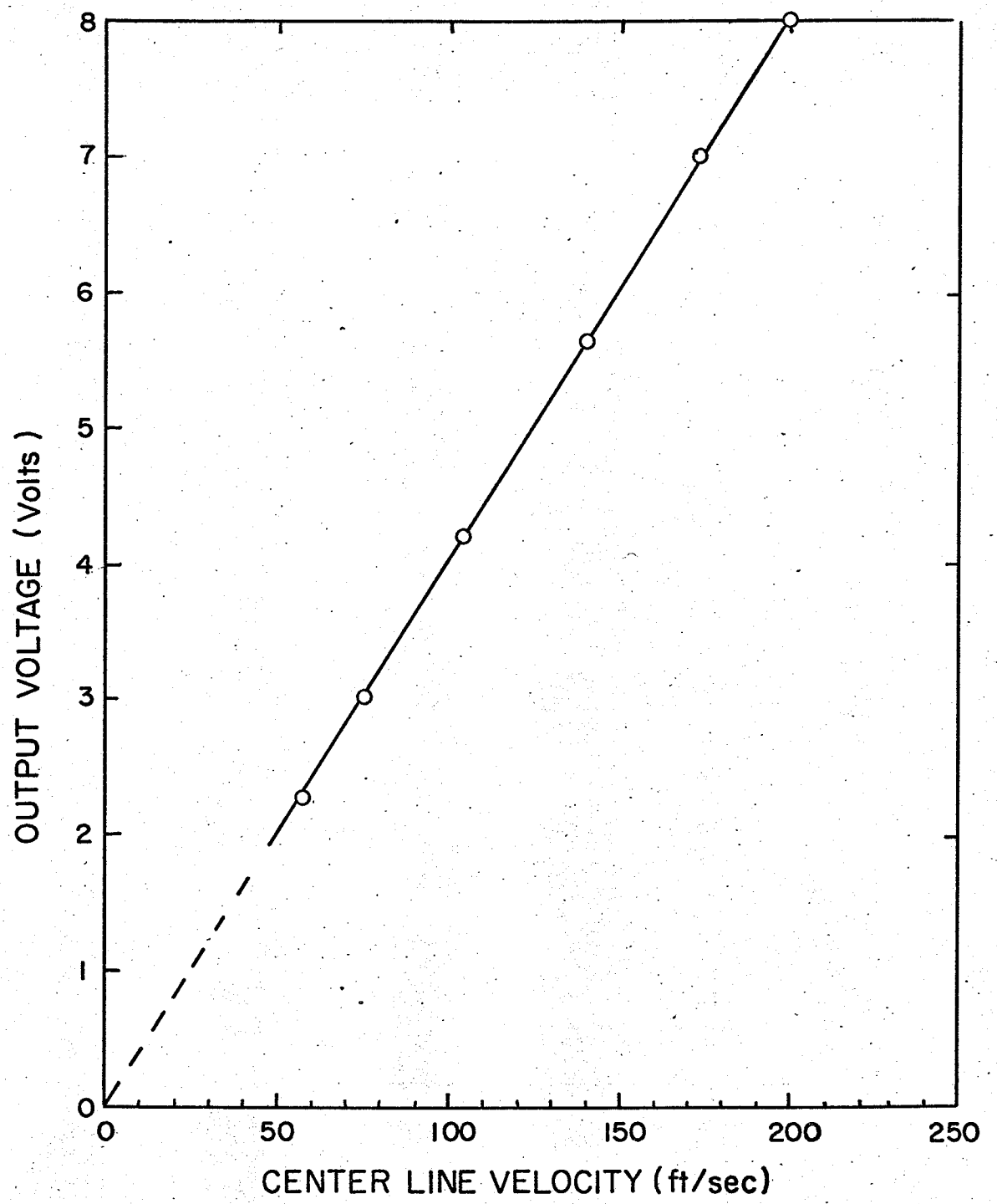

FIGURE 2.8 A TYPICAL, LINEARIZED CALIBRATION CURVE FOR A SINGLE WIRE BOUNDARY LAYER PROBE.

CHAPTER 3

CHARACTERISTICS OF THE FLOW FIELD.

3.1 Introduction

The turbulence measurements of this investigation were conducted in the test section of the wind tunnel as shown in Figures 2.1 and 3.1. Because the entrance length (L=17.5 D) was not long enough to promote fully developed pipe flow (this usually requires L>30 D), the turbulent boundary layers studied were those of a developing pipe flow. As mentioned previously in Section 2.1.1 the boundary layer was allowed to develop naturally. This fact is important when comparing boundary layer properties with other investigators, as Willmarth and Wooldridge (1963) have shown that an artificial tripping of the boundary layer, from laminar to turbulent conditions, changes the structure of the turbulence.

The mean velocity profiles and boundary layer thicknesses for the flow rates under consideration were obtained from Pitot tube measurements, and by using graphical integration methods on the mean velocity data, displacement thicknesses and momentum thicknesses were also determined. The turbulent intensity levels of the flow were measured using the hot-wire equipment.

A schematic diagram of the test section with the boundary layer growth pipes is given in Figure 3.1. In this figure, the zero reference position is located 3.25 inches from the flange on the exit of the contraction cone with the separation vectors ξ_1 and ξ_2 shown in the exploded view of the test section.

3.2 Characteristic Thicknesses of Boundary Layers.

In the following subsections, the definitions of the boundary layer thickness, the displacement thickness, and the momentum thickness will be presented. The definition for the turbulence intensities will be omitted, as it is covered in Section 3.3.

A summary of the boundary layer parameters is shown in Table 3.1.

3.2.1 Boundary Layer Thickness (δ)

The definition of the boundary layer thickness is to a certain extent arbitrary, because transition from the velocity in the boundary layer to that outside, takes place asymptotically. However, the definition adopted for the boundary layer thickness is that distance from the wall where the velocity differs by 1% from the external velocity.

3.2.2 Displacement Thickness δ^*

The friction forces present in the boundary layer cause the velocity in this region to be decreased and consequently, the volume flow is also reduced. The decrease in volume flow, compared to the flow which would exist for the condition of no boundary layer in the pipe may be written as:

$$\int_0^R (U_\infty - U)\, 2\pi r dr \qquad 3.1$$

where U_∞ is the free stream velocity.

U is the local mean velocity at r.

r is the radial coordinate measured outwards from the pipe axis.

R is the pipe radius.

The displacement thickness δ^* is defined as the thickness of a region, measured from the wall of the pipe, in which the volume flow would be equal to

this deficient flow volume. Thus, for axi-symmetric pipe flow the following equality holds:

$$\pi U_\infty \left(R^2 - (R - \delta^*)^2\right) = \int_0^R (U_\infty - U)\, 2\pi r dr, \qquad 3.2$$

and in the flow region from r=0 to r=R - δ the contributions to the term on the right hand side are negligible and consequently the lower limit of the integral may be changed to R - δ. Reducing Equation 3.2 and changing the limits result in:

$$2R\delta^* - \delta^{*2} = \int_{R-\delta}^R \left(1 - \frac{U}{U_\infty}\right) 2r dr, \qquad 3.3$$

and by solving this quadratic equation, the displacement thickness can be obtained. Because δ^* is small compared to R, the second order term may be neglected, and the resulting equation for the displacement thickness is:

$$\delta^* = \frac{1}{R} \int_{R-\delta}^R \left(1 - \frac{U}{U_\infty}\right) r dr. \qquad 3.4$$

3.2.3 Momentum Thickness θ

The momentum thickness may be defined as the thickness of a region in the flow, measured from the wall of the pipe, in which the flow would have the same momentum as that which is lost to the flow as a result of friction. This deficient momentum may be expressed as:

$$\rho \int_0^R (U_\infty - U)U\, 2\pi r dr \qquad 3.5$$

where ρ is the fluid density.

r is the radial coordinate measured outwards from the pipe axis.

R is the pipe radius.

U is the local mean velocity at r.

U_∞ is the free stream velocity.

Using an argument similar to the one presented for the displacement thickness,

an equation relating this deficient momentum to the momentum in the region defined by θ is:

$$\rho \pi U_\infty^2 (R^2 - (R - \theta)^2) = \rho \int_0^R (U_\infty - U) U \, 2\pi r dr, \qquad 3.6$$

and by changing the limits of the integral, as was done in Section 3.2.2 , this equation reduces to:

$$2R\theta - \theta^2 = \int_{R-\delta}^{R} (1 - \frac{U}{U_\infty}) \frac{U}{U_\infty} \, 2r dr. \qquad 3.7$$

This quadratic equation can be solved to obtain θ, however, as θ is small compared to R, the second order term may be neglected and the resulting equation for the momentum thickness is:

$$\theta = \frac{1}{R} \int_{R-\delta}^{R} (1 - \frac{U}{U_\infty}) \frac{U}{U_\infty} \, r dr. \qquad 3.8$$

3.3 Turbulence Intensities.

3.3.1 General Experimental Procedures.

Another parameter which is important in the description of the flow conditions is the distribution of the levels of the turbulence throughout the flow region. In this study, the intensity profiles of the velocity fluctuations were measured in the frequency band from 20 Hz to 50 KHz. The lower limit was set in order to eliminate the signal due to the large scale fluctuations present in the flow as a result of the action of the centrifugal fan in the wind tunnel. The upper frequency limit was arbitrarily set, as the power spectrum measurements did not indicate any appreciable energy contained in the small scale eddies beyond 50 KHz.

Initially the X-probe was used to measure the root-mean-square values of the fluctuating u and v velocity components. The results are shown in Figure 3.2 with the r.m.s. values of the fluctuating velocities being nondimensionalized with the local mean velocity, U. However, it was found that by using the X-probe, the wall of the test section could be approached to a distance of only $\xi_1 = 0.08R$. By using the boundary layer probe the wall could be approached to a distance of $\xi_1/R = 0.02$, but only the fluctuating velocity component in the axial direction could be measured.

It was decided to make a detailed study of the distribution of the turbulent intensities of the axial velocity component of the flow, as the pressure velocity correlations (discussed in Chapter 4) were measured using only the u component of the flow. Intensity profiles were measured at various tunnel speeds along three separate radial traverses, which were axially displaced from one another by the separation vector ξ_2. From these measurements, the gradients $\delta(\sqrt{\overline{u^2}})/\delta\xi_2$ and $\delta(\sqrt{\overline{u^2}})/\delta r$ could be determined, and from the mean velocity profiles the gradients $\delta U/\delta r$ were also determined.

3.3.2 Discussion of Results.

The turbulent intensity profiles of the fluctuating axial component of the velocity have been measured using both an X-probe and a boundary layer probe. The measurements taken using the X-probe, show both the u and v turbulence intensity profiles (see Figure 3.2) with the latter being approximately 40% lower in the boundary layer than the former. This result agrees with the general trend of the intensity profiles as reported by Klebanoff (1954) and Willmarth and Wooldridge (1963) for a flat plate and by Laufer (1954) for fully developed pipe flow.

As the same quantities were measured using two different hot-wire probe configurations operating under essentially the same flow conditions, it was possible to compare the results with one another. From Figure 3.2 it can be seen that the u intensity profiles compare favourably with one another in the boundary layer region. However, in the region outside the boundary layer, the X-probe measurements indicated a turbulence intensity level of 1.5% while the boundary layer probe gave values of 0.6%.

When using the X-probe for the measurements of the intensity levels, it was necessary to take the signal from each of the hot-wires on the probe, and form the instantaneous sum and difference of the two signals. The root-mean-square values of the two new signals were then obtained, and by using a procedure outlined in the instruction manual for the Disa Random Signal Correlator, the turbulence intensities were determined. With the single wire boundary layer probe, there was no need for the above electronic manipulation of the signals in order to obtain the intensity profiles as shown in Figure 3.3 because the r.m.s. values of the signal could be obtained directly using an r.m.s. meter.

The electronic noise in the adding and subtracting circuits of the Correlator could have introduced errors into the X-probe measurements in

the outer region of the flow where the turbulence intensity level was low. As the intensity of the signal from the probe increased, the signal to noise ratio increased and consequently the effect of the electronic noise was decreased. This would explain the good agreement between the two tests in the boundary layer region, because the level of the turbulence intensity in this region was much higher than in the free stream. It was felt that the u intensity profiles obtained using the boundary layer probe were more reliable, because less signal conditioning was required.

Figure 3.3 shows the turbulence intensity profiles of the fluctuating component of the axial velocity, measured along a radial traverse of the test section using the boundary layer probe. The turbulence intensities show a definite dependency upon the free stream velocity, U_∞. In the region outside the boundary layer ($\xi_1/R > .6$), the intensity levels increased with increasing free stream velocities and reached a maximum at a speed of 172 feet per second. As the mean flow rate was increased further, the results indicate a slight decrease in the level of the turbulence intensities. In the inner region of the flow field ($\xi_1/R < .5$), the velocity dependency was reversed, with the intensity levels decreasing for increasing free stream velocities. This trend did not change at the speed of 172 feet per second as was the case in the outer region. In the next chapter, the importance of the phenomena occurring at free stream velocities near 170 feet per second will be discussed in relation to the correlation measurements.

A comparison of the turbulence intensity measurements of the fluctuating component of the axial velocity with turbulence intensities as reported by Laufer (1954) is given in Figure 3.4. Laufer found that by using the shear velocity U^* as a characteristic velocity parameter, the various velocity distributions become independent of the flow Reynolds number.

Consequently, to compare the results of this investigation to those of Laufer, the r.m.s. values of the fluctuating u component were nondimensionalized using the shear velocity. For the calculation of the shear velocity, the wall shear stresses were obtained from pressure drop measurements. Also shown in Figure 3.4 are the results of Willmarth and Wooldridge (1963) which were obtained in a two dimensional boundary layer for $R_\theta = 38{,}000$. It can be seen that the $\sqrt{\overline{u^2}}/U^*$ values obtained in this investigation compare reasonably well with those reported by Laufer for a fully developed, pipe flow and by Willmarth and Wooldridge for a two dimensional boundary layer.

Figure 3.5 shows the distribution, along a radial traverse, of the r.m.s. values for the fluctuating u component of the velocity. From this figure it can be seen that as the free stream mean velocity was increased, the value of the fluctuating velocities also increased, but with a percentage increase slightly lower than that of the mean flow. By numerical differentiation of the boundary layer data presented in Figure 3.5, the velocity gradients $(\delta\sqrt{\overline{u^2}}/\delta r)$ were obtained, as shown in Figure 3.6. For the description of these velocity gradients, the convention adopted was that a positive slope indicated an increase in velocity with increasing r values. Also presented in Figure 3.6 are the gradients of the mean velocity, $(\delta U/\delta r)$, obtained by a numerical differentiation of the mean velocity data used to generate the velocity profiles shown in Figure 2.5.

In the boundary layer, both the $-\delta\sqrt{\overline{u^2}}/\delta r$ and $-\delta U/\delta r$ terms increase in magnitude as the wall is approached $(\xi_1/R=0)$, however, the increase for the mean velocity is much more pronounced than that of the fluctuating velocity, especially in the region near the wall $(0.05<\xi_1/R<0.2)$. From a consideration of the absolute numerical values of the gradients, the curves show that the $\delta\sqrt{\overline{u^2}}/\delta r$ values are at least an order of magnitude lower than those of $\delta U/\delta r$, for $\xi_1/R<0.25$. The importance of this is illustrated in

Appendix A.1 where an order of magnitude analysis is used for the determination of the equation relating the fluctuating wall pressure to the mean velocity gradients .

The velocity gradient $\delta\sqrt{\overline{u^2}}/\delta\xi_2$ was determined from the intensity profiles obtained along the three radial traverses, axially displaced from one another by the separation vector ξ_2. The convention adopted for the description of this velocity gradient was that a positive gradient indicates an increase in velocity for increasing ξ_2 values. The velocity gradients, $\delta\sqrt{\overline{u^2}}/\delta\xi_2$, for free stream velocities of 109.5, 160 and 192.5 feet per second are presented in Figure 3.7. For the lower two velocities, the results show a positive velocity gradient in the outer section of the boundary layer. This indicates that generation of turbulence is still going on in this region for these free stream speeds, while for the higher speed of 192.5 feet per second this is not the case as the gradient is always negative. In the inner region of the boundary layer ($\xi_1/R < 0.22$ for $U_\infty = 109.5$ ft/sec and $\xi_1/R < 0.34$ for $U_\infty = 160$ ft/sec) the negative nature of the velocity gradient shows that a decaying process is taking place. The velocity gradients for the three speeds all reach a minimum in the vicinity of $\xi_1/R = 0.06$ and increase as the wall is approached. This minimum may be due to the high shearing stresses present in the immediate vicinity of the wall.

If one considers the absolute numerical values of the velocity gradients, $\delta(\sqrt{\overline{u^2}})/\delta\xi_2$, it can be seen that they exhibit magnitudes of the order of 10. In comparison, the magnitudes of the velocity gradients, $\delta(\sqrt{\overline{u^2}}/\delta r$ and $\delta U/\delta r$, are of the order of 100 and 1000 respectively.

	Free Stream Velocity, U_∞ (ft/sec)			
	86.5	109.5	160	192.5
$\bar{U}$ (ft/sec)	75.6	95.9	140.8	168.6
δ (ft)	.0785	.0770	.0770	.0932
δ^* (ft)	.0110	.0110	.0110	.0125
θ (ft)	.00771	.00780	.00767	.00765
δ^*/θ	1.430	1.421	1.449	1.432
δ/δ^*	7.09	6.94	6.94	8.54
$R_\theta x10^{-4}$	.3842	.490	.7025	.8440

Table 3.1 A Comparison of the Boundary Layer parameters for different flow rates.

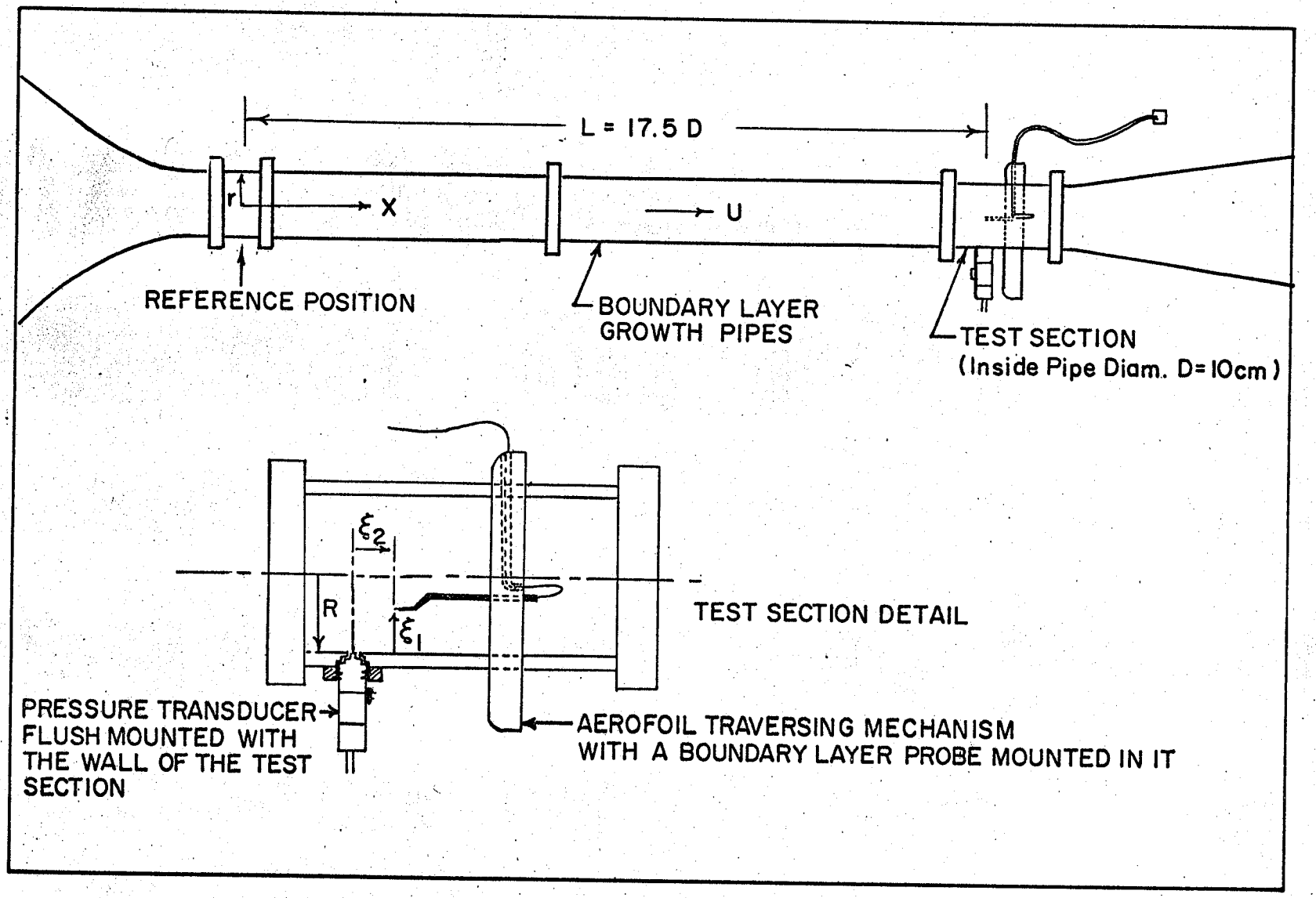

FIGURE 3.1 SCHEMATIC DIAGRAM SHOWING THE ORIENTATION OF THE TEST SECTION IN THE WIND TUNNEL.

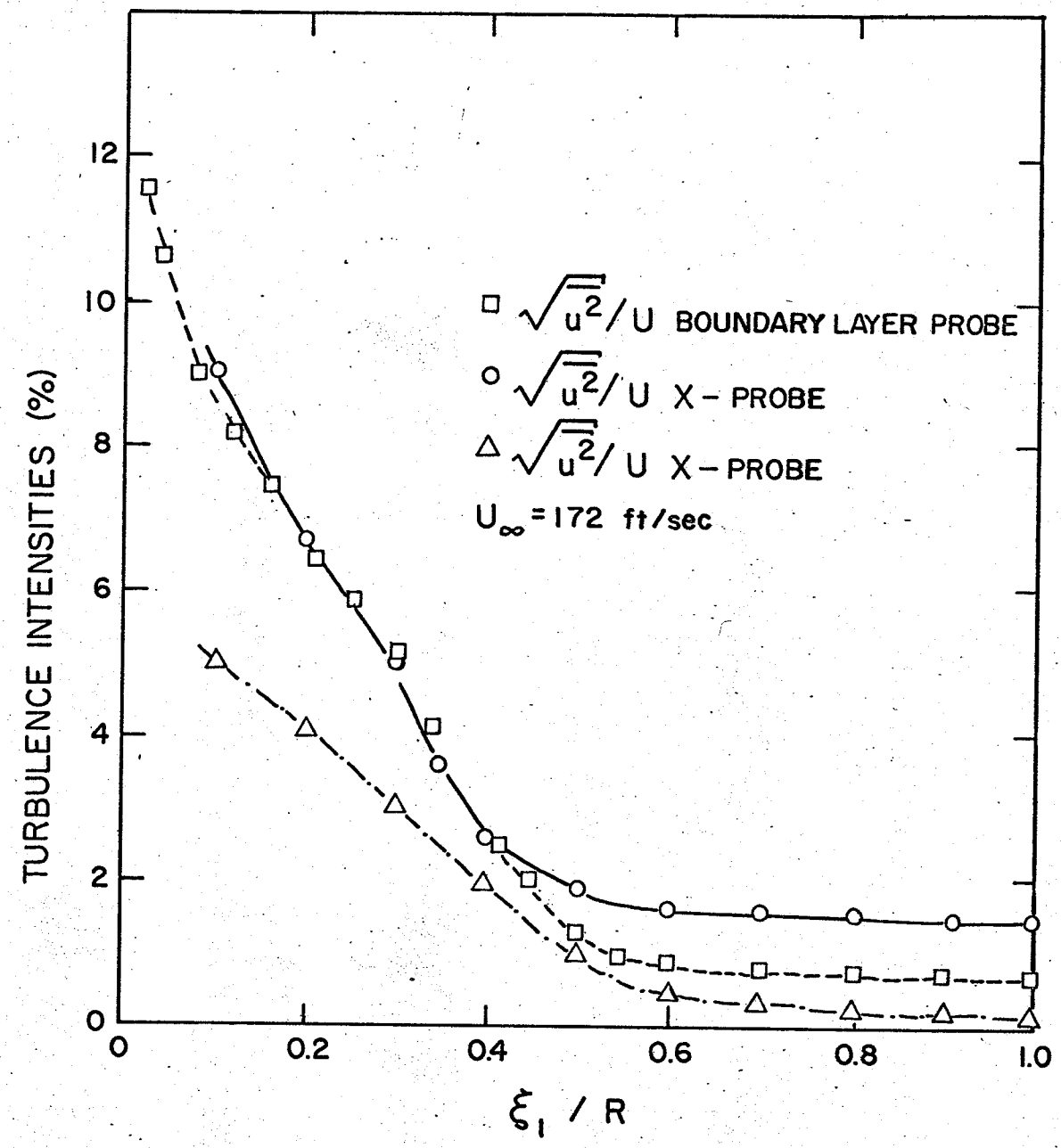

FIGURE 3.2 COMPARISON OF INTENSITY PROFILES OBTAINED USING A BOUNDARY LAYER PROBE AND AN X-PROBE, WITH L/D = 17.5 AND ξ_2 = 0.

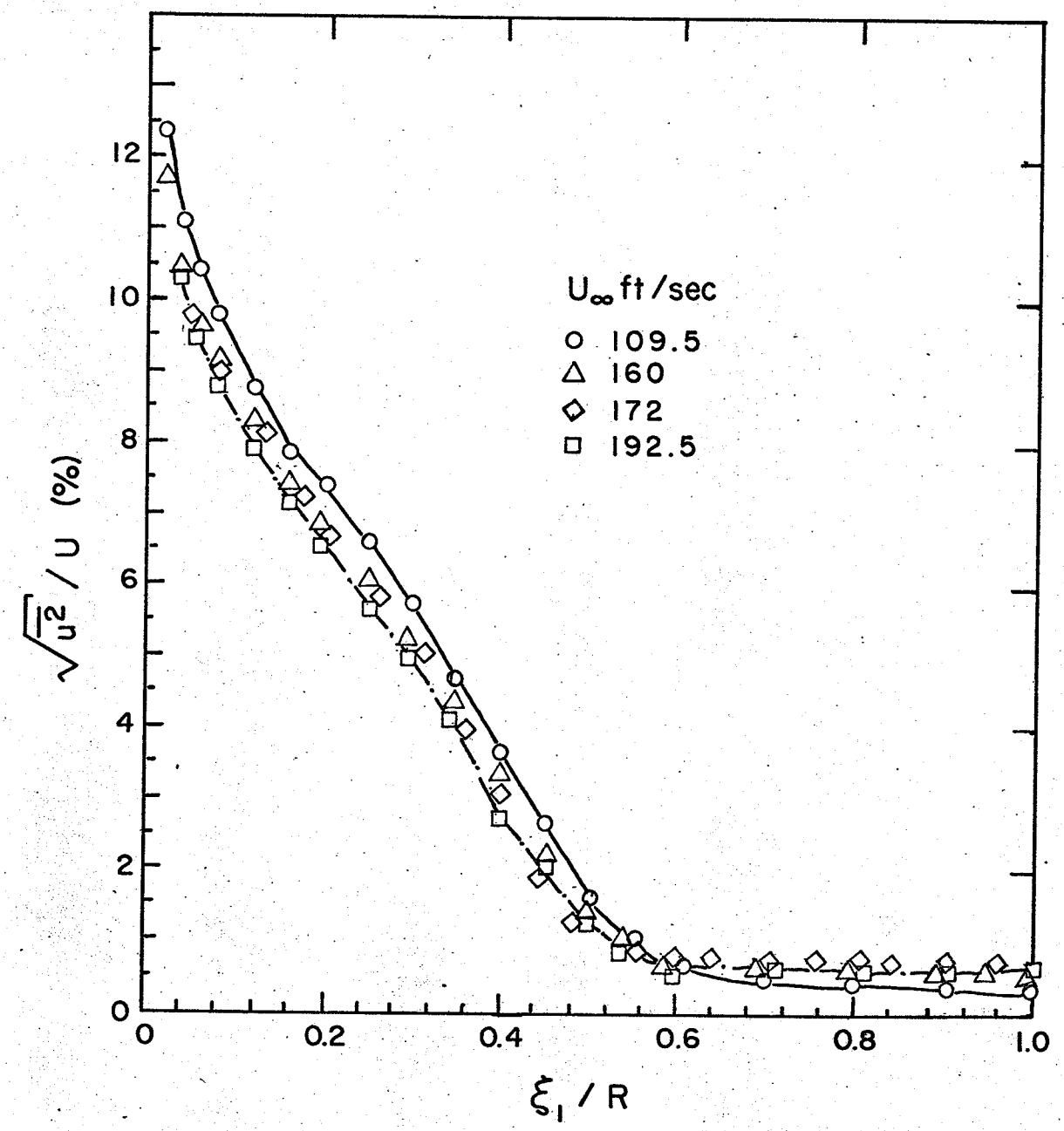

FIGURE 3.3. TURBULENCE INTENSITY MEASUREMENTS OBTAINED ALONG A RADIAL TRAVERSE, $\xi_2/R = 0.05$.

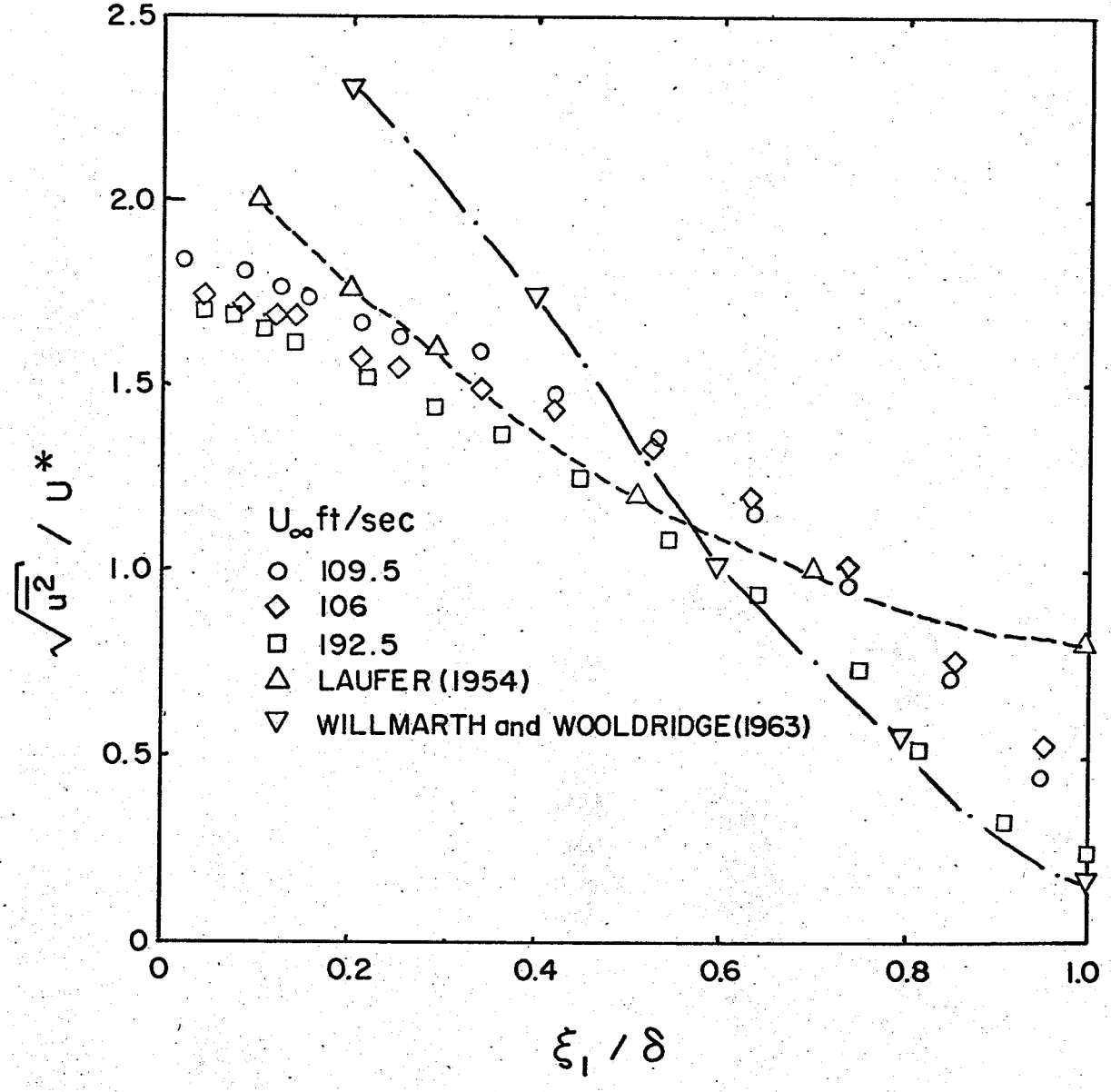

FIGURE 3.4 COMPARISON OF TURBULENCE INTENSITY MEASUREMENTS TO THOSE OF LAUFER (1954) AND WILLMARTH AND WOOLDRIDGE (1963).

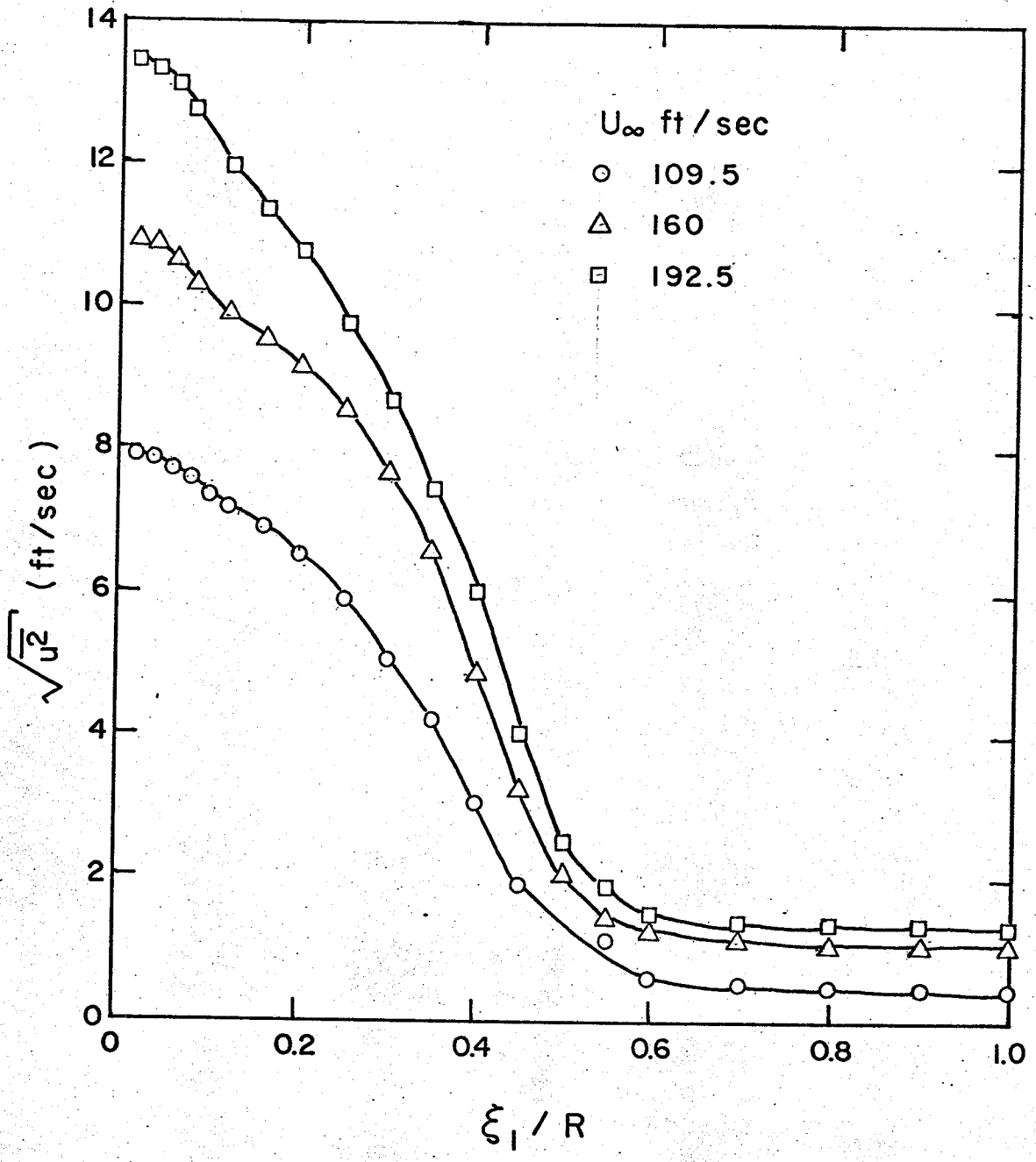

FIGURE 3.5 DISTRIBUTION OF THE r.m.s. VALUES FOR THE VELOCITY FLUCTUATIONS OBTAINED ALONG THE RADIAL TRAVERSE $\xi_2/R = 0$.

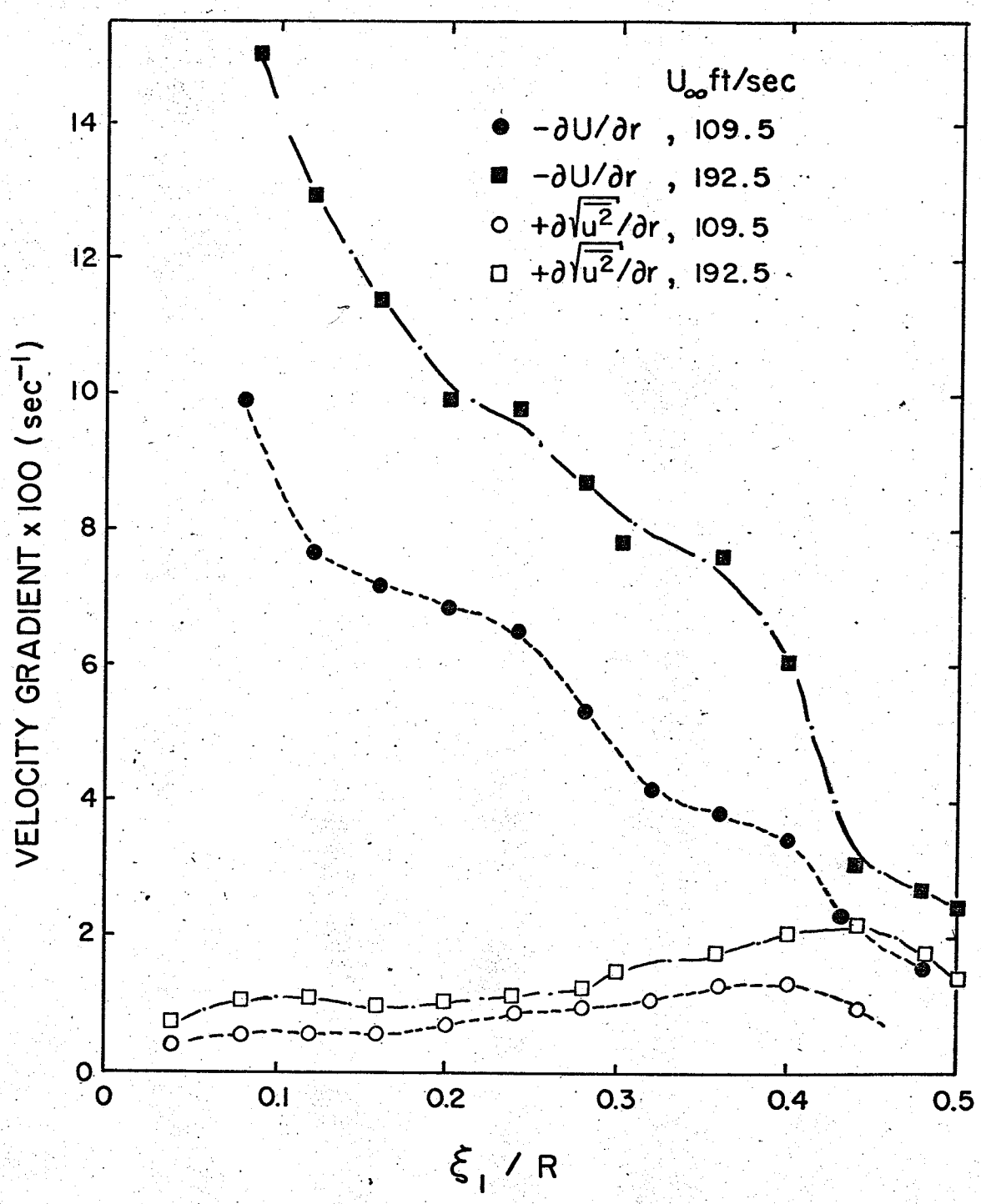

FIGURE 3.6 COMPARISON OF THE MAGNITUDES OF THE VELOCITY GRADIENTS IN THE RADIAL DIRECTION OF THE MEAN AND FLUCTUATING VELOCITY COMPONENTS.

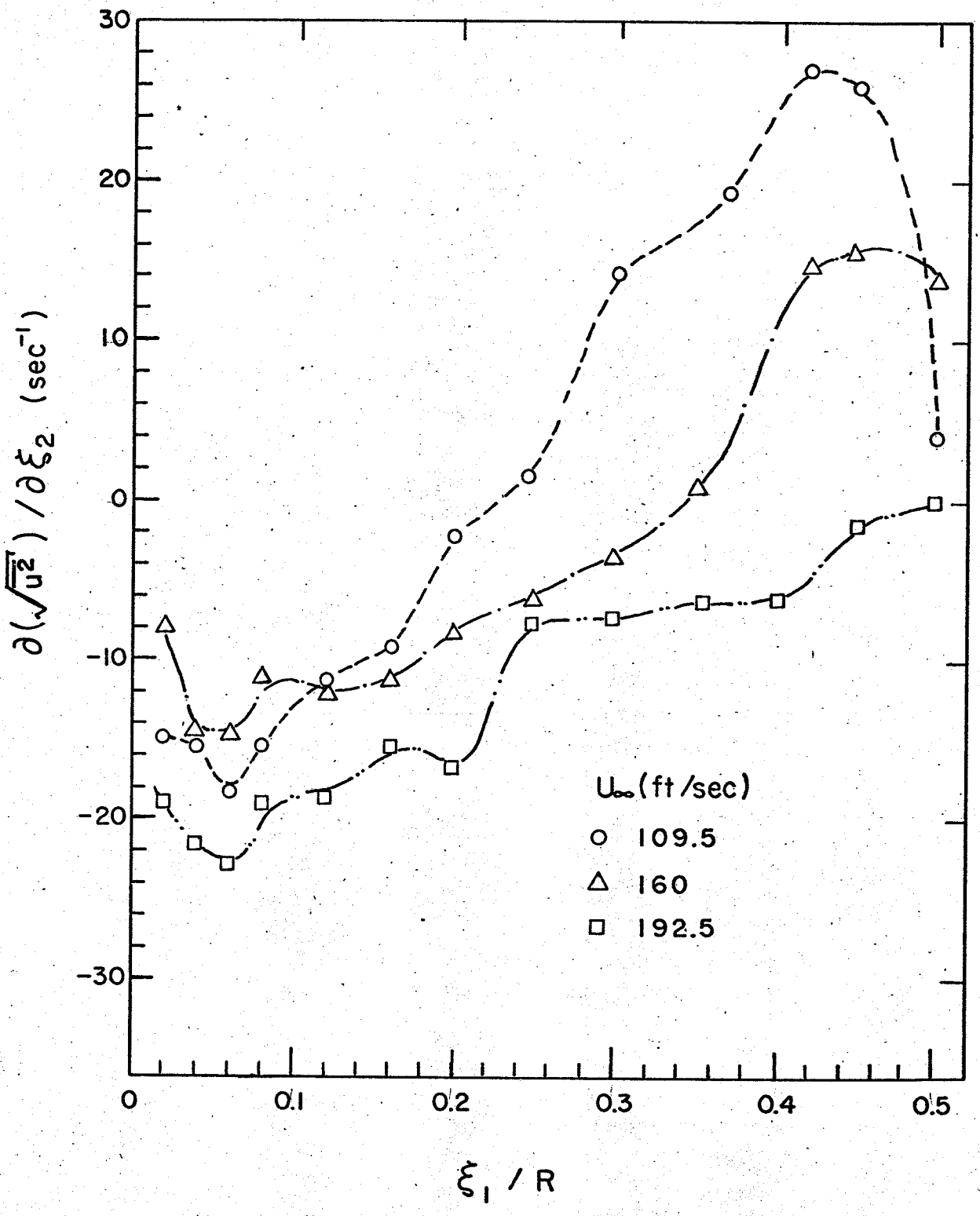

FIGURE 3.7 VELOCITY GRADIENTS IN THE AXIAL DIRECTION OF THE FLUCTUATING AXIAL VELOCITY COMPONENT.

CHAPTER 4

STATISTICAL PROPERTIES OF TURBULENCE MEASUREMENTS

4.1 Introduction to Correlation Analysis.

Correlation functions are extremely useful in the analysis of random phenomena and the complex wave forms which are produced. The correlation function technique seems to have been introduced to random process theory around 1920 by Sir G.I. Taylor and has since been used extensively in the field of turbulence research. This widespread use has been partly due to the fact that the correlation functions are usually concerned with readily measurable quantities such as velocity and pressure fluctuations.

The correlation techniques used for describing the interrelationships among various electrical signals are important in two broad areas of application:

(1) Auto correlation - which can be used to detect an unknown repetitive signal in the presence of noise.

(2) Cross correlation - used when it is desired to compare two wave forms to determine the degree of conformity between them.

In the following subsections the mathematical expressions for these correlation functions are given; curves showing the distribution of the related correlation coefficients between the fluctuating wall pressure and the fluctuating axial component of velocity are also presented.

The cross correlations between the wall pressure fluctuations and turbulent velocity fluctuations at various positions in the flow were measured in an attempt to determine how different regions of the developing pipe flow contribute to the wall pressure field.

4.1.1 Auto Correlation.

The auto correlation technique involves the comparison of a wave form against a delayed version of itself. The mathematical expression for this operation is commonly written as:

$$Q_{AA}(\tau) = \lim_{T\to\infty} \frac{1}{2T} \int_{-T}^{T} f_A(t)\, f_A(t - \tau)dt, \qquad 4.1$$

where:

$Q_{AA}(\tau)$ is the auto correlation function.

τ is a time-delay parameter.

$f_A(t)$ is a time function of a stationary physical process such as the fluctuating pressure or velocity.

T is the averaging time.

It can be seen from Equation 4.1 that each point on the complete correlation function, $Q_{AA}(\tau)$, must be determined by the multiplication of a signal $f_A(t)$, by a version of itself that has been delayed by some particular value of τ, and then integrated over a period T. When this multiplication and integration is performed for many values of τ, the complete correlation function can be obtained.

The auto correlation function permits extraction of information concerning signals that are obscured in noise, but the inherent nature of the operation rejects phase information concerning $f_A(t)$, and produces an output wave form that may not be an actual reproduction of the input wave form. However, it will always have the same periodicity as the input signal. Consequently, using this technique a frequency analysis of the input signal may be performed.

4.1.2 Cross Correlation.

The use of the cross correlation permits the comparison of two input signals from different, but coherent (not masked by noise), sources. The resulting correlation function contains information regarding the frequencies that are common to both wave forms, and the phase difference between them. The function may be expressed mathematically as:

$$Q_{AB}(\tau) = \lim_{T\to\infty} \frac{1}{2T} \int_{-T}^{T} f_B(t)\, f_A(t - \tau)dt, \qquad 4.2$$

where:

$Q_{AB}(t)$ is the cross correlation function.

τ is the time-delay parameter

$f_A(t)$ and $f_B(t)$ are two different time functions that arise from the physical process being investigated.

Equation 4.2 is very similar to that for the auto correlation, the difference being that the first input signal is multiplied by a delayed version of a second input signal, rather than by a time-delayed version of itself.

The cross correlation is extremely useful in describing the degree of conformity between two different signals as a function of their mutual delay. Because of its ability to measure,quantatively, the degree of "likeness" of two signals, the use of this correlation can provide a much deeper insight into the phenomenon being investigated than a separate analysis of the properties of either signal alone would reveal.

4.1.3 Experimental Technique for Data Collection and Analysis.

Rather than using the particular correlation functions in the form given in Equations 4.1 and 4.2, the two functions may be represented in terms of the following general covariance between two time dependent signals.

This general form is:

$$Q_{pq}\ (\xi_2,\ \xi_1;\ \tau)\ =\ \overline{p(x_1,\ R;t)\ q\ (x_1 + \xi_2,\ R - \xi_1;\ t + \tau)}, \qquad 4.3$$

where:

the over score denotes a statistical mean value.

τ, and t are the time parameters.

x_1, R, ξ_1 and ξ_2 are the position vectors shown in Figure 3.1.

p and q are time functions of a stationary process.

By normalizing Equation 4.3 with the individual root-mean-square values of the separate signals, the Correlation Coefficient $R_{pq}\ (\xi_2,\xi_1;\tau)$, may be represented as follows:

$$R_{pq}\ (\xi_2,\xi_1;\tau)\ =\ \frac{\overline{p(x_1,\ R;t)\ q\ (x_1 + \xi_2,\ R - \xi_1;\ t + \tau)}}{\sqrt{\overline{p^2(x_1,\ R;t)}}\sqrt{\overline{q^2\ (x_1 + \xi_2,\ R - \xi_1;\ t + \tau)}}} \qquad 4.4$$

This coefficient exhibits much the same properties as the correlation function and reveals the same information, however, the normalizing procedure simplifies the work involved in using the statistical correlation techniques. If for example, two fluctuating velocity signals were being correlated with one another, an absolute calibration of the velocity with respect to the output voltage would not be necessary. The reason being that the calibration constant, relating the electrical output to the velocity, would be cancelled out by the normalizing procedure. This assumption only holds for the condition where the calibration does not shift drastically with time, and fortunately, this is the case for the hot-wire anemometers and the pressure transducer. However, it should be noted that the dynamic response of the sensing elements must still be known, and taken into account. Another feature of this normalizing procedure is that the correlation coefficient formed, has values in the range of ±1.0, with the sign depending

on the phase shift between the two signals being correlated.

From the generalized equation for the correlation coefficient, Equation 4.4, the auto correlation coefficient, $R_{pp}\ (o,o;\tau)$ may be represented as:

$$R_{pp}\ (o,o;\tau) = \frac{\overline{p(x_1, R;t)\ p\ (x_1, R;\ t + \tau)}}{\overline{p^2}\ (x_1, R;t)} \qquad 4.5$$

where:

$p(x_1, R;t)$ is a time function of a stationary process such as pressure or velocity fluctuations.

$\overline{p^2}(x_1, R;t)$ is the mean squared value of this time function.

Figure 4.1 shows a block diagram of the electrical analogue method used to determine the correlation coefficients, and in this figure the two signals $p(x_1, R;t)$ and $u(x_1 + \xi_2, R - \xi_1;\ t)$ would be made the same in order to form the auto correlation. The time delay in this circuit was supplied by the movable playback heads of the F.M. tape recorder. However, several limitations were imposed by the use of this time delay unit. In order to ensure a high enough upper frequency limit (20 KHz) it was necessary to operate the tape recorder at a speed of 60 inches per second, and at this speed, a time delay of only ±5 m sec could be obtained. By operating the tape recorder at 6 inches per second a time delay of ±50 m sec could have been introduced, however, the upper frequency limit was then reduced to 2 KHz.

With the transducer mounted in the wall of the test section, as shown in Figures 1.2(b) and 3.1, the auto correlation coefficients of the wall pressure fluctuations were obtained using time delays in the range of $-5 \leq \tau \leq 55$ m sec. The resulting curve is shown in Figure 4.2, however, nothing conclusive could be drawn from this curve due to the limited time delay that could be introduced. A better time-delay unit, capable of giving larger time shifts, could be obtained by the use of an analogue time-delay line,

and using this delay line, a more useful correlation curve could have been obtained.

It will be shown in Section 4.2 that the auto correlation function and the energy spectrum function are a Fourier transform pair. Thus, no more information of a random process can be gained by auto correlation function techniques than what is obtained from direct spectral density measurements. Because the auto correlation methods employed were not adequate to obtain information on the periodicity of the input wave form, a more detailed study of the individual signals from the pressure transducer and hot-wire probes was made with the use of direct power spectral density measurements. These results are presented and discussed in Section 4.2.

The cross correlation coefficient between the fluctuating wall pressures and the fluctuating component of the axial velocity can be obtained directly from the general form of Equation 4.4. In this expression the time function $q(x_1 + \xi_2, R - \xi_1; t + \tau)$ would be replaced by $u(x_1 + \xi_2, R - \xi_1; t + \tau)$ and the new time functions, $p(x_1, R;t)$ and $u(x_1, R;t)$, would represent the fluctuating pressure and velocity signals respectively. The Disa Random Signal Correlator was used to determine the cross correlation coefficient, and the block diagram of the analogue circuit used is given in Figure 4.1.

Initially, it was the intention of this author to measure both the R_{pu} and R_{pv} cross correlation coefficients relating the wall pressure fluctuations to the fluctuating components of the velocity in both the axial and radial directions. The X-probe, which would give the u and v components of the fluctuating velocity, could approach the wall of the test section, in which the pressure transducer was flush mounted, to a distance of only $\xi_1 = 0.08$ R. The region of interest in the boundary layer extended much closer to the wall than this, and thus

it was decided to use the boundary layer probe which could approach the wall to a distance of $\xi_1 = 0.02R$. The boundary layer probe, however, could only be used to measure the fluctuating velocity in the axial direction and consequently only the R_{pu} correlation coefficients were determined.

The first measurements of this cross correlation coefficient were obtained on a radial traverse of the plane in which the center of the transducer was located ($\xi_2 = 0$). To investigate the effects of the unsteady flow field created by the hot-wire probe on the pressure transducer, the probe was located as close to the transducer as possible, and measurements of the root-mean-square wall pressure and energy spectra of the pressure fluctuations were made. With the hot-wire probe located directly above the transducer ($\xi_1/R = .02$) and downstream ($\xi_2 > 0$) of the transducer, there was no significant change in the root-mean-square wall pressure or the spectral density measurements compared to those taken without the presence of the probe. However, with the hot-wire probe located upstream ($\xi_2 < 0$) of the transducer, a significant change in r.m.s. value of the pressure fluctuation was observed and consequently, only radial traverses for $\xi_2 \geq 0$ were used for correlation purposes. The electrical signals from the hot-wire probe and the pressure transducer were filtered before the correlations were measured, using the same frequency band as for the turbulence intensity measurements, 20 Hz < f < 50 KHz. The upper frequency limit was important for the pressure transducer output, as a result of its mechanical resonant frequency being 58 KHz. For the correlation measurements it was found that an averaging time of 15 seconds was sufficient in order to obtain a true record of the results.

The results for the cross correlation measurements (with a zero time delay) obtained along three radial traverses for different free stream flow conditions, are presented in Figures 4.3(a), (b) and (c). The information

near the wall of the test section could not be displayed adequately in these figures, and consequently Figures 4.5 (a), (b) and (c) were presented with expanded scales along the axes.

4.1.4 Discussion of Cross Correlation Measurements.

The cross correlation coefficients between the wall pressure fluctuations and the fluctuating component of the axial velocity, measured in this investigation, are presented in Figures 4.3(a), (b) and (c).

From these figures it can be seen that the cross correlation coefficients R_{pu} (ξ_2, ξ_1; 0) all exhibit the same general trends as the separation vectors are changed. There appear to be three separate zones in the flow, each showing distinct characteristic properties, and these regions may be described as follows:

(a) The free stream flow region ($\xi_1/R > .58$) where the turbulence intensities are of the order of 1%.

(b) The intermittent zone ($.48 < \xi_1/R \leq .58$) where the flow is turbulent only part of the time.

(c) The turbulent boundary layer zone ($0 \leq \xi_1/R \lesssim .48$) where the turbulence intensities show a sharp increase up to 10%.

In the following discussion, the free stream flow region and the boundary layer region will be discussed in detail, however, the intermittent zone will not be discussed. The reason for this is that the parameter necessary for a meaningful discussion of the intermittent zone, the intermittency factor, γ, was not measured. For future studies in this zone, this parameter should be measured by the technique described by Hummel (1970).

The general trend exhibited by these correlation curves for a given speed, showed the values of the cross correlation coefficients remaining constant in the region $\xi_1/R > .58$; decreasing rapidly in the intermittent

zone; and decreasing gradually through zero to a low negative value in the boundary layer region. Consequently it is natural to discuss each of the regions separately.

In the free stream flow region ($\xi_1/R > .58$) the cross correlation coefficients remain constant for a given center line velocity, and it was previously shown in Section 3.3 that the level of the turbulence intensity in this region also remained constant. The fact that both the correlation coefficient R_{pu} $(\xi_2,\xi_1;0)$ and the intensity levels were constant would suggest that the pressure transducer receives comparable contributions, from all parts of this region, to the total measured fluctuating pressure. Considering the Navier-Stokes equations for three-dimensional flow and neglecting the body forces per unit mass, the following vector equation results:

$$-(1/\rho)\ \text{grad}\ p = d\bar{v}/dt, \qquad 4.6$$

where:

p is the pressure.

ρ is the fluid density.

$\bar{v}$ is the velocity vector.

From this equation it can be seen that a fluctuating velocity vector causes a pressure field to be generated and this field must be moving away from the source of generation at the speed of sound. Thus, the pressure field generated in this region must be propagated through this region and then through the boundary layer to the wall, where it is measured with the pressure transducer. Consequently, the fluctuating wall pressures measured were a result of both the turbulent action in the boundary layer and the fluctuating velocity in the free stream.

Figure 4.4 shows that the correlation coefficient in this region of the flow is dependent on the center line velocity whereas there does not

appear to be a very strong dependency upon the separation distance ξ_2. The latter observation would suggest the presence of large scale eddies or pulsations in the free stream flow region because one would expect a sharp decrease in correlation for increased values of ξ_2 if the velocity fluctuations were due to small scale eddies. From this figure, it can be seen that the maximum correlation between the fluctuating wall pressure and fluctuating axial velocity component occurred when the center line velocity was 172 feet per second. This is probably due to the fact that the intensity levels of the turbulence (see Section 3.3) in this region of the flow also reached a maximum at this speed.

In order to formulate some ideas of the nature of the velocity fluctuations in the free stream region, it was necessary to study them in the frequency domain because the turbulence intensities measured in the time domain, did not show the complete picture of what was happening. In Section 4.2 the energy spectral density measurements of the fluctuating axial velocity component in the free stream region are presented, and discussed in relation to the turbulence intensities.

The cross correlation coefficients which were measured with the hot-wire probe in the boundary layer region are presented in Figures 4.5(a), (b) and (c). These curves exhibit the same velocity dependency as was shown in the free stream flow region. However, in the boundary layer region a much stronger dependency upon the separation vector ξ_2 exists. In the outer region of the boundary layer the correlation coefficients showed a gradual decrease in magnitude as the ξ_1/R values decreased. This, however, does not imply that the wall pressure receives comparable contributions from all parts of this region since the intensity of the velocity fluctuation falls off rapidly as the distance from the wall, ξ_1/R increases. In the inner part of the boundary layer, the correlations were increasing in

magnitude towards the wall because of the relatively high turbulence intensities in this region. However, the maximum correlations near the wall decreased rapidly as the separation vector ξ_2 was increased. This decrease in correlation tends to suggest the presence of small scale, pressure producing eddies, in the boundary layer.

An interesting feature exhibited by these correlation curves was that the correlation coefficient changed from a positive to a negative correlation, with the point of reversal being shifted closer to the wall as the separation vector ξ_2 was increased. This reversal in sign for the correlation coefficient has been reported for a turbulent boundary layer of a flat plate by Kawamura (1960) and Bradshaw (1967). The latter presented the argument that the correlation passes through zero in the region where the turbulence intensity is high, because the pressure fluctuation is more nearly in phase with $\delta u/\delta x$ than u in this region. To validate this argument, one should obtain the space derivative of the fluctuating axial component of the velocity and correlate it with the wall pressure fluctuations. This was not done in this investigation but it should be included in future work.

When the boundary layer probe was located on the $\xi_2 = 0$ traverse, the maximum correlations between the fluctuating axial velocity and fluctuating wall pressures near the wall ($\xi_1/R = .02$) were of a magnitude between .06 and .10, which are comparable to the values given by Bradshaw (1967), Kawamura (1960) and Willmarth and Wooldridge (1962).

From these cross correlation measurements it can be seen that the wall pressure fluctuations in developing pipe flow are a result of the interaction of two components.

(a) The fluctuating axial velocity in the free stream region generating a fluctuating pressure which is transmitted through the boundary layer.

(b) The small scale eddies which are in the turbulent boundary layer.

4.2 Introduction to Spectral Analysis.

Another powerful method for describing a fluctuating field is to analyze it into Fourier components by adopting the spectral approach. It was previously mentioned in Chapter 3 that the Spectral theory and the Correlation theory are mathematically related by means of a simple Fourier transformation. Although these two methods of description are related, they put different emphasis on different aspects of the flow phenomena and the spectral theory often gives a clearer description of the basic mechanism of turbulence. The power spectral density presentation of turbulence information permits one to consider how the turbulent energy is distributed among the various frequencies or sizes of the turbulent eddies.

Spectral analysis has long been used in the field of communications with Taylor (1938) being the first to introduce it into the study of turbulence by presenting an energy spectrum of the velocity fluctuations behind a grid located in a wind tunnel. From this time, the power spectral density curves for the velocity fluctuations in a turbulent boundary layer have been presented by investigators such as Laufer (1954), Willmarth and Wooldridge (1963), and, Tu and Willmarth (1966). The fluctuating velocities have been studied in great detail, largely because of the early development of the hot-wire anemometer and it has been only in the last fifteen years that work dealing with the wall pressure fluctuations has been undertaken. With the recent development of miniature pressure transducers capable of detecting small pressure fluctuations, investigators such as Willmarth and Wooldridge (1962,1963), Bull (1963), Kawamura (1960), and Schloemer (1967) have presented power spectral density curves of the wall pressure fluctuations beneath a turbulent boundary layer.

In the following sections a mathematical description of the power spectrum, and power spectral density curves of the measured wall pressure fluctuations and the fluctuating axial velocity components, found in a developing pipe flow, are presented and discussed.

4.2.1 Mathematical Description

The power spectral density function of a fluctuating signal is related to the auto correlation function of the signal by the Fourier cosine transformation as shown below:

$$\Phi_{pp}(\omega) = \frac{1}{2\pi}\int_{-\infty}^{\infty} R_{pp}\,(o,o;\tau)\cos\,\omega\tau\,d\tau, \qquad 4.7$$

where:

$\Phi_{pp}(\omega)$ is a spectral density function of a fluctuating signal, p.

$R_{pp}(o,o;\tau)$ is the auto correlation function of the fluctuating signal.

τ is a time parameter.

As suggested by Equation 4.7, in order to obtain the power density spectrum from the auto correlation function it is necessary to multiply a cosine function at each frequency by the correlation function, and then integrate with respect to time. When this has been done over the frequency range of interest, the total power spectrum is obtained. Thus, by using this technique, the correlation function $R_{pp}(o,o;\tau)$ which exists in the time domain is transformed into a power spectral density function $\Phi_{pp}(\omega)$ which exists in the frequency domain.

This transformation has been used by several investigators to present information in the frequency domain, from data which was obtained in the time domain using correlation techniques. However, experimental

measurements are never free from inaccuracies, and because the energy spectral densities may be measured directly using a power spectrum analyzer, it is better to consider the mathematical relation between the spectrum and correlation function merely as a convenient means of checking the experimental determination of both.

4.2.2 Experimental Techniques for Data Collection and Analysis.

The power spectra presented in this section were measured using the Hewlett-Packard Model 3590-A wave analyzer, with a constant bandwidth of 10 Hz being employed over the frequency range of 10 Hz to 60 KHz. The narrow bandwidth used required the accumulation of data for several minutes at each center frequency so that a reasonably good average of the signal could be obtained. When preliminary tests were conducted, it was observed that the damping of the internal r.m.s. meter of the wave analyzer was insufficient, and consequently, the meter damping was increased from approximately 1 second to 10 seconds with very satisfactory results.

The pressure fluctuations were measured at different free stream velocities with the pressure transducer located in the test section, as shown in Figure 3.1. Figure 4.7 shows the spectral density measurements of the fluctuating wall pressure, with the ordinate of the spectral density curves being a decibel scale which is referenced to $1(\mu \text{ bar})^2/\text{Hz}$. In order to obtain the ordinate scale of the power spectral density curves in the appropriate units of squared pressure, the r.m.s. values of the signal at each central frequency were recorded using the internal r.m.s. meter of the wave analyzer. After the whole frequency range under consideration had been scanned, the total r.m.s. value of the signal was measured in the frequency band from 10 Hz $\leq f \leq$ 60 KHz using the Disa r.m.s. meter. This value will be referred to as the bandwidth unlimited r.m.s. value of the signal, and

because this measurement was very important an average value of several readings was obtained. Using the r.m.s. values from the wave analyzer, a power spectral density curve was plotted on linear graph paper with the ordinate being any arbitrary scale, selected for the best data representation.

To determine the ordinate scale in the appropriate pressure units, it was necessary to integrate the density curve and equate the area under the curve to the bandwidth unlimited r.m.s. value. Then, by using the calibration curve for the pressure transducer it was a simple matter to convert the electrical units into units of pressure.

The theory behind equating the area under the power spectral density curve (plotted on a linear scale) to the root-mean-square value of the bandwidth unlimited signal can be explained as follows:

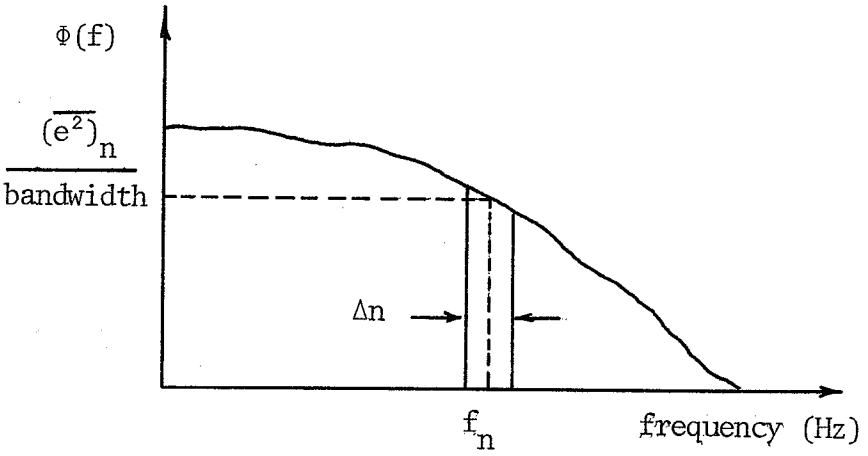

FIGURE 4.6 TYPICAL SHAPE OF A SPECTRAL DENSITY CURVE.

If one considers a bandwidth of (Δn) Hz with a central frequency of f_n, the corresponding output, per bandwidth, would be $[\Phi(f)]_n$ which would be measured in electrical units as $(\overline{e^2})_n$.

If the whole frequency range was considered, the total electrical output would be :

$$\left(\sum_{i=1}^{n} (\overline{e_i^2})^2 \right)^{\frac{1}{2}} , \qquad 4.8$$

where the summation is taken over the whole range of frequencies under consideration. These electrical signals add in quadrature because the quantity which is measured by the wave analyzer is the power contained in the signal. Figure 4.6 illustrates that strips which are $\overline{e^2}_n$/Hz high and (dn) Hz wide are being added up, and when the whole frequency range is scanned, the total area under the power spectral density curve is obtained and this must be equal to the bandwidth unlimited r.m.s. signal.

The power spectral density curves of the fluctuating axial velocity component were measured along the radial traverse, $\xi_2 = 0$, for various free stream velocities. These curves are presented using a decibel scale based on an arbitrary reference and thus only a qualitative discussion of the results was possible. When significant peaks were observed in the power spectra of the fluctuating axial component of velocity in the free stream region, a furthur investigation of the fluctuating velocity was undertaken with the traversing mechanism being re-located at the exit of the contraction cone. At this position, energy spectra of the fluctuating axial velocity component were obtained.

4.2.3 Discussion of Experimental Results.

The power spectral density measurements of both the fluctuating wall pressure and fluctuating axial component of velocity are presented in this section. The energy spectra of the pressure fluctuations will be discussed first, followed by comments on the spectra of the velocity fluctuations.

The power spectral density curves of the wall pressure fluctuations obtained for the free stream velocities of 109.5, 160, and 192.5 feet per second are shown in Figure 4.7 with the vertical scale being represented in decibels, referenced to $1(\mu \text{ bar})^2$/Hz. Included in this figure is the power

spectral density curve for the ambient noise of the system, obtained with the transducer mounted in the test section while the tunnel was not in operation. Thus, the output would be representative of the ambient noise in the tunnel plus the electronic noise in the instrumentation. It can be seen from Figure 4.7 that the ambient noise level is approximately 20 Db below the spectrum level for the highest velocity and about 10 Db below the level for the lowest velocity under consideration in the frequency range from 10 Hz to 10,000 Hz. This signal to noise level can be considered to be acceptable (Schloemer (1967)). Attempts were made to obtain an estimation of the contributions which the fan noise made to the total pressure signal, however, the sound measurements described in Section 1.4.3 were inconclusive.

In Figure 4.7 several prominant peaks can be seen in the low frequency range of the spectra, and these will be shown presently to be directly related to the velocity fluctuations occurring in the free stream region. Also it can be seen from the peak which occurred at a frequency of 58 KHz that the resonant frequency of the pressure transducer assembly had been excited, and consequently, no information beyond 50 KHz could be extracted to aid in the description of the pressure field.

Figure 4.8 shows a comparison of the power spectral density curve of the wall pressure fluctuations obtained for a free stream velocity of 192.5 feet per second to the spectra obtained by Bull (1963), Willmarth (1965), and Schloemer (1967) for a flat plate and by Bakewell (1962)for fully developed pipe flow. The comparison is shown in the form of nondimensional power spectral densities which are plotted as functions of a nondimensional frequency. This can be represented as:

$$\Phi(f)/\rho^2 U_\infty{}^3 \delta^* = F(f\ \delta^*/U_\infty), \qquad 4.9$$

where:

$\Phi(f)$ is the power spectral density; that is, the mean square pressure per unit bandwidth.

U_∞ is the free stream velocity.

ρ is the fluid density.

δ^* is the displacement thickness.

f is the center frequency.

This method of presenting the spectral data provided a useful scaling for the power spectral density in terms of the frequency, displacement thickness and flow velocity.

It should be noted that the curves in Figure 4.8 have not been corrected for the attenuation of the pressure fluctuations caused by the finite size of the sensing elements, however, the corrections which should be applied (described in Section 4.3) are all of the same order of magnitude. From the comparison it can be seen that the experimental results are slightly higher than the results of the other investigators and this may be due to the fact that the transducer was receiving contributions from the free stream region as well as from the boundary layer.

Figures 4.9(a), (b) and (c) show the energy spectra of the fluctuating axial velocity components which were measured along the radial traverse, $\xi_2 = 0$, for three different free stream velocities. The ordinate scale of these figures is represented in decibels, based on an arbitrary reference, and consequently only the energy contained by the fluctuating velocities measured at different ξ_1/R values on the same radial traverse, and for a given speed, may be compared with one another. Although the arbitrary reference of the decibel scale imposes a few limitations with regards to a quantitative analysis of how the energy distribution changes with increasing flow rates, it is possible to formulate a qualitative idea of the flow structure.

Crudely speaking, one can say that the seven energy spectra presented on each figure show the distribution of the energy among the various eddy sizes in the three regions of the flow described in Section 3.3. The lower three curves (ξ_1/R = 1, .8 and .6) show the distribution of the energy contained by the eddies in the free stream region; the middle curve, ξ_1/R = .4 shows the spectrum obtained in a region near the outer edge of the turbulent boundary layer; the upper three curves (ξ_1/R = .2, .1 and .02) show how the turbulent energy is distributed in the middle and inner regions of the turbulent boundary layer. It is convenient to discuss these regions separately, in a manner similar to the previous chapter.

In the free stream region of the flow, the curves obtained at ξ_1/R = 1 and .8 show similar characteristics for the mean free stream velocities which were considered. The spectra showed a relatively constant energy level up to about 200 Hz with a sharp decrease in energy occurring the frequency range from 200 Hz to 1000 Hz. Beyond the 1000 Hz frequency region, the energy level remained more or less constant until a frequency of 5500 Hz was reached. In the frequency range near 6000 Hz a sharp peak is prominent and beyond this frequency, the energy seems to be increasing slightly with several distinct peaks being present in this region of the spectra for the free stream velocities of 160 and 192.5 feet per second. It can be observed that the energy level of the spectra obtained at ξ_1/R = .6 remained constant up to about 700 Hz and as the frequency was increased, the energy level did not decrease as rapidly as in the spectra for ξ_1/R = 1 and .8. This would suggest that as the boundary layer was approached, a redistribution of energy took place among the eddy sizes in the range related to the frequencies from 700 to 5000 Hz.

The large amounts of energy contained in the immediate frequency range of 70 Hz indicated the presence of large scale velocity fluctuations in the free stream flow. These large scale fluctuations explain why the power spectra of the fluctuating wall pressure also have a prominent peak at 70 Hz, because it has been previously shown that the pressure measurements are strongly correlated with the fluctuating velocity in the free stream region. Figure 4.10 shows the energy spectra of the fluctuating component of the axial velocity in the free stream region, obtained at the exit of the contraction cone with $\xi_1/R = 1$ and $x = 0$. These spectra show prominent peaks occurring in the low frequency region at 70, 135 and 300 Hz, and because the peaks at 135 and 300 Hz were not observed downstream in the test section (see Figures 4.9(a), (b), and (c)) it would appear that a certain amount of viscous damping had occurred in the free stream region. The power spectra of the fluctuating wall pressures, measured in the test section as shown in Figure 3.1, showed prominent peaks at 70, 135 and 300 Hz, and consequently it is possible that the pressure transducer also measured the pressure waves which were generated by the fluctuating velocities upstream of the test section and were propagated through the flow region at the speed of sound.

Also shown by the spectra given in Figures 4.9(a), (b) and (c) was the presence of high energy-containing, high frequency (6000 Hz) eddies. The pressure field generated by these small scale eddies was only slightly evident in the power spectral density measurements of the wall pressure fluctuations. This may be due to the attenuation of the pressure waves resulting from the finite size of the pressure transducer. Section 4.3 will deal with this in more detail.

In the free stream region it can be seen that the prominent peaks in the spectra do not shift as the flow rate is changed and this

would indicate that the velocity fluctuations are not directly related to the centrifugal action of the fan. The low frequency velocity fluctuations which have been detected in the free stream region could be a result of a low frequency pulsation being introduced into the flow stream by a vibrating component of the tunnel such as one of the screen sections. The internal surface of the contraction cone was found to be fairly rough, as compared to the surface finish of the boundary layer growth pipes, and it is possible that small scale eddies were generated at the wall of the contraction cone and were then swept downstream into the test section. This could account for the high frequency velocity fluctuations which were detected in the free stream region.

Thus, it appears that the velocity fluctuations which were present in the free stream flow region were the result of small scale eddies being superimposed on a low frequency, pulsating flow field.

The spectral density measurements obtained at $\xi_1/R = .4$ indicate a fairly large increase in total energy contained by the flow in the outer region of the boundary layer as compared to that in the free stream region. All the spectra in the boundary layer region show that the total energy contained by the flow increased as the wall was approached. In this region it was noticed that for a specified decrease in ξ_1/R values, the energy increase in the outer region of the boundary layer was greater than the increase which occurred in the inner region. The reason for this phenomenon is not fully understood, and in order to determine how it is related to the fluctuating pressure and velocity fields in the turbulent boundary layer it would be necessary to study the spectra in a quantitative manner.

4.3 Spatial Resolution of the Sensing Element of the Pressure Transducer.

4.3.1 Introduction.

The finite size of the sensing element of the pressure transducer limits its spatial resolution of the pressure field associated with the turbulent flow. The signal output from the transducer is proportional to an average of the pressure fluctuations over the face of the sensor, and hence, the transducer is unable to resolve accurately those fluctuations having wavelengths of the same order of magnitude as the dimensions of the sensing element. Consequently, there are errors present in the experimental frequency spectral density data, especially in the higher frequency region.

It has been suggested by White (1967) that all measurements which have the condition that

$$(\omega r/U_\infty) > \pi/2 , \qquad 4.10$$

where:

ω is the radial frequency.

r is the radius of the sensing element of the transducer.

U_∞ is the free stream velocity,

are subject to error. From Equation 4.10, errors would be present in measurements obtained using the pressure transducer, with the PITRAN sensing element, for frequencies beyond 6000 Hz. This value was based on a free stream velocity of 192.5 feet per second and a radius of .093 inches.

The following section deals with the attempts by several investigators to obtain suitable corrections for the above phenomena.

4.3.2 Correction Factors

Corcos (1963) analyzed the problem of the finite element size and proposed a semi-empirical estimation of the response of flush mounted transducers

to the pressure field in a turbulent boundary layer. Several other investigators (Gilchrist and Strawderman (1965) and Geib (1968)) have reported experimental data, which, when reduced in a form that corresponds to Corcos' presentation, verify his predictions.

The corrections to be applied to the experimental measurements of the statistical averages related to the space-time covariance of the pressure depend, to a certain extent, upon an "a priori" knowledge of the pressure field. This is shown by the fact that the correction factor,

$$C_f(\omega) = \Phi m/\Phi \qquad 4.11$$

where:

Φm is the measured energy spectral value at a given frequency ω.

Φ is the corrected energy spectral value at the same frequency, was presented in a graphical form (reproduced in Figure 4.11) which showed its dependency on the nondimensional frequency $\omega r/U_c$. Thus a knowledge of the convection velocity, U_c, of the pressure field is needed before the correction factor $C_f(\omega)$ may be applied to the experimental data.

To determine the convection velocity experimentally, it would be necessary to have two flush mounted pressure transducers located along the pipe, and separated by some distance ξ. By measuring the signals from both transducers and performing a space-time cross correlation between them, the delay time τ for which the correlation was a maximum could be obtained. This value would be the time taken for a pressure producing eddy to be convected the distance ξ and hence, the convection velocity could be determined from $U_c = \xi/\tau$. Depending on the separation distance ξ, slightly different values of U_c are obtained, and experimental results show U_c to be dependent to a certain extent on the

frequency or eddy size.

Only one pressure transducer was available and because the above method required two flush mounted pressure transducers, an experimental determination of U_c could not be obtained. However, published results (Bull (1963) and Willmarth and Wooldridge (1962)) show that the convective velocity varies over the frequency range under consideration with $U_c = 0.64\ U_\infty$ for $\omega\delta^* = 5.0\ U_\infty$ and $U_c = 0.78\ U_\infty$ for $\omega\delta^* = .68\ U_\infty$.

In order to get an idea of the magnitude of the errors involved in the spectrum measurements of the pressure fluctuations, the spectral density obtained for $U_\infty = 192.5$ feet per second was plotted in Figure 4.12, with and without the correction factors being applied. For the corrections to be valid, Corcos stated that the ratio r/δ must be small, but a numerical value was not given in the paper. Gilchrist and Strawderman used r/δ ratios of 0.051 and 0.0193 for their experimental verification of Corcos' correction factor and consequently, the r/δ ratio of 0.0566 used in this investigation was initially assumed to be acceptable.

Referring to Figure 4.12 it appears that the corrections which were applied to the energy spectrum were unduly large, as one would expect the corrected curve to be decreasing in a similar manner to that of the uncorrected curve. A possible explanation for the over correction is related to the characteristic dimension which was selected for the PITRAN, because the construction of this sensing element was quite different than for a piezoelectric crystal. The correction factor was determined for use with pressure transducers using piezoelectric crystals which generate changes in electrostatic charge or voltage when stressed by compression or tension forces. These forces act on the whole sensing element and contribute evenly across the surface and consequently, the

radius of the sensor was used by Corcos to be the characteristic length parameter of the transducer. For the PITRAN sensing element, the piezo-junction stress is created with a point force, transmitted from the diaphragm to the emitter-base junction by means of a stylus (see Figure 1.1(a)). In this case, the pressure forces applied across the face of the sensor do not contribute evenly to the induced stress in the junction, and hence the radius of the diaphragm would not be a length parameter comparable to the radius of a piezoelectric crystal.

It thus appears that the correction factors obtained by Corcos cannot be used directly to determine the true power spectral density curve for fluctuating wall pressures measured with a pressure transducer using a PITRAN sensing element.

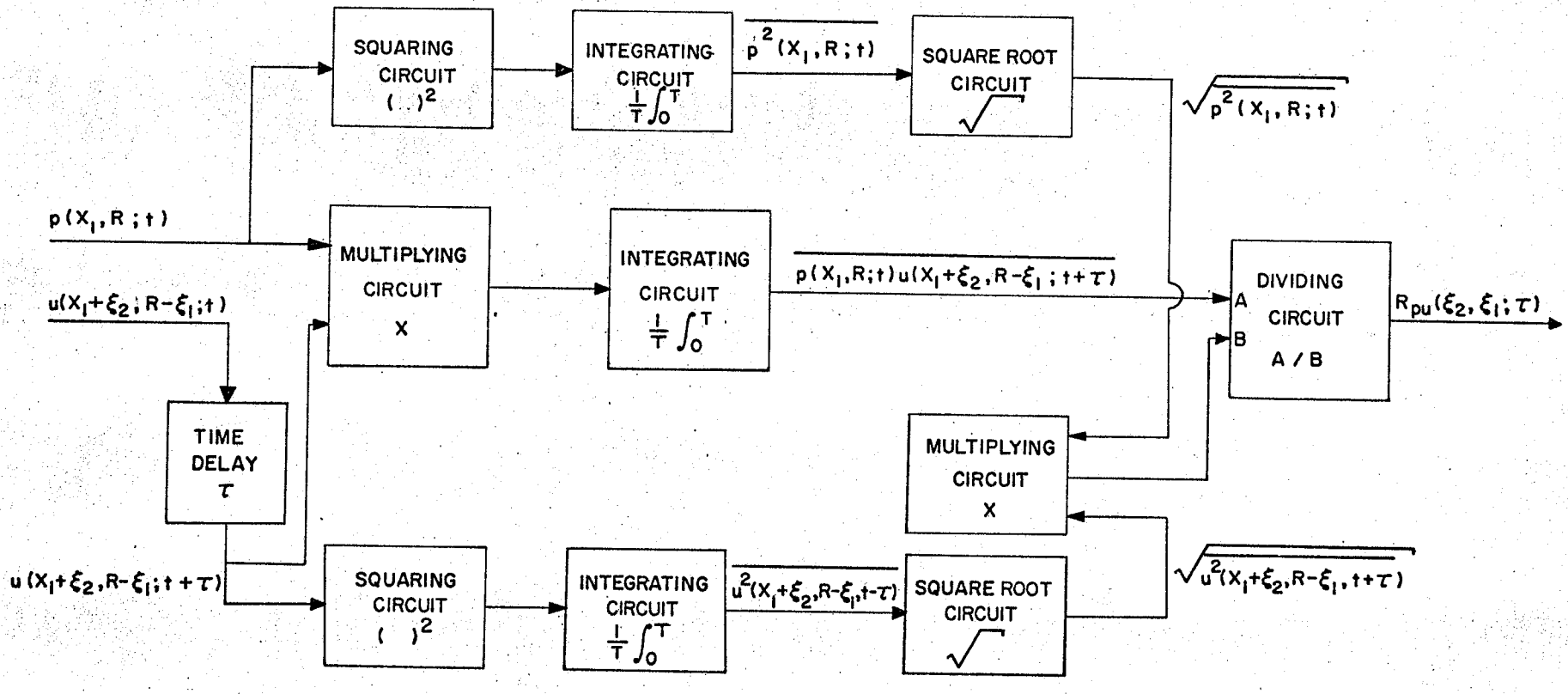

FIGURE 4.1 BLOCK DIAGRAM OF ANALOGUE CIRCUIT USED FOR CORRELATION MEASUREMENTS.

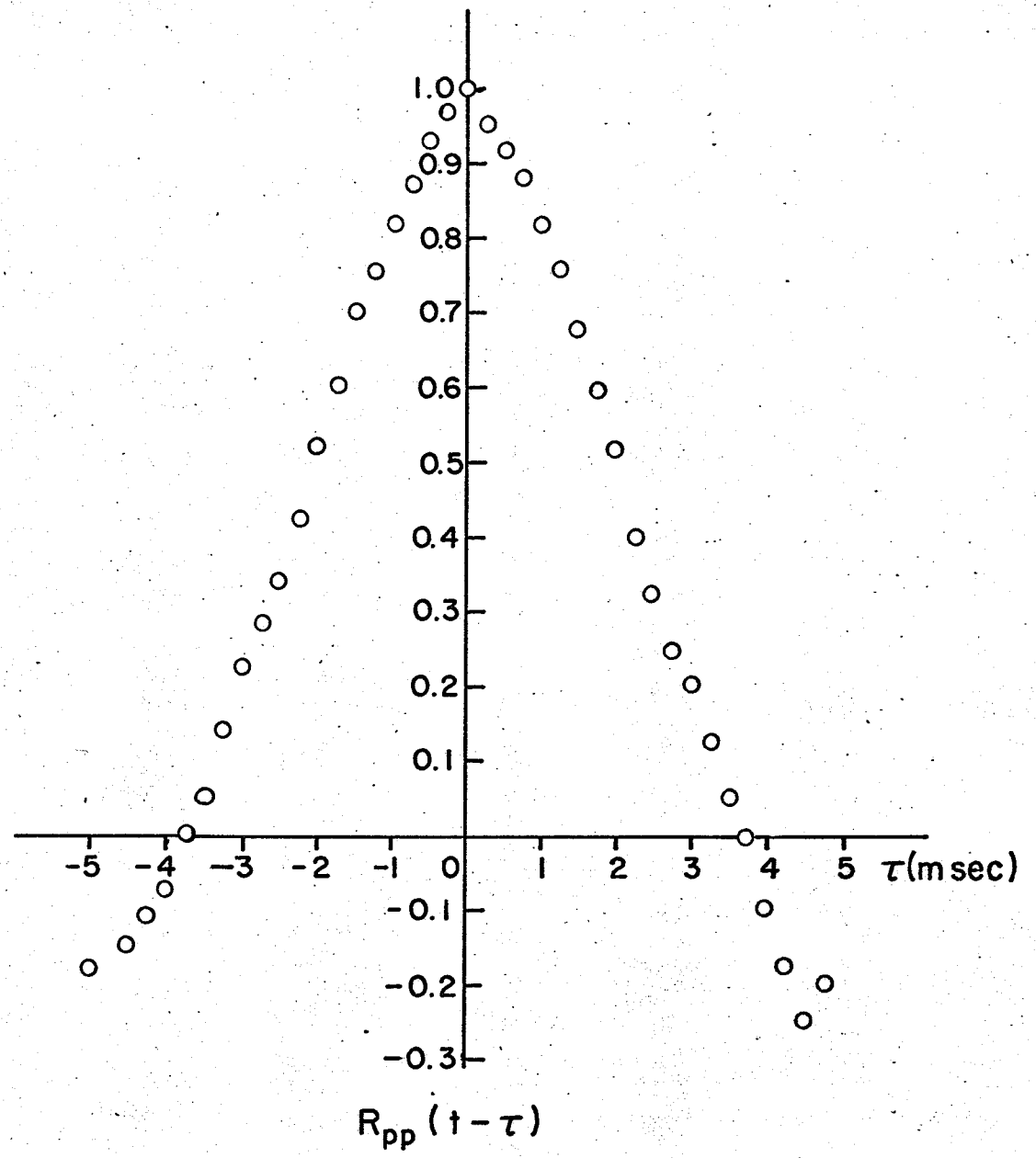

FIGURE 4.2 AUTO CORRELATION OF WALL PRESSURE FLUCTUATIONS FOR A TUNNEL SPEED OF 192.5 FEET PER SECOND.

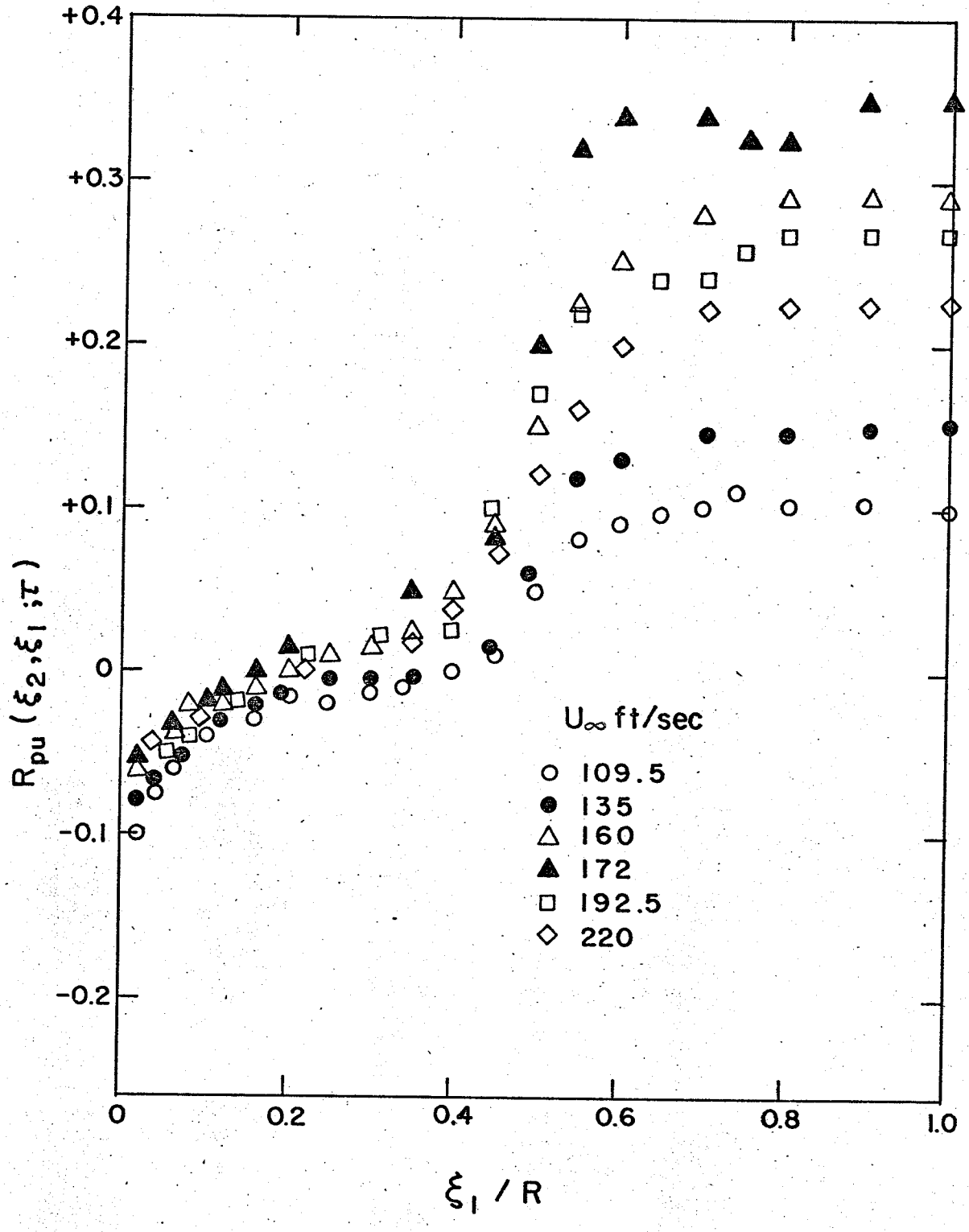

FIGURE 4.3 CROSS CORRELATION COEFFICIENTS R_{pu} FOR:

(a) $\xi_2 = 0$, $\tau = 0$.

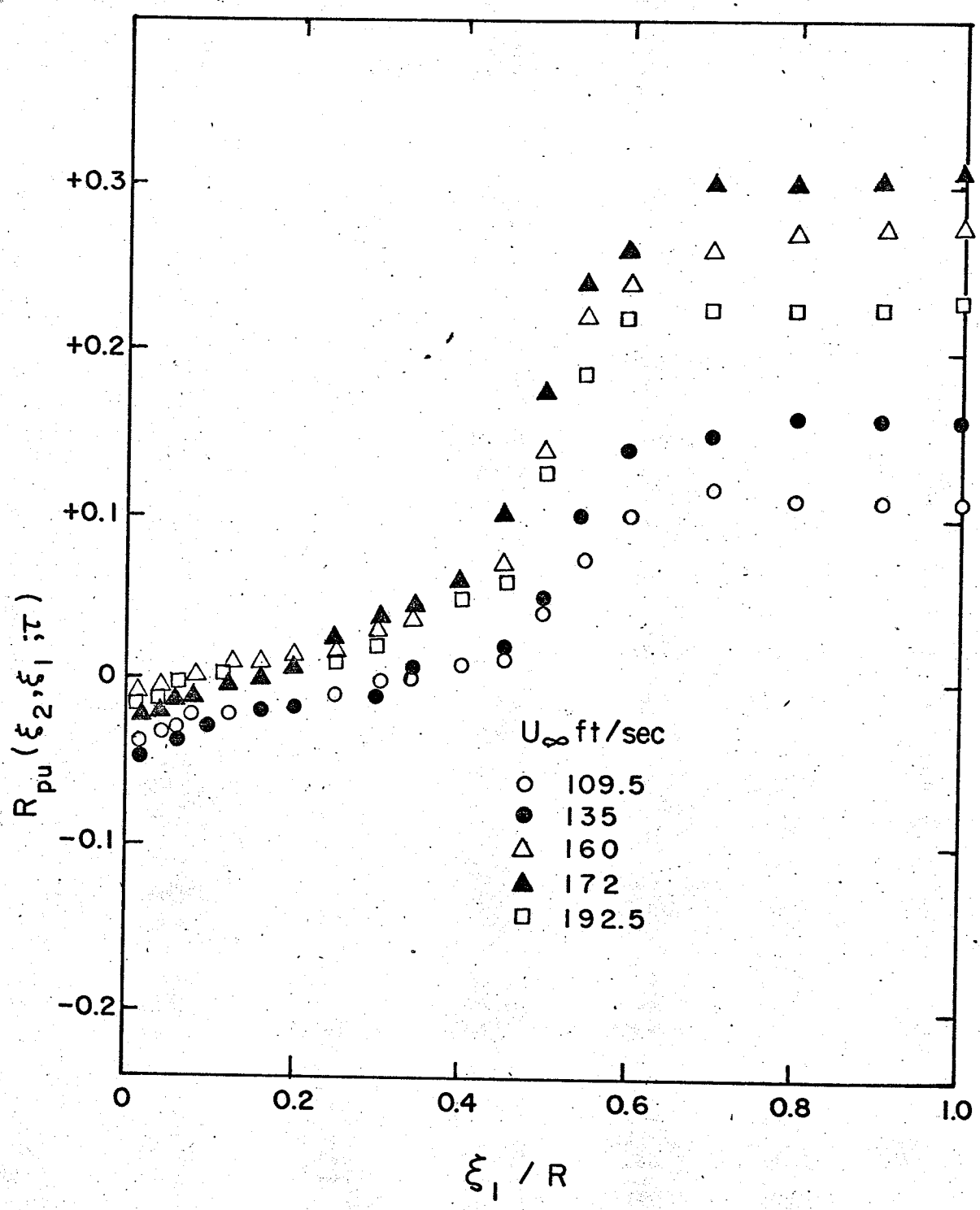

FIGURE 4.3(b) ξ_2 = .0164 ft, τ = 0.

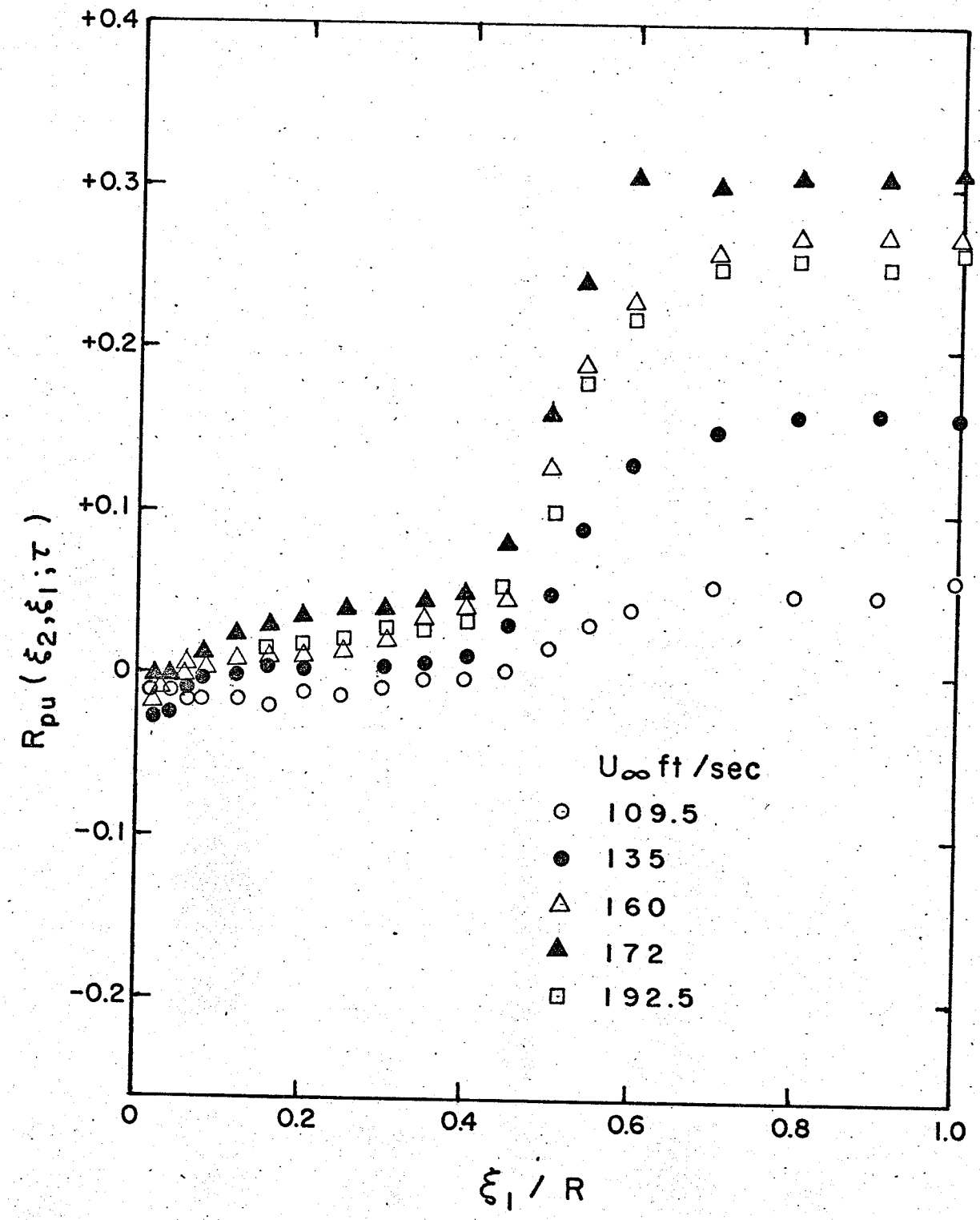

FIGURE 4.3(c) ξ_2 = .0328 ft, τ = 0.

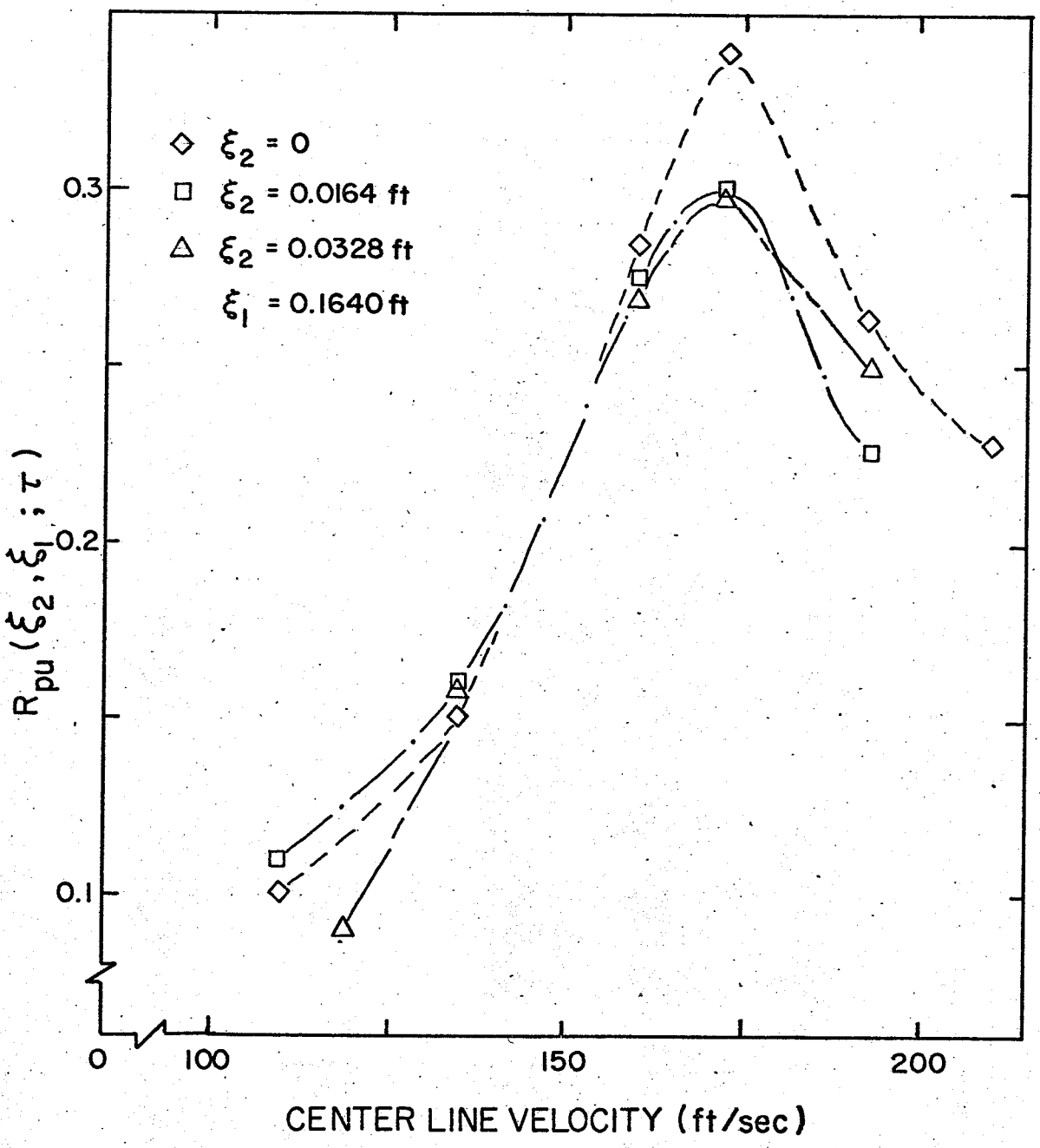

FIGURE 4.4 VELOCITY DEPENDENCY OF R_{pu} IN THE FREE STREAM REGION.

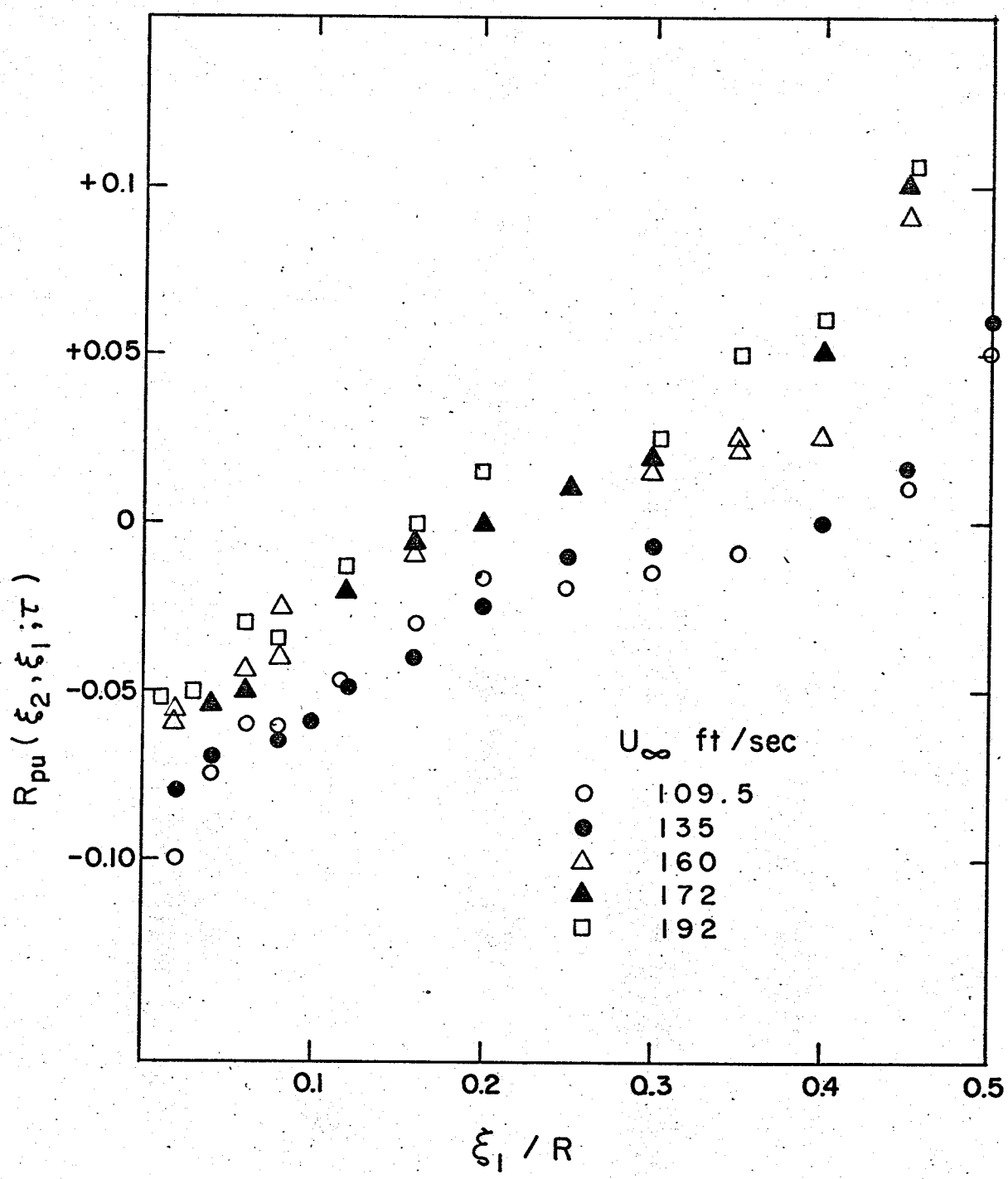

FIGURE 4.5 CROSS CORRELATION COEFFICIENTS, R_{pu} PRESENTED WITH AN EXPANDED SCALE FOR:

(a) $\xi_2 = 0, \tau = 0.$

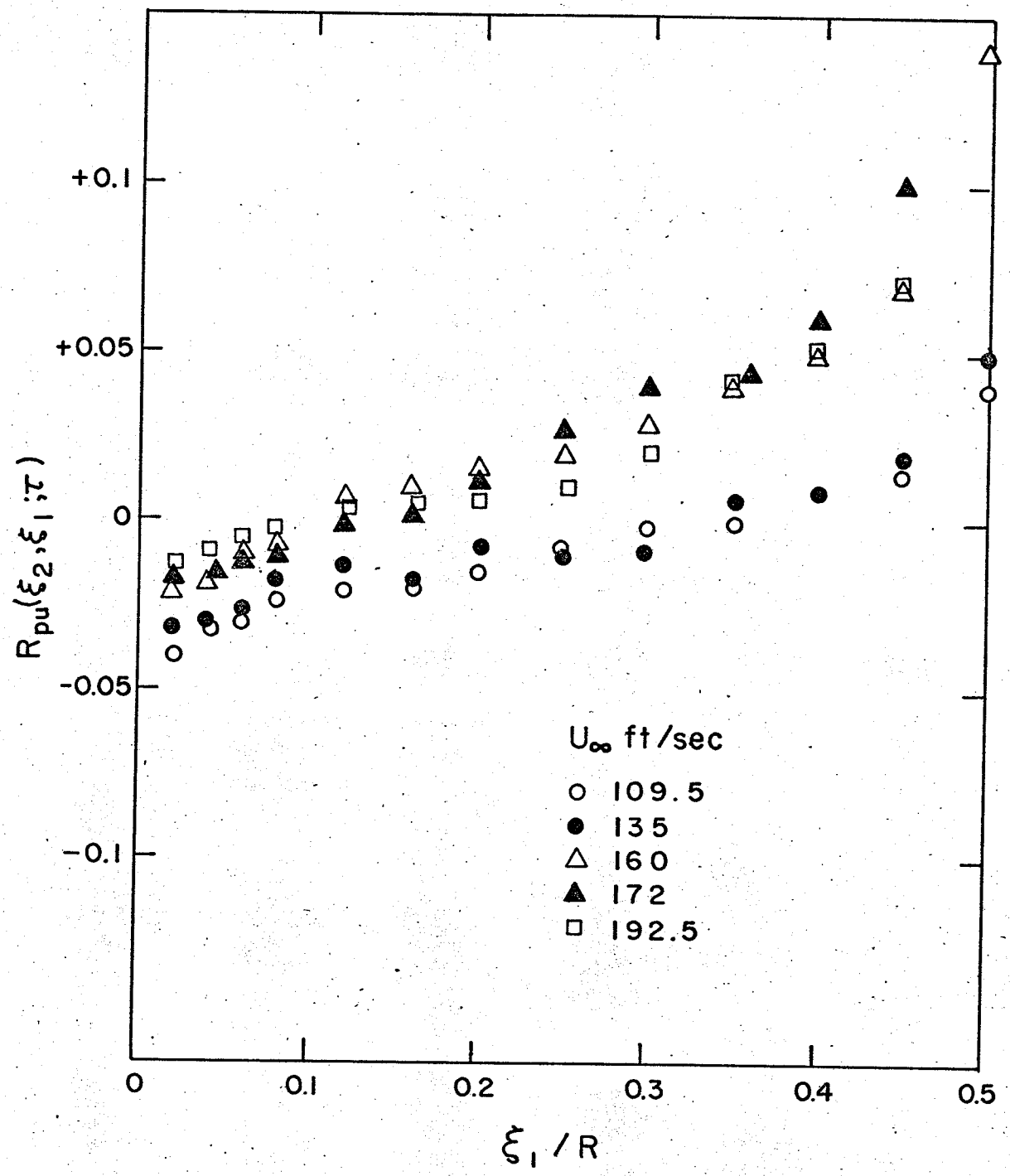

FIGURE 4.5(b) $\xi_2 = .0164$, $\tau = 0$.

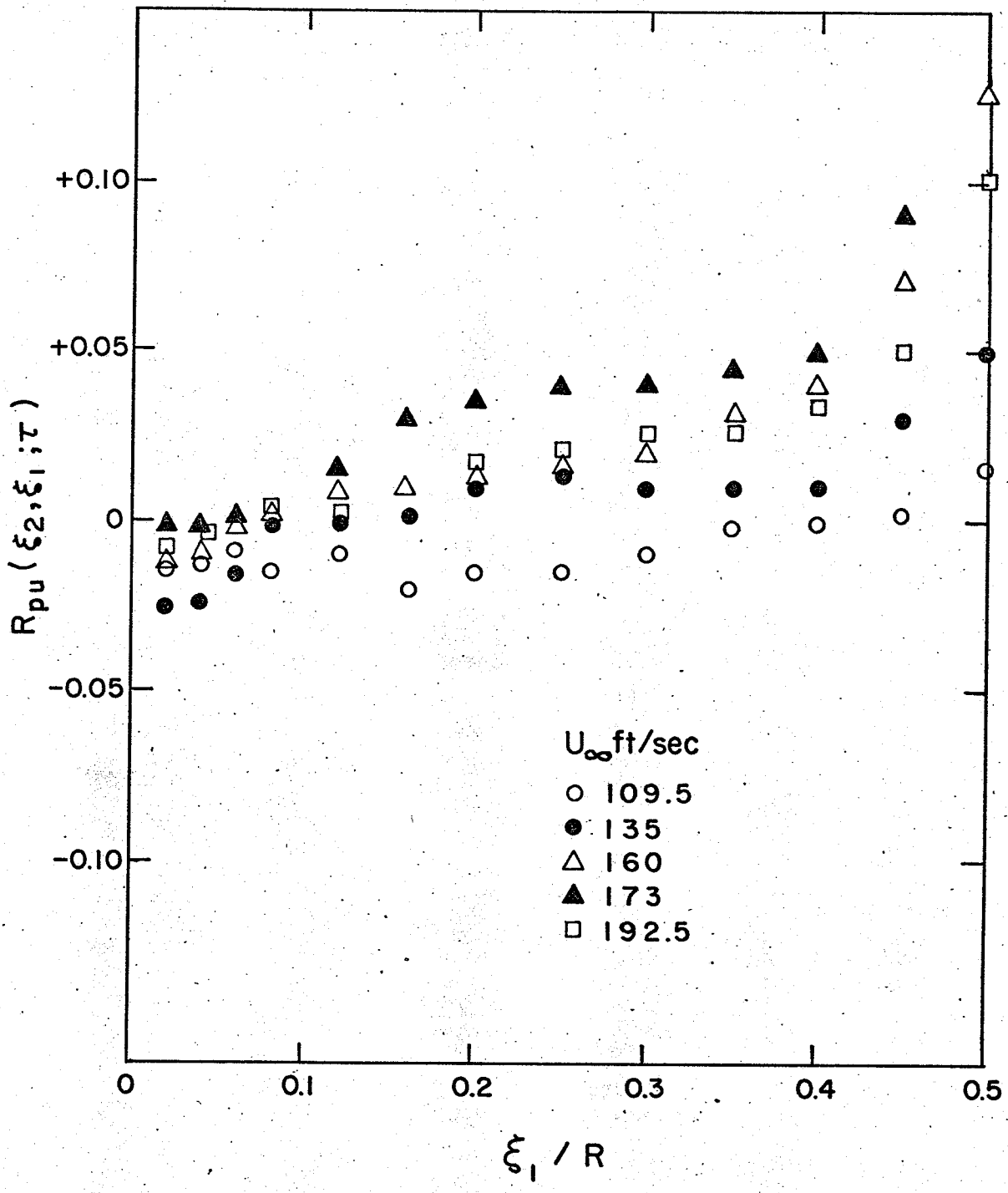

FIGURE 4.5(c) ξ_2 = .0328 ft, τ = 0.

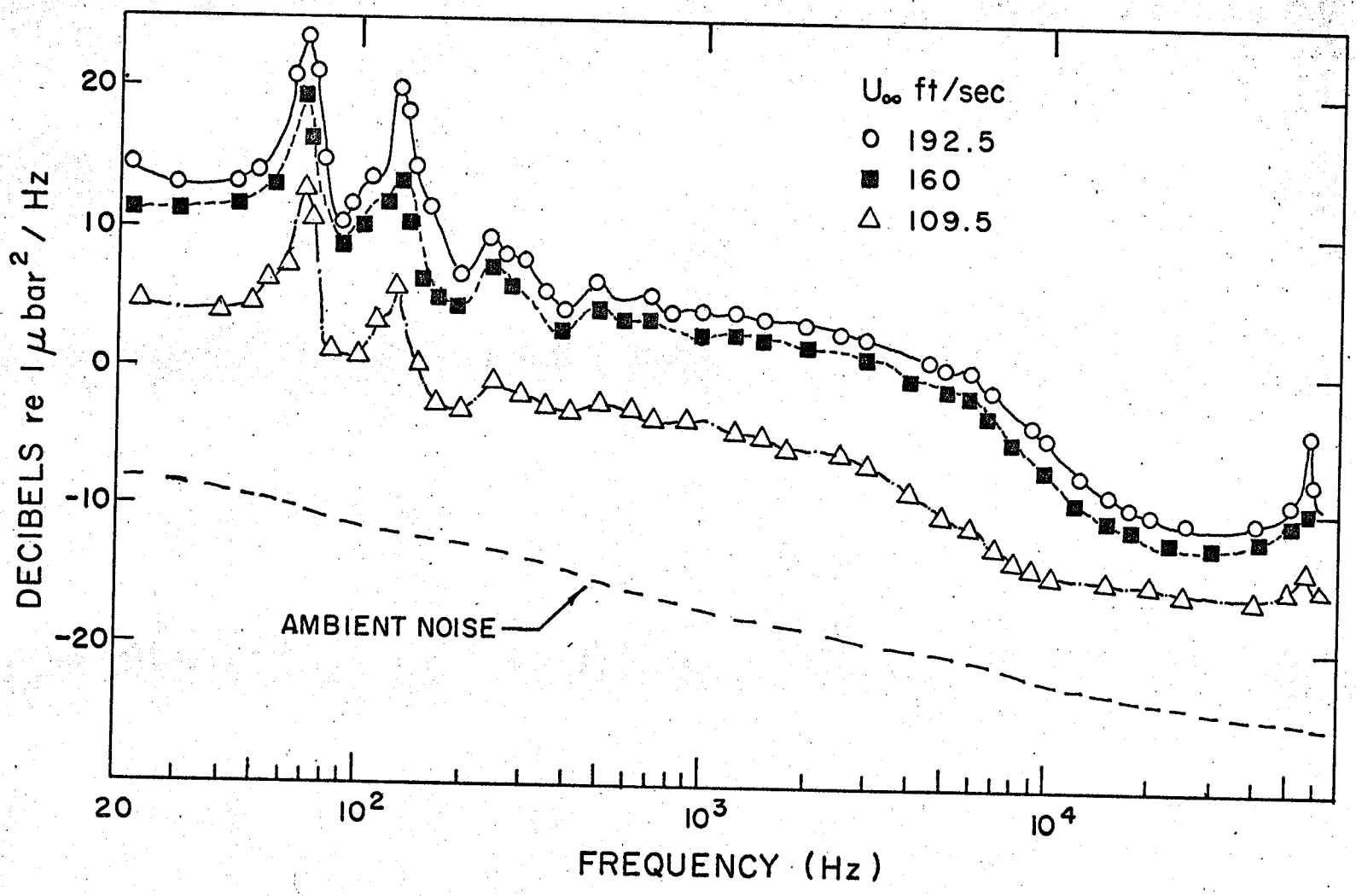

FIGURE 4.7 POWER SPECTRAL DENSITIES OF THE WALL PRESSURE FLUCTUATIONS.

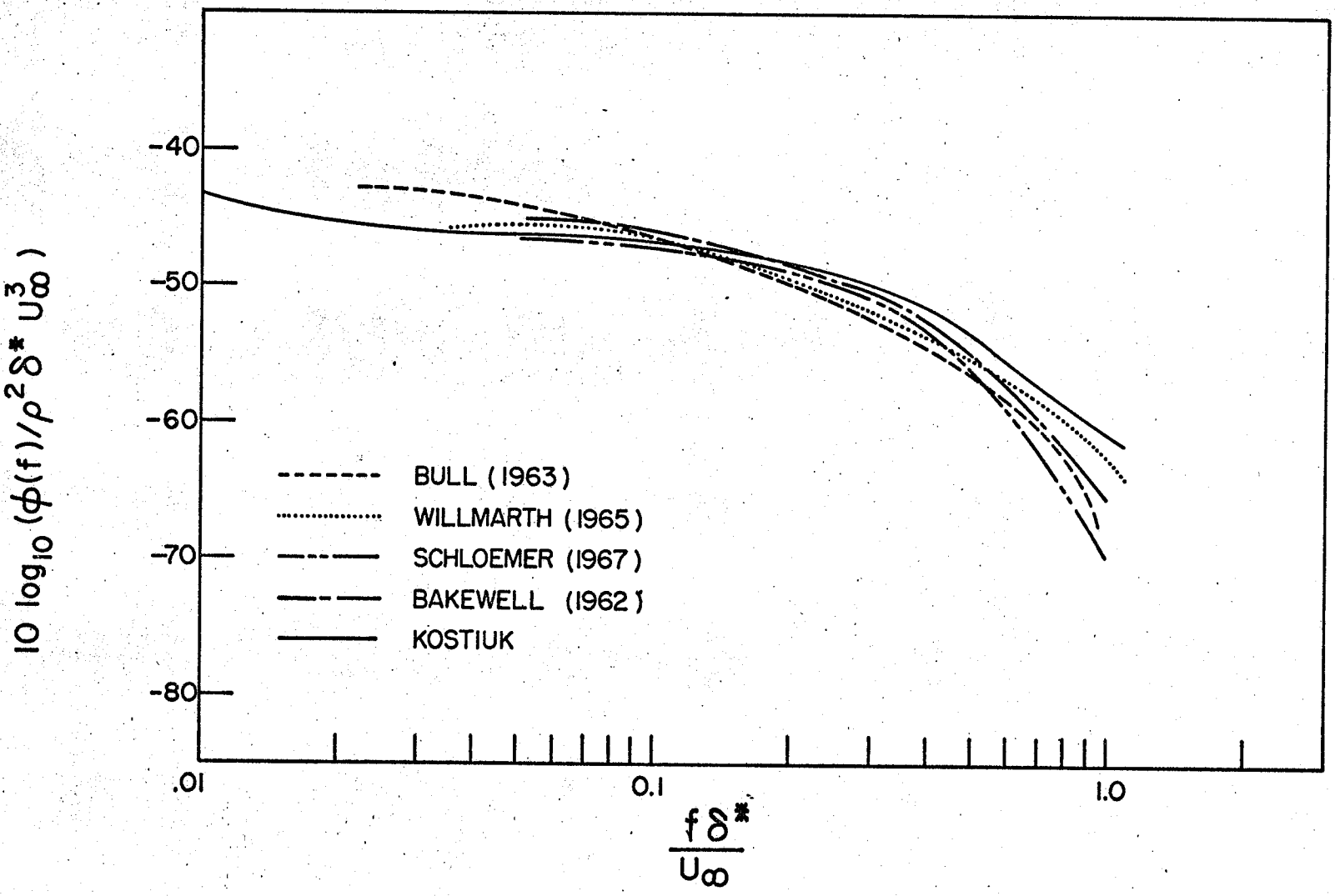

FIGURE 4.8 NONDIMENSIONALIZED POWER SPECTRAL DENSITIES FOR FLUCTUATING WALL PRESSURES BENEATH A TURBULENT BOUNDARY LAYER.

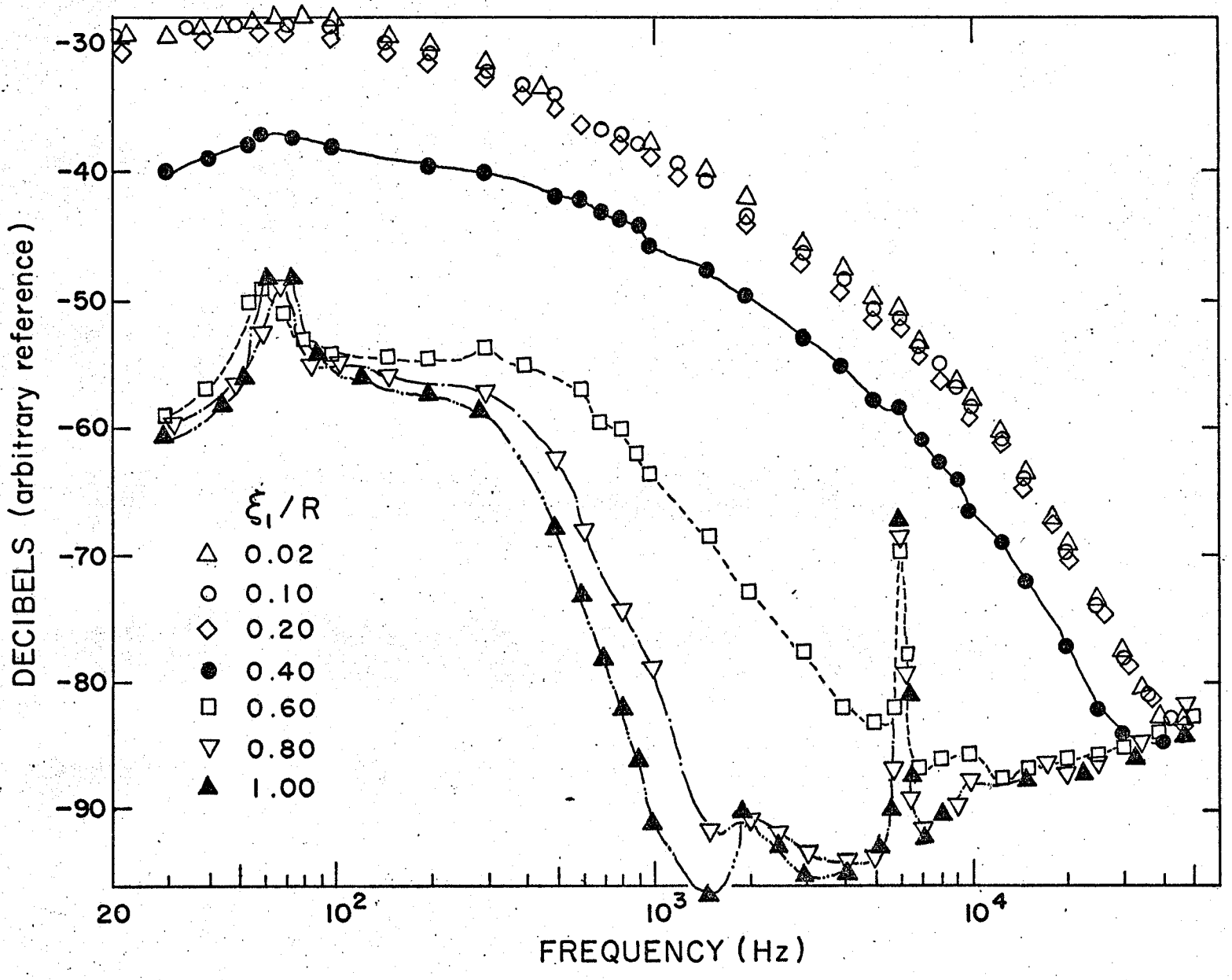

FIGURE 4.9 POWER SPECTRAL DENSITY MEASUREMENTS OF THE FLUCTUATING VELOCITY COMPONENT IN THE AXIAL DIRECTION FOR $\xi_2=0$ and: (a) $U_\infty=109.5$ ft/sec.

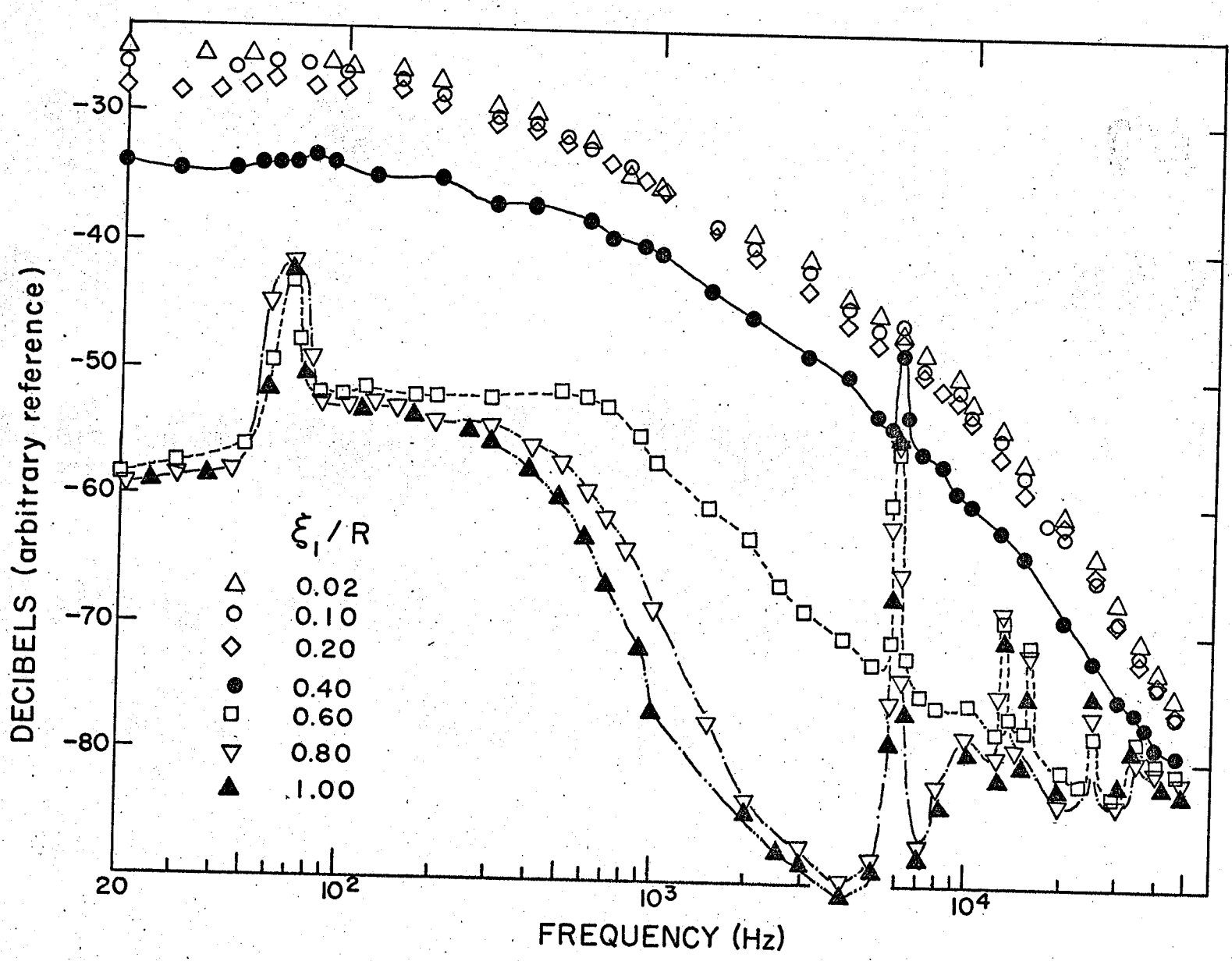

FIGURE 4.9(b) U_∞ = 160 ft/sec.

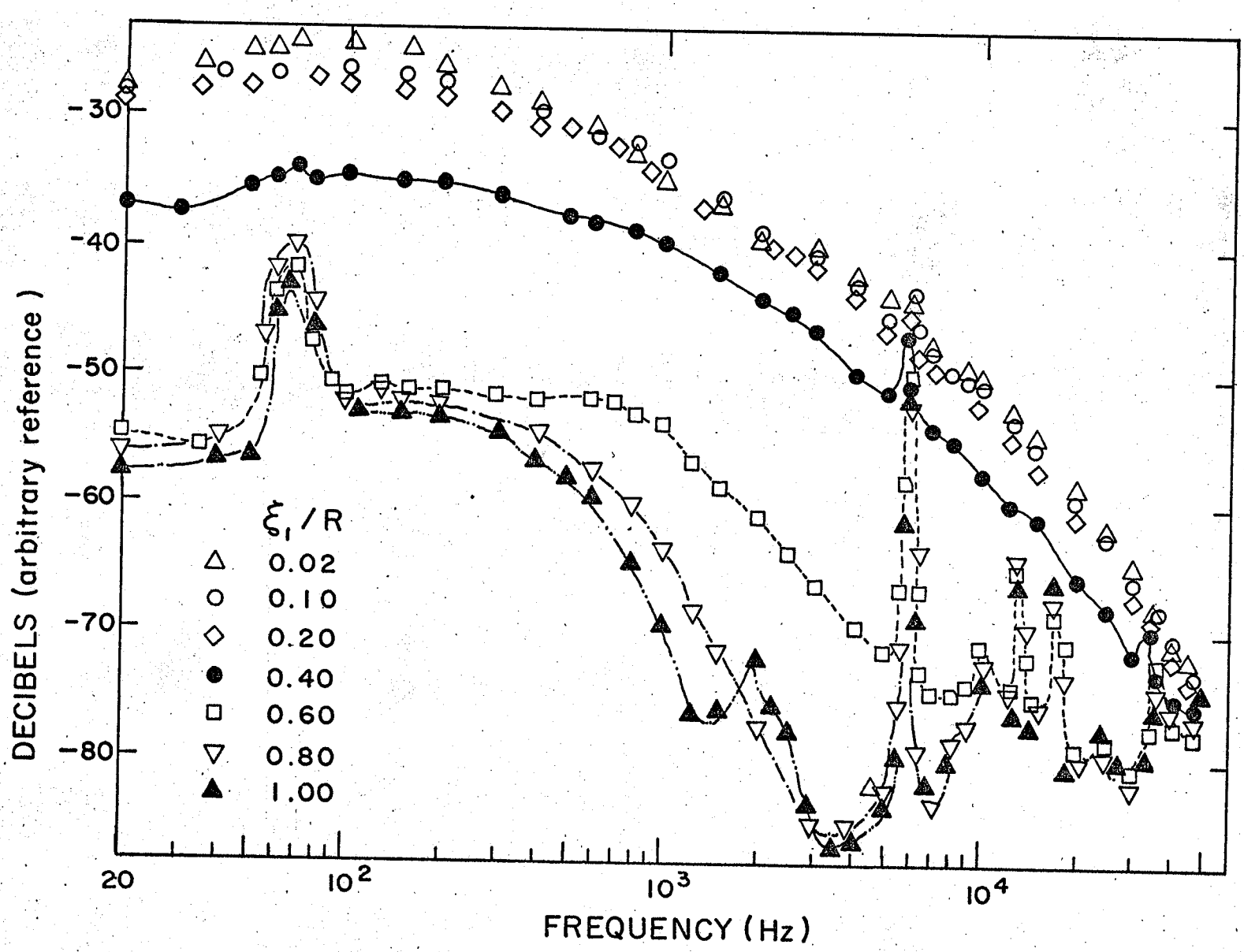

FIGURE 4.9(c) U_∞ = 192.5 ft/sec.

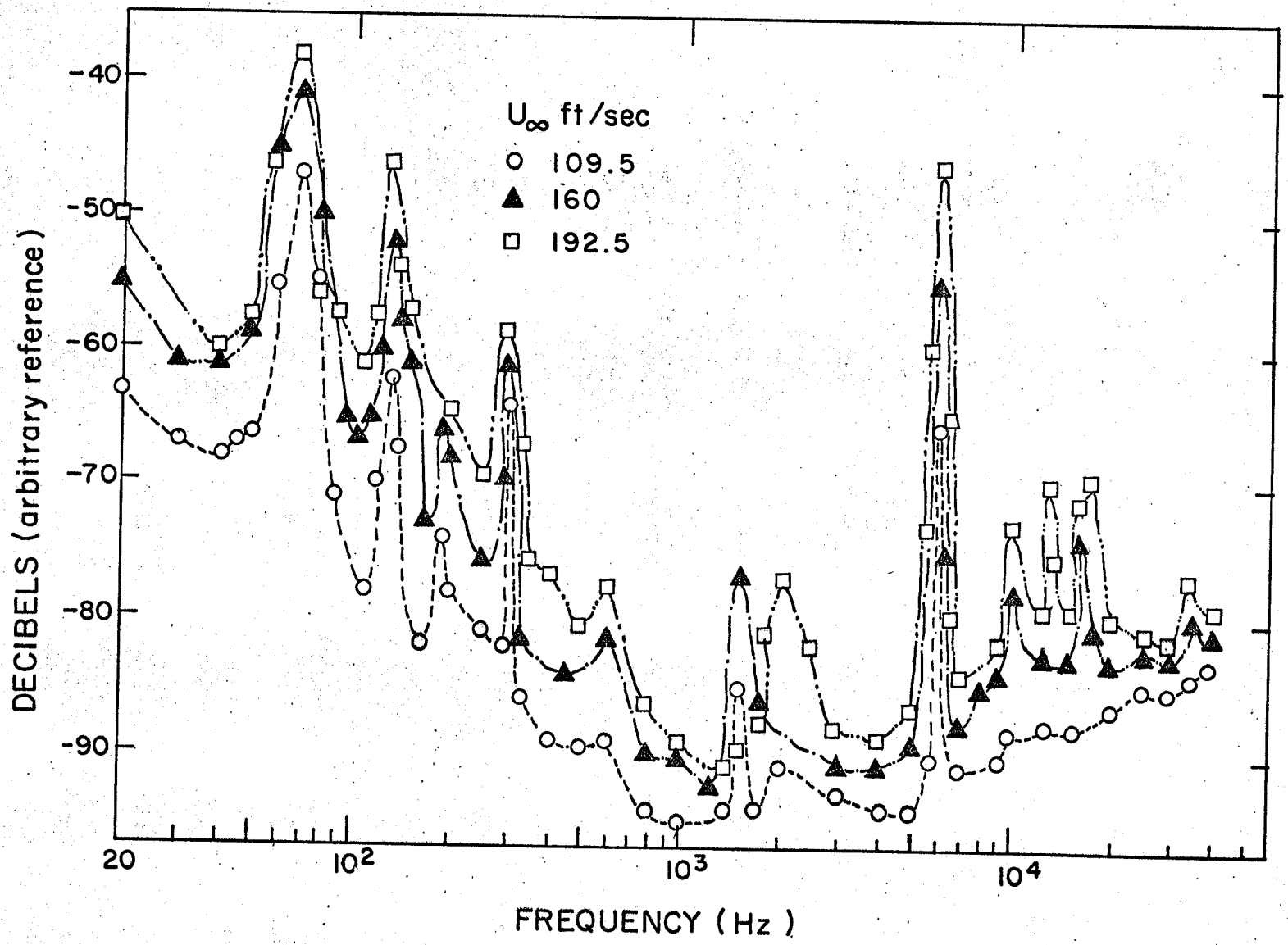

FIGURE 4.10 POWER SPECTRAL DENSITIES OF THE FLUCTUATING VELOCITY COMPONENT IN THE AXIAL DIRECTION MEASURED AT THE EXIT OF THE CONTRACTION CONE WITH $x = 0$ and $\xi_1/R = 1$.

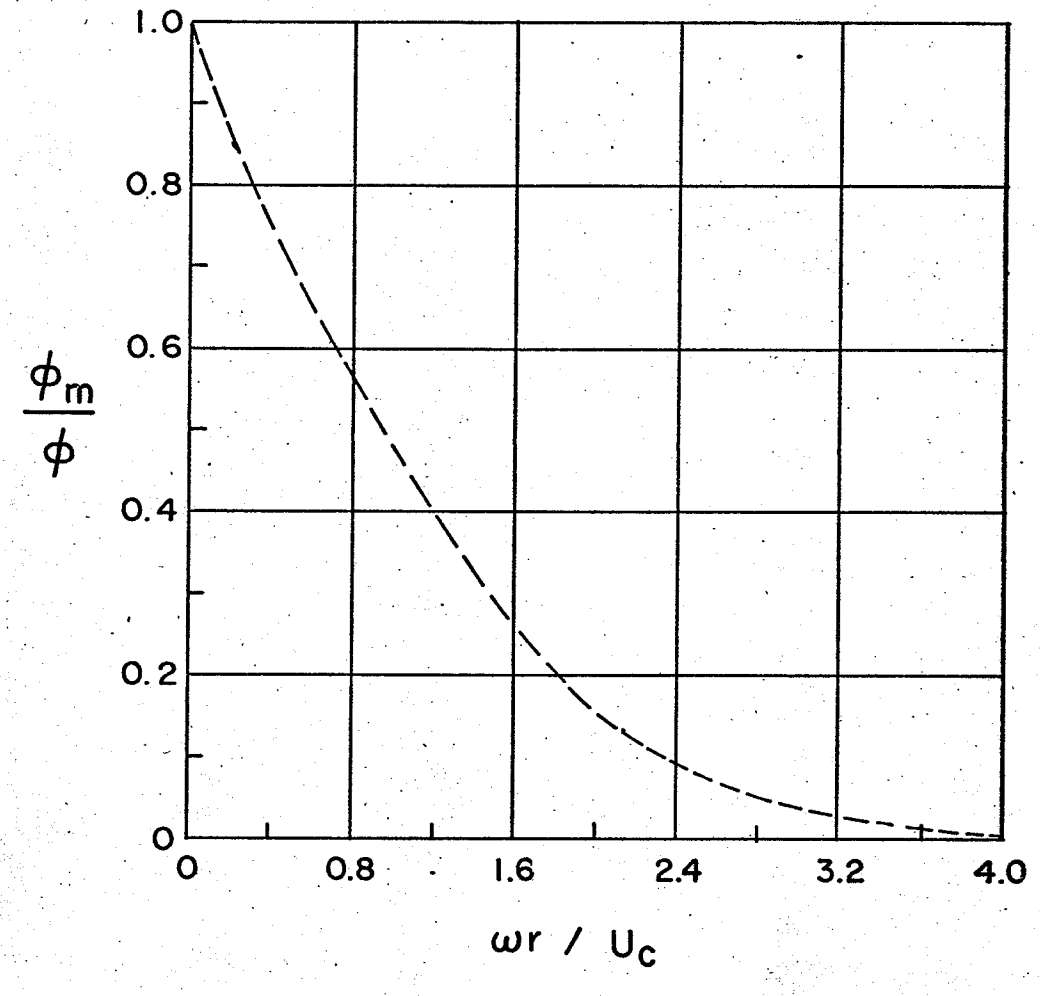

FIGURE 4.11 ATTENUATION OF THE FREQUENCY SPECTRAL DENSITY BY A ROUND PRESSURE TRANSDUCER (AFTER CORCOS (1963)).

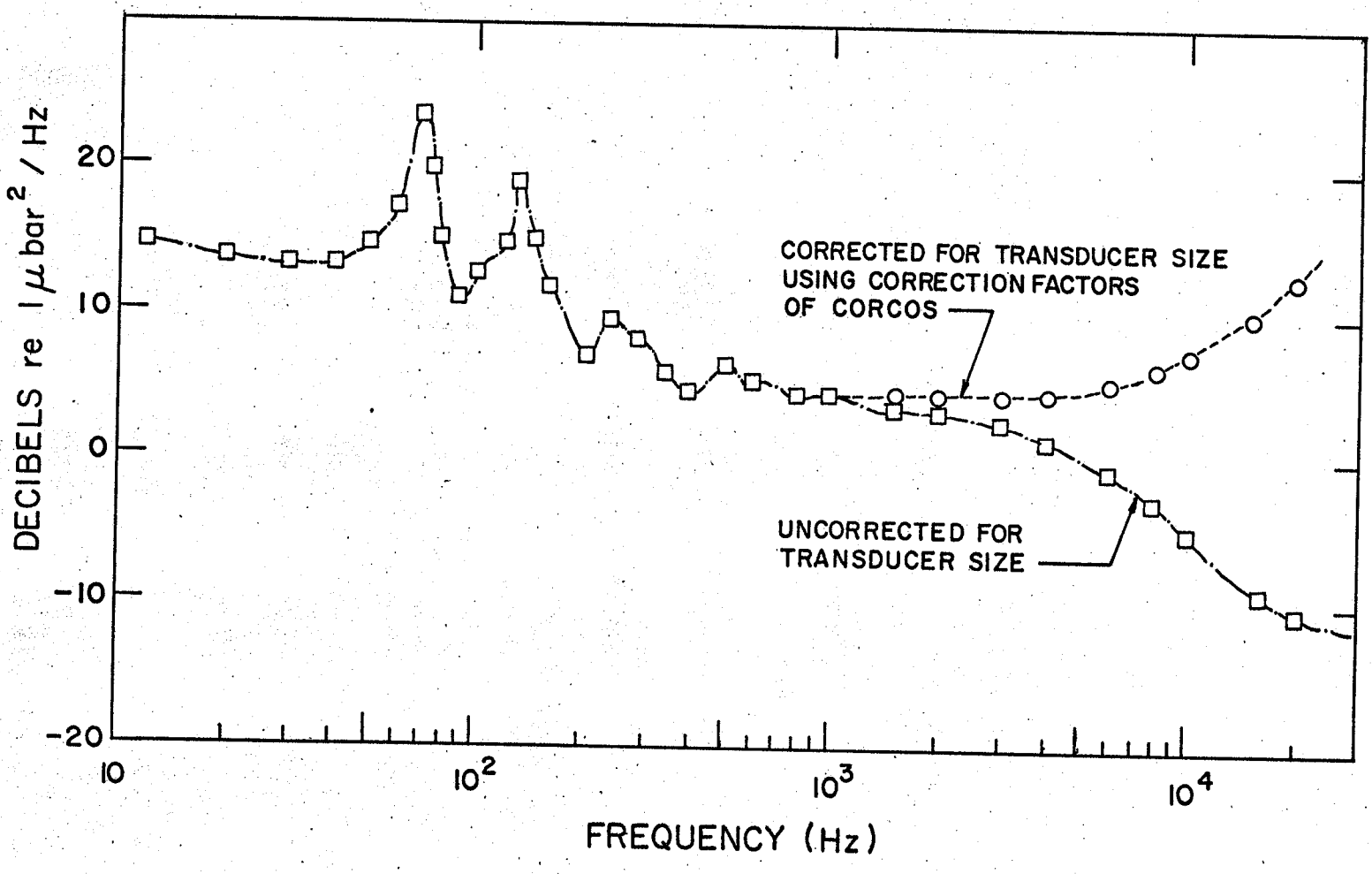

FIGURE 4.12 CORRECTED AND UNCORRECTED POWER SPECTRAL DENSITIES OF FLUCTUATING WALL PRESSURES OBTAINED FOR U_∞ = 192.5 ft/sec AND ξ_2 = 0.

CHAPTER 5

CONCLUSIONS AND RECOMMENDATIONS.

5.1 Conclusions.

The main results of this experimental investigation can be summarized as follows:

(1) Using a piezojunction sensing element (a PITRAN), a pressure transducer capable of measuring both static and transient pressures, as found in turbulence studies, has been developed. In the static mode of operation the calibration curve showed a ±1.5% F.S.O. independent linearity, a 3% F.S.O. hysteresis, and a repeatability of .5% F.S.O. The transducer exhibited a thermal sensitivity shift of 0.15% F.S.O./^{o}F and a thermal zero shift of 1% F.S.O./^{o}F. In the dynamic mode of operation, the transducer exhibited a flat (±1 db re .0002 μ bar) frequency response from 0 to 20 KHz and had a mechanical resonant frequency of 58 KHz. Measurements of the fluctuating wall pressures, obtained using this pressure transducer in a turbulent boundary layer, compared very well with results published by other investigators using piezoelectric crystals. The good agreement between the results confirms that this pressure transducer can be used with confidence, for the measurement of wall pressure fluctuations as found in turbulent boundary layers.

(2) The turbulence intensity profiles, which were obtained from hot-wire measurements in the turbulent boundary layer of a developing pipe flow, exhibited the same general trends as those presented by Klebanoff (1954) and Willmarth and Wooldridge (1963) for a flat plate and by Laufer (1954) for fully developed pipe flow. From these measurements, a dependence on

the free stream velocity U_∞ was observed with the intensity levels in the inner region of the flow field ($\xi_1/R < .5$) decreasing with increasing U_∞. In the free stream region ($\xi_1/R > .6$) the intensity levels increased with increasing U_∞ until a maximum was reached at $U_\infty = 172$ ft/sec. As the flow rate was increased further, there was a slight decrease in the turbulence level.

(3) From a comparison of the pressure and velocity spectral densities and R_{pu} correlation measurements, it appears that the flow field in the free stream region of the flow consists of large scale ($f < 100$ Hz) pulsations on which small scale ($f > 6000$ Hz) eddies are superimposed. In the boundary layer there were no predominant scales of eddies present except at a flow rate of $U_\infty = 192.5$ feet per second, where the influence of the small scale eddies (6000 Hz) in the free stream was detected.

(4) From the cross correlation measurements and energy spectra of the fluctuating velocity components and fluctuating wall pressures it appears that the wall pressure fluctuations in developing pipe flow are a result of the interaction of two pressure fields.

(a) The pressure field associated with the large scale eddies in the free stream region which is transmitted through the boundary layer.

(b) The pressure field produced by the small scale eddies in the boundary layer.

(5) The orders of magnitude of the absolute numerical values of the velocity gradients $\delta\sqrt{\overline{u^2}}/\delta\xi_2$, $\delta\sqrt{\overline{u^2}}/\delta r$ and $\delta U/\delta r$ were determined to be in the ratios of 10, 100 and 1000 respectively.

(6) In the boundary layer region the cross correlation coefficient changed from a positive to a negative correlation, with the point of reversal being shifted closer to the wall as the separation vector ξ_2 was

increased. This reversal in sign for the correlation coefficient has been also reported for a turbulent boundary layer of a flat plate by Kawamura (1960) and Bradshaw (1967) who attributed it to the fact that the pressure fluctuation is more nearly in phase with $\delta u/\delta x$ than $\ddot{u}$ in the region where the reversal occurred.

(7) The finite size of the sensing element of the pressure transducer limits its spatial resolution of the pressure field associated with the turbulent flow. Corcos (1963) proposed a semi-empirical estimation of the errors introduced in spectral density measurements obtained using piezoelectric crystals as the sensing element. However, due to the difference in construction between a piezoelectric sensing element and the PITRAN, the correction factors proposed by Corcos could not be used.

5.2 Recommendations.

The energy spectra and cross correlations were measured primarily at one station along the pipe and in order to do a detailed analysis of developing pipe flow, many more stations must be considered. Future investigations of a developing pipe flow should include:

(a) Measurements obtained at several positions along the pipe section in which the flow is developing, and in a region of fully developed pipe flow in order to check that experimental and data reduction techniques are correct.

(b) Measurements of the intermittency factor .

(c) Cross correlation measurements between $\partial\sqrt{\overline{u^2}}/\partial x$ and the wall pressure fluctuations to validate Bradshaw's argument (1967) of why the correlation curves change sign.

(d) A detailed analysis of the shear stress developed at the wall.

REFERENCES

Bakewell, H.P., et al., 1962, "Wall pressure correlations in turbulent pipe flow", U.S.N. Underwater Sound Lab. Rept. 559.

Bradshaw, P., 1967, "Inactive motion and pressure fluctuations in turbulent boundary layers", J. Fluid Mech., 30.

Bull, M.K., 1963, "Properties of the fluctuating wall-pressure field of a turbulent boundary layer", Univ. Southampton A.A.S.U. Rept. 234.

Clauser, F.H., 1954a,"Turbulent boundary layers in adverse pressure gradients", J. of Aero. Sciences, 21.

Corcos, G.M., 1963, "Resolution of pressure in turbulence", J. Acoust. Soc. Amer.,35.

Corcos, G.M., 1963, "The structure of the turbulent pressure field in boundary layer flows", J. Fluid Mech., 18.

Freison, G., 1970, "A theoretical and experimental study of contraction cones", M.Sc. Thesis, University of Manitoba.

Geib, F.E., 1969, "Measurements on the effect of transducer size on the resolution of boundary layer pressure fluctuations", J. Acoust. Soc. Amer., 46.

Gilchrist, R.B. and Strawderman, W.A., 1965, "Experimental hydrophone-size correction factors for boundary layer pressure fluctuations", J. Acoust. Soc. Amer., 38.

Hofland, R. and Glick, H.S., 1969, "A miniature transducer for measuring low transient pressures", Rev. Sci. Instrum., 40.

Hummel, R.H., 1970, "Intermittency measuring techniques using a probability density analyzer", M.Sc. Thesis, University of Manitoba.

Kavak, I., 1970, "Conductive rubber pressure transducers for fluids research", Rev. Sci. Instrum., 41.

Kawamura, M., 1960, "Pressure-velocity correlation and double velocity correlation in a turbulent boundary layer along a flat plate", J. Sci., Hiroshima Univ., Ser. A, 24.

Klebanoff, P.S., 1954, "Characteristics of turbulence in a boundary layer with zero pressure gradient", NACA Tech. Note 3178.

Kraichnan, R.H., 1956, "Pressure fluctuations in turbulent flow over a flat plate", J. Acoust. Soc. Amer., 28.

Krueger, H., 1970, "Turbulent flow in a straight conical diffuser", M.Sc. Thesis, University of Manitoba.

REFERENCES (continued)

Laufer, J., 1954, "The structure of turbulence in fully developed pipe flow" NACA Report, 1174.

Patel, V.C., 1965, "Calibration of the preston tube and limitations on its use in pressure gradients", J. Fluid Mech., 23.

Preston, J.H., 1954, "The determination of turbulent skin friction by means of Pitot tubes", J. Roy. Aero. Soc., 58.

Schloemer, H.H., 1967, "Effects of pressure gradients on turbulent-boundary-layer wall-pressure fluctuations", J. Acoust. Soc. Amer.,42.

Schraub, F.A. and Kline, S.J., 1965a, "A study of the structure of the turbulent boundary layer with and without longitudinal pressure gradients", Mech. Engrg. Dept. Rept. MD-12, Stanford University.

Slusar, G.G., 1969, "Turbulence measurements in a straight conical diffuser", M.Sc. Thesis, University of Manitoba.

Taylor, G.I., 1938, "Correlation measurements in a turbulent flow through a pipe", Proc. Roy. Soc. London, A157.

Tu, B.J. and Willmarth, W.W., 1966, "An experimental study of the structure of turbulence near the wall through correlation measurements in a thick boundary layer", Univ. of Michigan Tech. Rept. ORA 02920-3-T.

White, P.H., 1967, "Effect of transducer size, shape and surface sensitivity on the measurement of boundary layer pressures", J. Acoust. Soc. of Amer., 41.

Willmarth, W.W., 1956, "Wall pressure fluctuations in a turbulent boundary layer", NACA Technical note, 4139.

Willmarth, W.W., 1958, "Small barium titanate transducer for aerodynamic or acoustic pressure measurements", Rev. Sci. Instrum., 29.

Willmarth, W.W. and Wooldridge, C.E., 1962, "Measurements of the fluctuating pressure at the wall beneath a thick turbulent boundary layer", J. Fluid Mech., 14.

Willmarth, W.W. and Wooldridge, C.E., 1963, "Measurements of the correlation between the fluctuating velocities and the fluctuating wall pressure in a thick turbulent boundary layer", NATO Report, 456.

Willmarth, W.W., 1965, "Corrigendum: Measurements of the fluctuating pressure at the wall beneath a thick turbulent boundary layer", J. Fluid Mech., 21.

REFERENCES (continued)

Willmarth, W.W. and Tu, B.J., 1967, "Structure of turbulence in the boundary layer near the wall", Physics of Fluids Supplement.

Wills, J.A.B., 1962, "The correction of hot-wire readings for proximity to a solid boundary", J. Fluid Mech., 12.

York, T.M., 1970, "Stress dynamics in high speed piezoelectric pressure probes", Rev. Sci. Instrum., 41.

APPENDIX A.1

EQUATIONS RELATING PRESSURE FLUCTUATIONS TO MEAN VELOCITY GRADIENTS.

Using the relevant Navier-Stokes equation for turbulent flow, it is possible to express a relationship between the fluctuating pressures and fluctuating velocities. This is important as it enables one to obtain an idea of the pressure field through direct measurements of the velocity field.

The following is a summarized version of the mathematical treatment of the problem as presented by Corcos (1963).

By taking the divergence of each term of the Navier-Stokes equation for turbulent flow, and making use of the continuity equation, the following expression results:

$$\nabla^2 P = -\rho_o \frac{\partial^2 V_i V_j}{\partial x_i \partial x_j}, \qquad \text{A.1}$$

where:

P is the pressure.

V is the velocity vector.

x is the position vector.

ρ_o is the fluid density,

and the repeated index denotes summation over all three components, in the ordinary cartesian convention. Both the pressure and velocity terms are made up of a mean and a fluctuating component and are denoted by:

$$P = \overline{P} + p'$$

$$V_i = U_i + u_i$$

$$V_j = U_j + u_j$$

When the above are substituted into Equation A.1 the following equation results:

$$\nabla^2 P + \nabla^2 p' = -\rho_o \left\{ \frac{\partial U_j}{\partial x_i} \frac{\partial U_i}{\partial x_j} + 2\frac{\partial U_i}{\partial x_j} \frac{\partial u_j}{\partial x_i} + \frac{\partial u_j}{\partial x_i} \frac{\partial u_i}{\partial x_j} \right\} \qquad A.2$$

If a time average of the terms in the above equation is taken and the resulting expression is subtracted from this equation, the resulting equation can be written as:

$$\nabla^2 p' = -\rho_o \left[2 \frac{\partial U_i}{\partial x_j} \frac{\partial u_j}{\partial x_i} + \left\{ \frac{\partial^2 u_i u_j}{\partial x_i \partial x_j} - \frac{\partial^2 \overline{u_i u_j}}{\partial x_i \partial x_j} \right\} \right] \qquad A.3$$

where:

$$\frac{\partial u_i}{\partial x_j} \frac{\partial u_j}{\partial x_i} = \frac{\partial^2 (u_i u_j)}{\partial x_i \partial x_j} \quad .$$

The two terms contributing to the right hand side, which define the velocity field, can be referred to as the mean shear-turbulence interaction and the turbulence-turbulence interactions respectively.

If, the turbulence-turbulence interaction term can be considered negligible, then for two dimensional flow, Equation A.3 becomes

$$\nabla^2 p' = -2\rho_o \frac{\partial U_i}{\partial x_j} \frac{\partial u_j}{\partial x_i}$$

$$= -2\rho_o \left[\frac{\partial U}{\partial x} \frac{\partial u}{\partial x} + \frac{\partial V}{\partial y} \frac{\partial v}{\partial y} + \frac{\partial U}{\partial y} \frac{\partial v}{\partial x} + \frac{\partial V}{\partial x} \frac{\partial u}{\partial y} \right] , \qquad A.4$$

where U and V are the components of mean velocity and u and v are the fluctuating components of velocity in the x and y directions, respectively.

By assuming the following terms are small,

$$\left\{ \frac{\partial U}{\partial x} \frac{\partial u}{\partial x} \right\} , \left\{ \frac{\partial V}{\partial y} \frac{\partial v}{\partial y} \right\} \text{ and } \left\{ \frac{\partial V}{\partial x} \frac{\partial u}{\partial y} \right\} ,$$

Equation A.4 is reduced to

$$\nabla^2 p' = -2\rho_o \frac{\partial U}{\partial y} \frac{\partial v}{\partial x} . \qquad A.5$$

This equation has been the foundation of a number of attempts to predict turbulent boundary layer wall pressure fluctuations. However, this equation only holds for the assumption that the orders of magnitude of the appropriate terms are small.

A result of the experimental work of this investigation showed that:

$$\partial U/\partial r = 0(1000)$$

$$\partial\sqrt{\overline{u^2}}\,/\partial r = 0(100)$$

$$\partial\sqrt{\overline{u^2}}\,/\partial x = 0(10).$$

Also from the turbulent intensity profile for the v component of the fluctuating velocity, a rough estimate of the order of magnitude for $\partial\sqrt{\overline{v^2}}/\partial r$ was made to be $0(50)$. Measurements of $\partial U/\partial x$ and $\partial V/\partial x$ were not taken, however, it is not expected that these quantities would be very large.

By making the crude approximations that $r \simeq y$ and $0(\sqrt{\overline{u^2}}) \simeq 0(u)$ it can be seen that the assumptions used to get Equation A.5 were valid.

Calibration Chart for
Condenser Microphone
Cartridge Type 4133

Serial No. 2314773

Brüel & Kjær
Denmark

Sensitivity at 250 Hz, 760 mm Hg, and with 200 V polarization voltage:

Measured at the output of a cathode follower with input capacity 3 pF and gain —0.9 dB (B & K) Cathode Follower 2614-2615):

...0,94... mV/μbar —...50,5... dB re. 1 V/μbar

K*) = +.....14,5 dB

Cartridge open circuit sensitivity:

....1,22... mV/μbar —...58,3 dB re. 1 V/μbar

Ko*) = +....12,3 dB

This calibration is traceable to The National Bureau of Standards, Washington D.C.

Cartridge capacity at 1 kHz with 200 V polarization:

C = ...18,7.. pF.

*) Correction Factor, for direct sound level reading on B & K Instruments adjusted to 3 mV/μbar = —46 dB re. 1 V/μbar.

BG 0061

Individual Frequency Response
The upper curve is the free field characteristic, valid for the Microphone Cartridge with protection grid, and mounted on Cathode Follower 2614 or 2615. Sound waves perpendicular to diaphragm. (See Fig.).

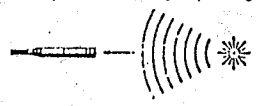

The lower curve is the pressure response curve recorded with electrostatic actuator.

Conditions of Test:

Temperature .....22.. °C

Barometric Pressure .....760.. mm Hg.

Relative Humidity .....40.. %

Date 12-11-68 Signature .R.S.....

Summarized Specifications

Outside Diameter: 0.5 inch (12.7 mm), without protecting grid.

Grid Thread (coupler mounting): 0.5 inch (12.7 mm) - 60 NS 2.

Resonant Frequency: approx. 25 kHz (overdamped).

Equivalent Air Volume at 1 atm. and 1 kHz < 0.01 cm³.

Temperature coefficient between —50 and + 60°C. Less than ± 0.01 dB/°C.

Ambient pressure coefficient: approx. —0.1 dB for + 10 % pressure change.

Relative Humidity influence: Less than 0.1 dB, in the absence of condensation.

Dynamic Range:
4 % distortion upper limit: 150 dB re. 0.0002 μbar
Safety limit: 174 dB re. 0.0002 μbar

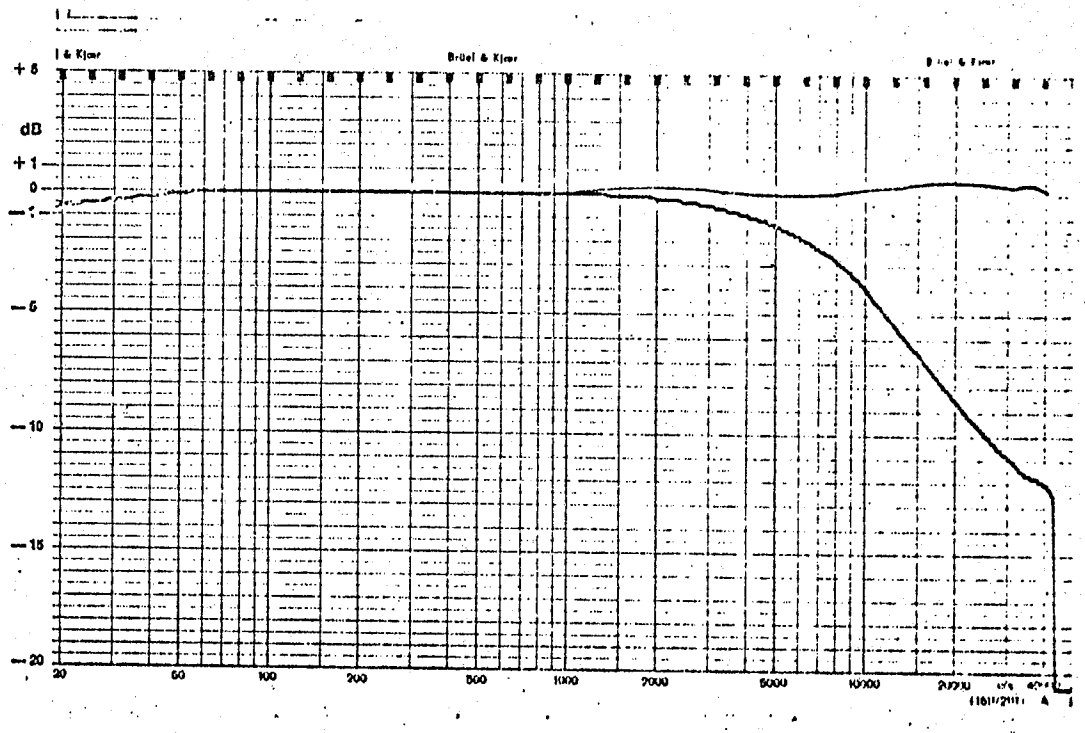

FIGURE A.1 CALIBRATION CURVE FOR THE BRUEL AND KJAER HALF INCH CONDENSER MICROPHONE.

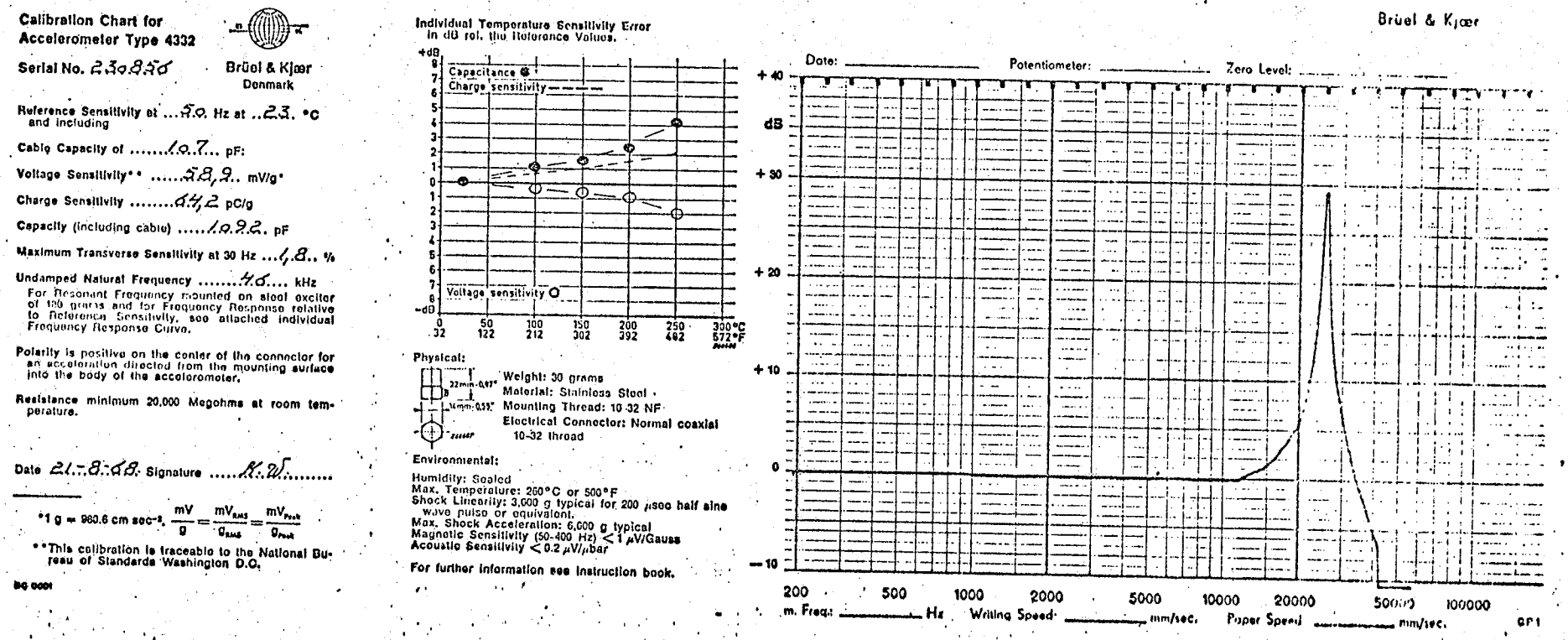

FIGURE A.2 CALIBRATION CURVE FOR THE BRUEL AND KJAER ACCELEROMETER.